

SIMULATION AND ANALYSIS OF MAGNETIC RECONNECTION IN A
LABORATORY PLASMA ASTROPHYSICS EXPERIMENT

by

NICHOLAS ARNOLD ECHLIN MURPHY

A dissertation submitted in partial fulfillment of the
requirements for the degree of

DOCTOR OF PHILOSOPHY

(ASTRONOMY)

at the

UNIVERSITY OF WISCONSIN – MADISON

2009

Abstract

Magnetic reconnection is an inherently multiscale process in which small-scale physics and large-scale dynamics both play important roles. To address the interplay between local and global effects, extended magnetohydrodynamic (MHD) simulations of the Magnetic Reconnection Experiment (MRX) are presented using the NIMROD code. Both the “pull” and “push” modes of operation are simulated with and without two-fluid effects in the generalized Ohm’s law. The pull reconnection rate is slowed by the presence of high downstream pressure. Because of the lesser volume available on the inboard side of the current sheet, density is depleted more quickly from the inboard upstream region than the outboard upstream region during pull reconnection, resulting in a radially inward drift of the current sheet. A buildup of pressure on the inboard side of the current sheet during push reconnection displaces the X-point towards the outboard side of the current sheet. Two-fluid simulations show good agreement with experimental observations of the quadrupole out-of-plane magnetic field associated with two-fluid reconnection. However, geometric effects are found to be more important in determining the reconnection rate than the inclusion of two-fluid effects. Communication between small and large scales is primarily due to pressure gradients that develop from a pileup of reconnection exhaust which then feed back on the reconnection process.

Magnetic reconnection with asymmetry in the outflow direction occurs in many situations in both nature and the laboratory. A control volume analysis is performed for the case of steady antiparallel magnetic reconnection with asymmetric downstream pressure to find approximate relations for conservation of mass, momentum, and energy in the resistive magnetohydrodynamic (MHD) framework. These relationships are used to derive the

outflow velocity from each side. The reconnection rate is not greatly affected except when outflow from both sides of the current sheet is blocked. Instead of bidirectional Alfvénic jets, reconnection with asymmetric downstream pressure can result in one Alfvénic jet and one sub-Alfvénic jet. A similar model is presented for reconnection in cylindrical geometry when the outflow is aligned with the radial direction. The predictions of these models are tested using resistive MHD simulations of driven asymmetric magnetic reconnection.

*To my friends Karin Lathin and Joseph Lindstrom,
for everything they have done for others*

Dr. McCoy: *“I knew it was wrong. I shouldn’t have done it!”*

Captain Kirk: *“What’s that?”*

Dr. McCoy: *“I should have never reconnected his mouth.”*

—STAR TREK, EPISODE #56, “SPOCK’S BRAIN”

“Resistance is futile.”

—THE BORG, KINDLY REMINDING US OF THE NEED TO INCLUDE ADDITIONAL TERMS IN OUR GENERALIZED OHM’S LAW

Acknowledgements

I would first like to thank Carl Sovinec and Ellen Zweibel for the support and assistance they have ceaselessly provided as my advisors. Without their guidance and patience, this thesis would not have been possible. What they have taught me will last throughout my entire career as a scientist.

The faculty of the Department of Astronomy must also be acknowledged for giving me the education and training necessary to be a professional astronomer. I would like to thank Linda Sparke for her idea during my first year to consider working with “Ellen’s friends in engineering,” an idea that has turned out to be quite fruitful. Discussions with Alex Lazarian during classes and seminars have improved my understanding of astrophysical magnetic fields and turbulence, and have given me a new appreciation of dust. Much of my knowledge of how to do astrophysical research came from working with Joseph Cassinelli during my first year in Madison. I thank my thesis committee (Joseph Cassinelli, Sebastian Heinz, Carl Sovinec, Rich Townsend, and Ellen Zweibel) for valuable comments on this manuscript.

I also acknowledge the help I have received from the plasma physics community in Madison, especially for making an astronomy graduate student feel welcome. In particular, I would like to thank Stewart Prager, Yi-Min Huang, Vladimir Mirnov, Chris Hegna, Fatima Ebrahimi, Adam Bayliss, and Ping Zhu. These simulations performed for this thesis used the NIMROD code, and I must thank all of those who have contributed to its development, including Carl Sovinec, Dalton Schnack, Dylan Brennan, Scott Kruger, Dan Barnes, Charlson

Kim, Alan Glasser, and the rest of the NIMROD team. In the greater plasma physics community, I must also thank Paul Cassak, Masaaki Yamada, Hantao Ji, Stefan Gerhardt, Yang Ren, Alexey Kuritsyn, Michiaki Inomoto, Seth Dorfman, Michael Brown, Chris Cothran, Michael Schaffer, Michael Shay, Brian Sullivan, Amitava Bhattacharjee, and Marc Swisdak. My thesis research was supported by the Center for Magnetic Self-Organization in Laboratory and Astrophysical Plasmas (CMSO). In addition to financial support, I found the CMSO to be a great community full of wonderful researchers dedicated to building bridges between laboratory and astrophysical plasma physics.

This is a largely computational thesis, and hence I must state my appreciation for the system administration skills of Stephan Jansen, who has kept the astronomy department network running smoothly. The astronomy department staff throughout my tenure as a graduate student have been wonderful, including Steve Anderson, Angela Normington, Lynn Thiele, and John Varda. I also thank Jane Schwantz and Dale Schutte from plasma physics. I must also express appreciation for several faculty from the University of Michigan and elsewhere during my time as an undergraduate, especially John Monnier, Hugh Aller, Joel Bregman, Rachel Somerville, Joel Smoller, and Jack Baldwin. I thank Hugh Aller in particular for his Astronomy 160 class which convinced me to go into astronomy.

I must also thank fellow students and post-docs for their contribution to the warm atmosphere of Wisconsin astronomy and physics, including (in the Department of Astronomy) Kat Barger, Andrey Beresnyak, Tom Bethell, Ella Braden, Blakesley Burkhart, Laura Chomiuk, Steve Crawford, Claudia Cyganowski, Kate Dellenbusch, Katie Devine, John Everett, Andy Fox, Emily Freeland, Sam Friedman, Aaron Geller, Natalie Gosnell, Kelley Hess, Alex Hill, Tabettha Hole, Ryan Keenan, Amanda Kepley, Min-Young Lee, Tommy Nelson, Lou Nigra, Matt Povich, Andrew Schechtman-Rook, Paul Sell, Elizabeth Stanway,

Aaron Steffen, Jennifer Stone, Laura Trouille, Christer Watson, Kyle Westfall, Isak Wold, Corey Wood, and (in the Departments of Physics and Engineering Physics) Chris Carey, Jim Reynolds, Jacob King, John O'Bryan, Eric Howell, Bonita Burke, Mark Schlutt, Tom Bird, Matt Palotti, Daniel Lecoanet, Tim Tharp, and Hillary Stephens.

I must also thank the many friends I have made outside of graduate school for helping to make my Madison experience memorable. From the Emma Goldman (now Audre Lorde) Co-op, I thank Joseph Lindstrom, Max Camp, Lauren Nielsen, Alex Hojem, Jana Grceвич, Summer Wilken, Cedric Lawson, Renee Gasch, Sylvia Jones, Kelly Rentscher, Brian Jordan, Mingwei Huang, Aaron Blecher, Ben Luedcke, Betsy Levine, Anne Seeber, Tom Ebersole, Sara Edquist, Lindsey Saunders, Nick Mader, Ali Muldrow, and many others. From Madison Community Co-op, I thank Stefanie Jones, Kathy Parker, Gabriel Heck, C. J. Carter, Lauren Allen, Rick White, Steve McClure, and Liz Shaffer-Wishner. From the Teaching Assistants' Association, I thank Claiborne Hill, Samaa Abdurraqib, Aaron Bibb, Rob Henn, Chris Bolander, Mark Supanich, Jay Gates, Stephanie Eastwood, Paul Reckner, Adam Berliner, Jason Murcko, Aaron Bibb, Peter Brinson, Sherry Johnson, Tim Frandy, Julien Colvin (with whom I got my picture taken with George Takei!), and Boian Popunkiov. From the rest of the Madison community, I thank Lori Nitzel, Austin King, Maura McCormick, Kyle Novak, Kerean Grant Povich, Trevor Irwin, Jon Bohman, Sean Hedican, and Christina Vandenhouten. To the members of Alliance for Animals, thank you for hosting numerous vegan dinners, where I always ate more than I should have, but never enough!

I would like to thank my family for their support, for putting up with me not calling home often enough, and for being there whenever I needed to visit or talk. Thank you Mom and Dad, Ron, Ellen, and Sue. And finally, I would like to thank my partner throughout most of graduate school, Sonja, for her patience, compassion, and understanding.

Contents

Abstract	i
1 Introduction	1
1.1 Introduction	2
1.2 Models of Magnetic Reconnection	5
1.2.1 The Sweet-Parker Model	7
1.2.2 The Petschek Model	13
1.2.3 Enhanced Resistivity from Small-Scale Instabilities	14
1.2.4 Turbulent Reconnection	16
1.2.5 Two-Fluid Reconnection	17
1.2.6 Asymmetric Reconnection	21
1.3 The Interplay Between Small and Large Scales During Magnetic Reconnection	23
1.4 Introduction to NIMROD	24
1.5 Overview of Thesis	27
References	28
2 Global Axisymmetric Simulations of Two-Fluid Reconnection in an Ex- perimentally Relevant Geometry	38

2.1	Introduction	39
2.2	Two-Fluid Model	41
2.3	MRX Simulation Setup	44
2.4	Resistive MHD Null-Helicity Simulations	50
2.4.1	Resistive MHD Pull Reconnection	50
2.4.2	Resistive MHD Push Reconnection	53
2.4.3	Discussion of Resistive MHD Results	56
2.4.3.1	Asymmetric Effects Associated with Cylindrical Geometry	56
2.4.3.2	Pressure Effects, Flux Availability, and Reconnection Rate	58
2.4.3.3	Scalings with Driving Voltage and Resistivity	59
2.5	Two-Fluid Null-Helicity Simulations	63
2.5.1	Two-Fluid Pull Reconnection	63
2.5.2	Two-Fluid Push Reconnection	66
2.5.3	Discussion of Two-Fluid Results	68
2.5.3.1	Comparison with Resistive MHD Reconnection	68
2.5.3.2	Azimuthal Flows	70
2.5.3.3	Electron Velocity Profile	70
2.5.3.4	Electron Outflow Opening Angle	72
2.5.3.5	Quadrupole Shape	73
2.5.4	Convergence	74
2.6	Co- and Counter-Helicity Two-Fluid Results	76
2.6.1	Two-Fluid Co-Helicity Push Reconnection	76
2.6.2	Two-Fluid Counter-Helicity Push Reconnection	79
	References	87

3	Magnetic Reconnection with Asymmetry in the Outflow Direction	92
3.1	Introduction	93
3.2	Equations of Magnetohydrodynamics	99
3.3	Linear Geometry	100
3.3.1	Effects of Symmetric Downstream Pressure	101
3.3.2	Effects of Asymmetric Downstream Pressure	103
3.3.3	Internal Structure of an Asymmetric Current Sheet	112
3.3.4	Comparison to Linear Geometry Simulations	114
3.4	Cylindrical Geometry	118
3.4.1	Global Properties and Internal Structure	121
3.4.2	Driven Reconnection in Cylindrical Geometry	125
3.4.3	Discussion	127
3.5	Applicability to Flux Cancellation and the Magnetotail	128
	References	134
4	Conclusions	141
4.1	Summary and Conclusions	142
4.2	Astrophysical Significance of Results	148
4.3	Future Work	151
	References	152
A	Technical Modifications to NIMROD	155
A.1	Introduction	156
A.2	Establishment of a Logically Non-Rectangular Grid	157
A.3	Defining Initial Conditions for a Logically Non-Rectangular Grid	162

A.4 Connectivity	165
A.4.1 Seam Matching Subroutines	170
References	180

List of Tables

1.1	Characteristic plasma parameters in a variety of physical settings.	8
2.1	Simulation parameters	49
3.1	Simulation results and model predictions at $t = 13.3 \mu s$	119
3.2	Application of linear geometry model to flux cancellation events	133

List of Figures

- | | | |
|-----|--|----|
| 1.1 | A Sweet-Parker reconnection layer of half-length L and half-thickness δ . . . | 9 |
| 1.2 | A characteristic resistive MHD simulation result for magnetic reconnection starting from a periodic Harris sheet equilibrium using the NIMROD code (see Section 1.4). Shown are contours of (a) out-of-plane current density and (b) magnetic flux. Note the presence of a long and thin diffusion region. . . . | 12 |
| 1.3 | A characteristic two-fluid simulation result for magnetic reconnection starting from a periodic Harris sheet equilibrium using the NIMROD code. Shown are contours of (a) out-of-plane current density, (b) magnetic flux, and (c) out-of-plane magnetic field. Note the presence of a strongly localized diffusion region, an X-point magnetic field geometry, and a quadrupole out-of-plane magnetic field near the X-point. | 18 |
| 2.1 | A low resolution version of the finite element grid used for cylindrical geometry simulations of two-fluid pull reconnection in MRX. Note that high resolution is present both in the reconnection region and along the expected position of the quadrupole field. | 45 |

2.2	The push and pull modes of operation in MRX. [Reprinted with permission from Yamada et al. 1997, Phys. Plasmas, 4, 1936. Copyright 1997, American Institute of Physics.]	47
2.3	Simulations of pull reconnection using a resistive MHD model show the development of Sweet-Parker-like current sheets. Shown are (a) the azimuthal current density and (b) the plasma pressure (in SI units) along with stream-traces of the magnetic field.	51
2.4	The position of the magnetic field null, the flow stagnation point, and the maximum current density as a function of time during a null-helicity resistive MHD simulation of pull reconnection. Similar behavior is observed when the Hall term is included.	53
2.5	Simulations of resistive MHD push reconnection in cylindrical geometry, showing (a) azimuthal current density and (b) plasma pressure, along with stream-traces of the poloidal magnetic field.	54
2.6	The position of the magnetic field null, the flow stagnation point, and the maximum current density as a function of time during a null-helicity resistive MHD simulation of push reconnection.	55
2.7	Comparisons of the (a) thickness δ , (b) length $L_{0.5}$, and (c) reconnecting electric field strength E_{recon} at $t = 11.2 \mu\text{s}$ for linear geometry simulations of push (squares) and pull (diamonds) reconnection using different values of resistivity. For this figure, $V_{\text{loop}} = 1000 \text{ V}$. The dotted lines represent the Sweet-Parker scaling $\delta \propto \eta^{1/2}$ for constant L , V_{in} , and B_{in} , and the dashed line represents the electric field E_{xvac} that would exist at the X-point in the absence of plasma.	60

- 2.8 Comparisons of the (a) thickness δ , (b) length $L_{0.5}$, and (c) reconnecting electric field strength E_{recon} at $t = 11.2 \mu\text{s}$ for linear geometry simulations of push (squares) and pull (diamonds) reconnection using different driving voltage strengths. The current sheet width decreases while the current sheet length and reconnecting electric field both increase. For this figure, $\eta/\mu_0 = 40 \text{ m}^2 \text{ s}^{-1}$. The dashed line represents E_{xvac} as a function of driving voltage. 61
- 2.9 (a) Experimental results showing azimuthal magnetic field contours along with electron velocity vectors during pull reconnection in a typical deuterium discharge in MRX, courtesy of Y. Ren (Ren 2007). (b) A closeup of azimuthal magnetic field contours during a simulation of two-fluid pull reconnection. Note the difference in the orientation of this figure with respect to the other figures in this chapter. 64
- 2.10 Simulation results for two-fluid null-helicity pull reconnection with the geometry of MRX, showing (a) the azimuthal magnetic field, (b) pressure contours, and (c) the outflow component of the electron velocity, V_{eZ} . The three images also include streamtraces of the poloidal magnetic field. The separatrix is colocated with the quadrupole field and the boundary between the low-pressure inflow and high-pressure outflow regions. 65
- 2.11 Azimuthal magnetic field contours with a poloidal magnetic field streamtrace during a simulation of two-fluid push reconnection. 67
- 2.12 The reconnecting electric field strength E_{recon} as a function of time for resistive MHD and two-fluid push and pull reconnection. The dotted line shows the electric field strength E_{xvac} that would exist at the initial X-point in the absence of plasma. 69

- 2.13 The outflow component of electron velocity during a linear geometry simulation of two-fluid pull reconnection. In (a), a comparison is made to an equivalent experimental result (data courtesy of Y. Ren). In (b), (c), and (d), comparisons of electron outflow profiles are made for different initial temperatures, driving voltage strengths, and resistivities. Unless noted, $\eta/\mu_0 = 40 \text{ m}^2 \text{ s}^{-1}$ 71
- 2.14 Results from a convergence study in which the simulations presented in Figure 2.12 are repeated with different numbers of finite elements. Shown for each of these simulations are (a) the peak magnitude of the resistive electric field, (b) the maximum pressure, and, for two-fluid simulations, (c) the peak magnitude of the out-of-plane quadrupole magnetic field. Asterisks correspond to the simulations presented in Figure 2.12. 75
- 2.15 Out-of-plane current density (a), out-of-plane magnetic field (b), and plasma pressure (c) during a linear geometry simulation of two-fluid co-helicity (guide field) push reconnection. 77
- 2.16 The vertical component of the Hall electric field (a), and the vertical components of the ion and electron velocities V_{iZ} and V_{eZ} (b) along $Z = 0$ during a linear geometry simulation of two-fluid co-helicity push reconnection. 78

- 2.17 Out-of-plane current density along with a magnetic field streamtrace of the separatrix (a), and plasma pressure with ion velocity vectors (b) during a simulation of two-fluid counter-helicity push reconnection performed in linear geometry to remove cylindrical geometry effects. The out-of-plane magnetic field induced by the flux cores is out of the page for $Z > 0$ and into the page for $Z < 0$. Note that in (a) the X-point is shifted to the left of $R = 0.375$ (the position of the flux core centers) and that in (b) there is strong ion outflow towards the right that leads to the asymmetric pressure buildup. 81
- 2.18 The positions of the magnetic field null, the radial ion flow stagnation point, the radial electron flow stagnation point, and the peak current density as a function of time during a simulation of counter-helicity merging in linear geometry. 82
- 2.19 Terms in the R -component of the momentum equation along $Z = 0$ m are compared for a simulation of two-fluid counter-helicity push reconnection using linear geometry. The X-point position is shifted to the left of $R = 0.375$ m due to the Hall effect. 84
- 2.20 Azimuthal current density (a), plasma pressure (b), and radial velocity (c) as functions of radius during counter-helicity push reconnection using cylindrical geometry. Symmetry breaking is due to both cylindrical geometry and the Hall effect. Cases I and O refer to two-fluid simulations of counter-helicity push reconnection showing an inward and outward radial shift, respectively. Case R refers to the resistive MHD equivalent of case I. 86

- 3.1 Sweet-Parker-like reconnection with asymmetric downstream pressure and a pressure gradient through the current sheet. The solid vertical bar inside the current sheet (marked s) represents the flow stagnation point and the dashed vertical bar (marked n) represents the magnetic field null. 104
- 3.2 The magnitude of flow velocity on the left side of the current sheet, $|V_L|$, calculated from equation (3.31) as a function of $p_L - p_{in}$ and $p_R - p_{in}$. Contours are separated by $0.2V_A$, with the thickest contour representing $V_L = V_A$. The value for V_R can be found by switching p_L and p_R . This figure assumes that the scaling factors in equations (3.20), (3.21), and (3.22) are unity. 109
- 3.3 The normalized reconnection rate, given by $S^{1/2}V_{in}/V_A = \sqrt{(V_L + V_R)/2V_A}$, as a function of $p_L - p_{in}$ and $p_R - p_{in}$ and calculated using equation (3.31) to find V_L and V_R . The contours are separated by 0.2, with the thickest contour representing a value of 1. This figure assumes that the scaling factors in equations (3.20), (3.21), and (3.22) are unity. 110
- 3.4 A slice in the outflow direction along $z = 0$ of terms from (a) momentum balance and (b) electric field balance for case B at $t = 13.3 \mu s$. Vertical bars represent the positions of the flow stagnation point (marked s) and the magnetic field null (marked n). The ideal electric field is zero at both the flow stagnation point and the magnetic field null. 115

3.5 Comparisons between the scaling relationships derived in Section 3.3 for reconnection with asymmetric downstream pressure and a resistive MHD simulation of the push mode of operation in MRX using linear geometry with one downstream wall closer to the reconnection site than the other. Shown are the left and right hand sides of equations (3.20)–(3.22) representing scaling relations for (a) mass, (b) momentum, and (c) energy. The data points representing cases A and B are plotted in blue and red, respectively, for $f = e^{-1}$ (diamonds) and $f = e^{-2}$ (plus signs). The data were extracted at $9.1 \mu\text{s}$, $11.2 \mu\text{s}$, $13.3 \mu\text{s}$, and $15.4 \mu\text{s}$ 117

3.6 Sweet-Parker-like reconnection in cylindrical geometry with outflow aligned with the radial direction. Because of the divergence constraint, B_{in} must be a function of radius. The solid vertical bar inside the current sheet represents the flow stagnation point and the dashed vertical bar represents the magnetic field null. 120

3.7 Comparisons between the scaling relationships derived in Section 3.4 for reconnection in cylindrical geometry with outflow aligned with the radial direction, and the resistive MHD simulation of the push mode of operation of MRX reported in Section 2.4.2. Shown are the left and right hand sides of equations (3.47), (3.59), and (3.62) representing scaling relations for (a) mass, (b) momentum, and (c) energy, where the symbol conventions of Figure 3.5 are used. The data were extracted at $9.1 \mu\text{s}$, $11.9 \mu\text{s}$, $13.3 \mu\text{s}$, and $15.4 \mu\text{s}$ 126

- 3.8 The ratio of the plasma pressure at a tailward distance of $X + L/2$ divided by the plasma pressure at a tailward distance of $X - L/2$ as a function of distance from Earth in the tailward direction for two possible characteristic lengths of a reconnection layer. The plasma pressure is calculated from equation (22) from the work of Zaharia et al. (2005). 132

Chapter 1

Introduction

1.1 Introduction

Magnetic reconnection is the process in which magnetic field lines are broken and rejoined in a highly conducting plasma. It is a fundamental process in plasma physics and is important to the evolution and dynamics of plasmas in astrophysics, space, and the laboratory. Reconnection, when it occurs, efficiently converts magnetic energy into kinetic and thermal energy and energized particles. Changes made by reconnection to magnetic topology in a plasma can have significant consequences for the global evolution of a system. For these reasons, magnetic reconnection is among the most active areas of plasma physics research.

Magnetic reconnection plays a fundamental role in the evolution of the solar atmosphere. The interplay between differential rotation, the solar dynamo, and convection ensure that the magnetic field of the Sun is typically highly stressed and prone to reconnection events (e.g., Aschwanden 2004, p. 407). In the corona, reconnection is believed to be responsible for energy release and particle acceleration during solar flares (e.g., Masuda et al. 1994; Tsuneta 1996). Reconnection is one of the leading candidates to explain the heating of the solar corona (e.g., Walsh & Ireland 2003). The topological changes associated with reconnection allow coronal mass ejections (CMEs) to occur (e.g., Lin & Forbes 2000). Observations of flux cancellation events (Martin et al. 1985) suggest that magnetic reconnection occurs as deep as the photosphere (e.g., Litvinenko & Martin 1999). Indeed, much of the early research on the reconnection process was motivated by solar physics.

There is indirect evidence that magnetic reconnection also occurs in the interstellar medium (ISM). If the magnetic field of the ISM were fully frozen into the interstellar plasma,

one would predict ~ 50 reversals of the large scale magnetic field (using an orbital time scale of ~ 200 Myr and an age of the Milky Way of ~ 10 Gyr, and assuming that the galactic disk initially had a coherent magnetic field). Current estimates of the number of these reversals range from two (Weisberg et al. 2004) to about eight (Han et al. 2006). That the number of reversals is so small suggests that some magnetic field diffusion must occur. Moreover, the generation of a large scale interstellar magnetic field through dynamo action is difficult to explain without invoking reconnection or some other form of magnetic field diffusion (e.g., Parker 1992; Blackman 1998; Widrow 2002 and references therein). For both of these reasons, magnetic reconnection is thought to be an important process in the ISM. Despite this indirect evidence, the extremely long length scales and miniscule classical resistivity associated with the ISM make it difficult to explain how reconnection can occur on time scales shorter than a Hubble time.

In situ observations of magnetic reconnection are possible via satellite measurements in the Earth's magnetosphere. At the dayside magnetopause, reconnection occurs as the interplanetary magnetic field (IMF) that is embedded in the solar wind pushes against the Earth's magnetosphere. The two plasmas involved in this process have considerably different properties (e.g., Phan & Paschmann 1996). Because these plasmas are topologically distinct prior to reconnection, it is common for the reconnecting magnetic field lines in the two sources to have a component parallel to each other (known as a guide field). The magnetosphere is a natural laboratory to study the physics of collisionless reconnection.

Reconnection plays an important role in magnetospheric substorms. These events occur when magnetic energy stored in the Earth's magnetotail as a result of driving from the solar wind is released into kinetic and thermal energy and energetic particles. Aurorae resulting from these energetic particles are signatures of these events. Recent results

from the THEMIS mission provide evidence that magnetotail reconnection is the triggering mechanism for at least a subset of these substorms (Angelopoulos et al. 2008). Reconnection allows the relaxation and self-organization of the magnetotail and consequently is important for the global energy balance in the magnetosphere. Much effort in recent years has been undertaken to include small-scale physics in global simulations of the magnetosphere (e.g., Kuznetsova et al. 2007). Reconnection events have also been observed in the Earth's magnetosheath (Phan et al. 2007) and in the solar wind (Gosling et al. 2007).

Reconnection plays an important role in magnetically confined plasmas in the laboratory. In tokamaks, sawteeth events associated with kink instabilities demonstrate temporary stochastization of the magnetic field and loss of core confinement resulting from reconnection (e.g., Yamada et al. 1994). Catastrophic losses of confinement known as disruptions involve global reconnection of the magnetic field in a tokamak (e.g., Goetz et al. 1991). Tearing modes (Furth et al. 1963) can develop in configurations such as reversed field pinches (RFPs) and tokamaks. The growth of these resistive instabilities flattens the temperature gradient in these configurations and reduce confinement (e.g., Chang & Callen 1990).

Reconnection is also important in the nonlinear evolution and saturation of many plasma instabilities. Simulations of the magnetized Kelvin-Helmholtz instability show that reconnection or reconnection-like events occur in the nonlinear regime as the magnetic field becomes wound up in vortices (Palotti et al. 2008; Faganello et al. 2009). Reconnection may play a role in the saturation of the magnetorotational instability (MRI) in accretion disks by balancing magnetic field growth (e.g., Sano 2005, 2007). Examples such as these highlight how the small-scale physics of magnetic reconnection interact with large-scale physics to help determine the nonlinear evolution of a plasma.

Magnetic reconnection is a fundamental process in laboratory plasmas, space plasmas,

and in astrophysics. Studies of reconnection in each of these fields are largely complementary to each other. For space plasmas, *in situ* measurements observe extremely fine structure along the satellite’s orbital path, but it is very difficult to reconstruct the large-scale configuration of the Earth’s magnetic field at any given time from these measurements. In the laboratory, it is possible to perform controlled experiments with multiple probes to gauge the large-scale structure of the magnetic field, but probe size limitations make measurements of fine structure difficult, and plasma parameters are typically more modest than in nature. Astrophysics provides an additional laboratory for the limiting case of extreme scale separation, but observations are typically averaged along the line of sight and constrained by limited resolution. For these reasons, understanding the physics of reconnection requires bridging these three different fields. Progress in understanding reconnection in one context will improve understanding of reconnection in other contexts. This thesis is a cross-disciplinary effort to bridge laboratory and astrophysical plasma physics in the context of magnetic reconnection.

1.2 Models of Magnetic Reconnection

Since the process of magnetic reconnection was first postulated by Giovanelli (1946), an abundance of models have been developed to describe how magnetic reconnection occurs (e.g., Parker 1957; Sweet 1958; Petschek 1964; Syrovatskii 1971; Sonnerup 1979; Mandt et al. 1994; Lazarian & Vishniac 1999; Heitsch & Zweibel 2003; Cassak & Shay 2007). In this section, I review several of these theories due to their importance, historical significance, and relevance to this thesis. Reviews of magnetic reconnection include those by Syrovatsky (1981), Hones (1985), Taylor (1986), Biskamp (1993, Chapter 6; 2000), Priest & Forbes (2000), Bhattacharjee (2004), Aschwanden (2004, Chapter 10), and Zweibel & Yamada

(2009).

Prior to discussing models of magnetic reconnection, it is important to discuss the nature of the electric field in the reconnection region. The generalized Ohm's law, which is derived from the electron equation of motion (e.g., Krall & Trivelpiece 1973), is given by

$$\mathbf{E} + \mathbf{V} \times \mathbf{B} = \eta \mathbf{J} + \frac{\mathbf{J} \times \mathbf{B}}{ne} - \frac{\nabla \cdot \mathbf{P}_e}{ne} + \frac{m_e}{ne^2} \left[\frac{\partial \mathbf{J}}{\partial t} + \nabla \cdot \left(\mathbf{J}\mathbf{V} + \mathbf{V}\mathbf{J} - \frac{\mathbf{J}\mathbf{J}}{ne} \right) \right], \quad (1.1)$$

in SI units where \mathbf{E} is the electric field in some inertial reference frame, \mathbf{V} is the center-of-mass flow velocity with respect to that frame, \mathbf{B} is the magnetic field, η is the resistivity, \mathbf{J} is the current density, n is the number density, e is the fundamental unit of charge, m_e is the mass of an electron, and \mathbf{P}_e is the electron pressure tensor. The quantities $\mathbf{J}\mathbf{V}$, $\mathbf{V}\mathbf{J}$, and $\mathbf{J}\mathbf{J}$ are dyadic tensors. The $-(\mathbf{V} \times \mathbf{B})$ term represents the ideal electric field. The right hand side includes (from left to right) the resistive term, the Hall term, the electron pressure term, and electron inertia. In the ideal MHD limit, all of the terms on the right hand side of equation (1.1) go to zero. As a consequence, the magnetic field is “frozen-in” to the plasma (e.g., the magnetic field is advected with the flow and magnetic topology is preserved). In the resistive MHD limit, the only term on the right hand side of equation (1.1) is the resistive term, which prevents the magnetic field from being perfectly frozen-in to the plasma and allows magnetic field line slippage. The Hall term by itself cannot change magnetic topology. Instead, it acts to freeze the magnetic field into the electron fluid. However, in the context of reconnection the Hall effect is able to modify the structure of the magnetic field away from the X-point to facilitate fast reconnection. Off-diagonal (nongyrotropic) terms in the electron pressure tensor can be a major contributor to the electric field during reconnection (e.g., Bessho & Bhattacharjee 2005). Magnetic topology can also be changed through the Biermann battery when temperature and number

density gradients are not parallel. Electron inertia is also able to contribute to magnetic field line breakage. The resistive term is important when the Lundquist number S [the ratio of a resistive diffusion time to an Alfvén crossing time; see equation (1.9)] is small. The Hall term and electron pressure term are typically important when variations occur on length scales shorter than the ion inertial length c/ω_{pi} and electron inertia is typically important when variations occur on length scales shorter than the electron inertial length c/ω_{pe} .¹ Characteristic plasma parameters for a variety of physical settings are shown in Table 1.1. Two-fluid effects are important in the Earth’s magnetosphere, tokamaks, and some laboratory plasma experiments, but are unlikely to be important in the ISM and the solar photosphere. Because of the enormous Lundquist number associated with the ISM using length scales comparable to a parsec, reconnection in the ISM most likely requires the development of small-scale structure (e.g., Haverkorn & Goss 2007; Stone & Zweibel 2009).

1.2.1 The Sweet-Parker Model

A significant advance in astrophysical plasma physics was the mechanism proposed by Sweet (1958) and analyzed by Parker (1957). As an alternative to global resistive diffusion of magnetic fields, Sweet pointed out that pushing two plasmas together with oppositely directed magnetic flux allows diffusion to occur on a length scale much shorter than a typical equilibrium length scale. When Parker analyzed this setup, he found that such a process could occur on timescales of weeks instead of the hundreds of years predicted for global magnetic field diffusion in solar flares.

¹The electron plasma frequency $\omega_{pe} = \sqrt{n_e e^2 / \epsilon_0 m_e}$ and the ion plasma frequency $\omega_{pi} = \sqrt{n_i Z^2 e^2 / \epsilon_0 m_i}$ represent the characteristic frequencies of electron and ion oscillations in a plasma due to inhomogeneities of charge. The electron inertial length c/ω_{pe} and the ion inertial length c/ω_{pi} are the characteristic length scales for each particle to be accelerated by electromagnetic forces in a plasma.

Table 1.1. Characteristic plasma parameters in a variety of physical settings.

Location	n (cm ⁻³)	T (K)	L (cm)	B (G)	S	c/ω_{pi} (cm)	c/ω_{pe} (cm)
Solar corona	10^8	10^6	10^9	50	2×10^{13}	2×10^3	50
Solar photosphere	5×10^{15}	6000	10^7	200	5×10^4	0.32	7.5×10^{-2}
Solar wind (1 AU)	10	10^5	10^{11}	5×10^{-5}	2×10^{11}	7×10^6	2×10^5
Earth's magnetotail	0.2	10^6	10^8	10^{-4}	7×10^{10}	5×10^7	10^6
ISM	1	10^4	10^{18}	5×10^{-6}	2×10^{16}	2×10^7	5×10^5
MRX ^a	5×10^{13}	1.7×10^5	25	350	240	4.5	8×10^{-2}
Tokamak	10^{14}	10^8	100	10^4	3×10^8	2.3	5×10^{-2}

^aAssuming deuterium ions.

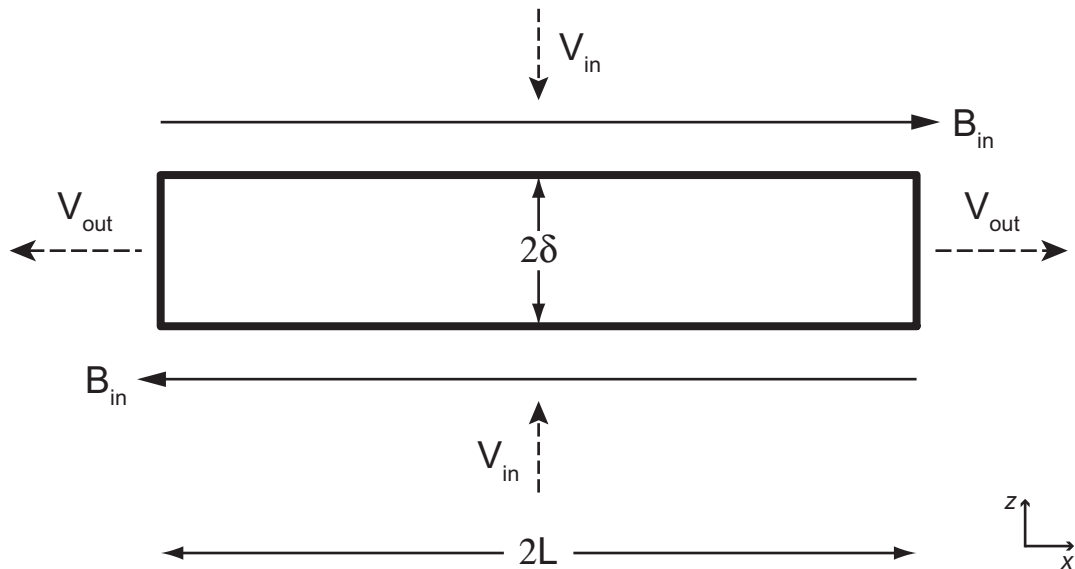


Fig. 1.1.—: A Sweet-Parker reconnection layer of half-length L and half-thickness δ .

The Sweet-Parker model describes steady-state antiparallel magnetic reconnection in the incompressible inviscid resistive MHD framework. Here, I repeat the derivation of the scaling relationships given by Parker (1957). The configuration associated with the Sweet-Parker model is given by Figure 1.1. In this derivation, x is the outflow direction, y is the out-of-plane direction, and z is the inflow direction. For a steady-state model, the electric field must be uniform. Resistivity is assumed to be important only within the reconnection layer. The ideal Ohm's law then yields the relation

$$E_y = V_{in} B_{in}, \quad (1.2)$$

where E_y is the uniform out-of-plane electric field, V_{in} is the inflow velocity, and B_{in} is the reconnection magnetic field strength. Using the low-frequency Ampere's law, the out-of-

plane current density, J_y , is approximately given by

$$J_y \sim \frac{B_{in}}{\mu_0 \delta}, \quad (1.3)$$

where δ is the current sheet half-thickness. For this relation, we use that the magnetic field reverses over a distance of $\sim 2\delta$. The inflow velocity, V_{in} , current sheet half-thickness δ , and resistivity η are then related by

$$V_{in} \sim \frac{\eta}{\mu_0 \delta}. \quad (1.4)$$

The above relationship represents the condition that the resistive electric field, ηJ_y , within the current sheet matches the ideal electric field outside the current sheet. The thickness of a steady state reconnection layer is set by how quickly magnetic field lines can diffuse.

For the incompressible case, conservation of mass yields the relationship

$$V_{in} L \sim V_{out} \delta, \quad (1.5)$$

where V_{out} is the outflow velocity and L is the half-length of the reconnection layer. The left-hand side represents the mass flux into the layer and the right-hand side represents the mass flux out of the layer.

A scaling relation for energy is then derived by assuming that the magnetic energy flux into the layer is proportional to the kinetic energy flux out of the layer,

$$V_{in} L \left(\frac{B_{in}^2}{2\mu_0} \right) \sim V_{out} \delta \left(\frac{\rho V_{out}^2}{2} \right). \quad (1.6)$$

Dividing by equation (1.5) and rearranging gives the relationship

$$V_{out} \sim V_A \equiv \frac{B_{in}}{\sqrt{\mu_0 \rho}}. \quad (1.7)$$

Thus, the outflow velocity in a Sweet-Parker current sheet scales with the upstream Alfvén speed. Using equation (1.4), the dimensionless reconnection rate can be given as

$$\frac{V_{in}}{V_A} \sim \frac{1}{S^{1/2}}, \quad (1.8)$$

where the Lundquist number S is defined to be

$$S \equiv \frac{\mu_0 L V_A}{\eta}. \quad (1.9)$$

Sweet-Parker reconnection occurs on an intermediate time scale between an Alfvén wave crossing time and a resistive diffusion time. However, the Sweet-Parker model ignores compressibility, downstream pressure, viscosity, three-dimensional effects, and kinetic effects not included in the MHD model.

When applied to the solar corona, the Sweet-Parker model predicts that reconnection will occur on time scales of weeks rather than the time scales of centuries as predicted by global magnetic field resistive diffusion (e.g., Parker 1957). While this is a significant theoretical improvement, the Sweet-Parker model is unable to explain the extremely short time scales of seconds to minutes observed for energy release during solar flares. Nevertheless, the Sweet-Parker model is a foundation upon which much of the theory of magnetic reconnection is built.

The Sweet-Parker model has been tested innumerable times using two-dimensional resistive MHD simulations of magnetic reconnection. The most notable of this class of simulations are those by Biskamp (1986), which showed the development of long and thin current sheets and agreement with the Sweet-Parker scalings. Characteristic resistive MHD simulation results for reconnection starting from a Harris sheet equilibrium² are shown in Figure 1.2 and feature the development of a long and thin extended diffusion region. The Sweet-Parker model is accepted as the correct model for reconnection in the resistive MHD framework for moderate Lundquist number ($S \sim 10^2$ – 10^4). Experimental tests of the Sweet-

²A Harris sheet equilibrium is given by $B_x(z) = B_0 \tanh(\frac{z}{\delta})$, $J_y(z) = \left(\frac{B_0}{\mu_0 \delta}\right) \operatorname{sech}(\frac{z}{\delta})$, and $p(z) = \left(\frac{B_0^2}{2\mu_0}\right) \operatorname{sech}(\frac{z}{\delta})$ using the coordinate system established in Section 1.2.1 (Harris 1962).

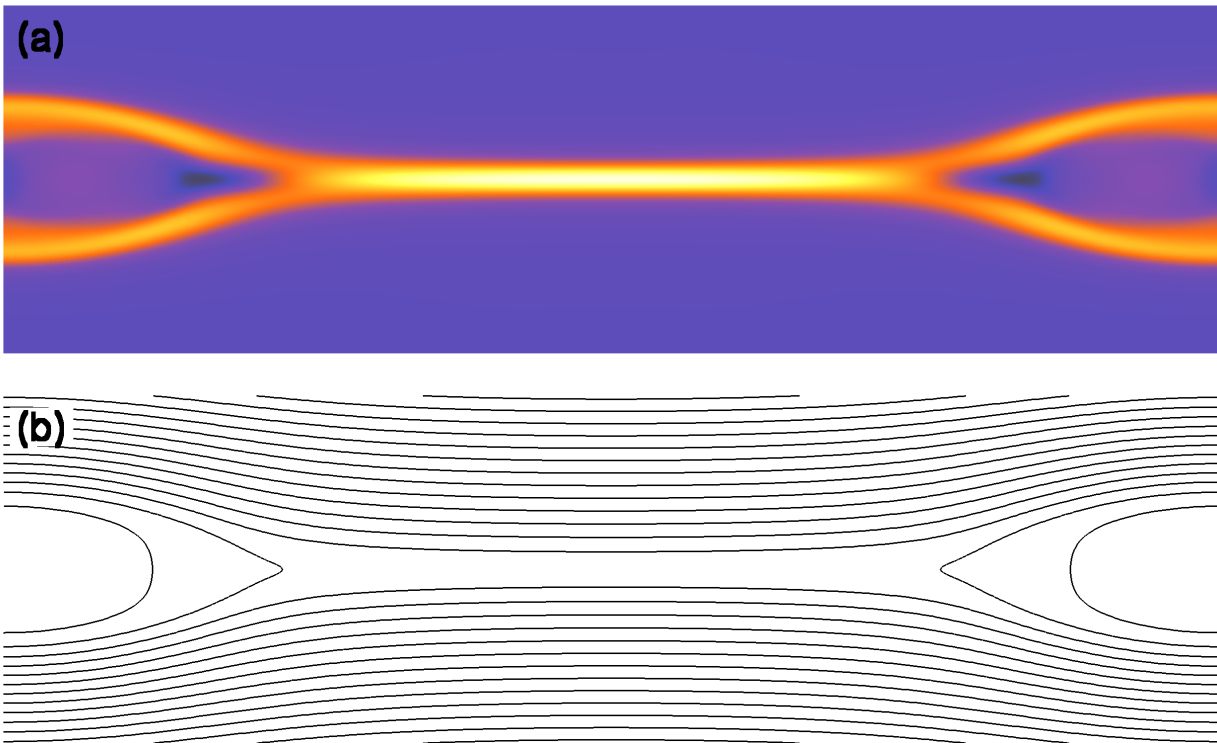


Fig. 1.2.—: A characteristic resistive MHD simulation result for magnetic reconnection starting from a periodic Harris sheet equilibrium using the NIMROD code (see Section 1.4). Shown are contours of (a) out-of-plane current density and (b) magnetic flux. Note the presence of a long and thin diffusion region.

Parker model were first done at the Magnetic Reconnection Experiment (MRX) by Ji et al. (1998, 1999) using collisional plasmas. A straightforward comparison to Sweet-Parker scalings did not compare well to experiment, and extensions to the model were needed to account for the effects of downstream pressure, anomalous resistivity, compressibility, and viscosity.

The validity of the Sweet-Parker model at extremely large Lundquist numbers has also been questioned. The extreme aspect ratios predicted by the Sweet-Parker model are unrealistic and likely unstable to plasmoid formation and ejection, potentially limiting the maximum length of a reconnection layer (e.g., Bulanov et al. 1978; Loureiro et al. 2007; Bhattacharjee et al. 2009). Turbulent motions can also help determine the maximum length of a coherent reconnection layer (e.g., Servidio et al. 2009).

1.2.2 The Petschek Model

A historically important model in the development of reconnection theory was proposed by Petschek (1964). Petschek realized that the reason why Sweet-Parker reconnection is so slow is that there is a bottleneck related to conservation of mass. In particular, plasma must exit the current sheet before new plasma can enter it for a steady state model. Petschek proposed a mechanism in which the reconnection inflow is mediated by four stationary slow mode shocks to allow a diffusion region much smaller than the global length scale. The maximum reconnection rate in this configuration is given by

$$\frac{V_{in}}{V_{out}} \approx \frac{\pi}{8 \ln S}. \quad (1.10)$$

The very weak dependence on the Lundquist number would allow fast reconnection via the slow shock mechanism for even astrophysical situations where S can be as high as 10^{21} . Consequently, the Petschek model gained widespread acceptance soon after it was proposed.

In the last 25 years there has been much doubt cast on Petschek’s slow mode shock model of fast reconnection. The resistive MHD simulations by Biskamp (1986) show that for a uniform resistivity, Sweet-Parker-like current sheets develop even when Petschek reconnection is used as an initial condition. Priest and Forbes (1986, 2000) note that Petschek (1964) assumes that the upstream magnetic field is approximately potential, which is inappropriate for driven reconnection. Kulsrud (2001) argues that the component of the downstream magnetic field in the inflow direction cannot be adequately regenerated in the Petschek model with uniform resistivity (cf. Baty et al. 2006). The Petschek solution is only able to be obtained in single fluid numerical simulations if an *ad hoc* resistivity enhancement is prescribed for the diffusion layer (e.g., Yan et al. 1992), but the justification for this resistivity enhancement is unclear. Fully kinetic simulations of magnetic reconnection (e.g., Daughton et al. 2006) do not show the development of slow mode shocks separating the inflow and the outflow. Moreover, laboratory experiments favor the formation of Sweet-Parker-like current sheets in collisional plasmas (Ji et al. 1998, 1999). Petschek’s mode of reconnection has not been conclusively observed in nature or the laboratory, and thus has fallen out of favor among most plasma physics researchers.

1.2.3 Enhanced Resistivity from Small-Scale Instabilities

Another means to achieve fast magnetic reconnection is through a resistivity enhancement beyond the classical values predicted by Spitzer and Härm (1953) for electron-ion collisions. Such resistivity enhancements have been postulated to explain observations in the laboratory (e.g., Ji et al. 1998, 1999) and inferred from observations of reconnection in solar flares (e.g., Chae et al. 2003). Many numerical simulations incorporate an *ad hoc* anomalous resistivity as a function of either physical location or current density to allow

fast reconnection within the resistive MHD framework, especially for global simulations (e.g., Borovsky et al. 2008). Physically, such resistivity enhancements are thought to be caused by small-scale instabilities in the current sheet which lead to microturbulence which in turn enhances magnetic field diffusion. A comprehensive review of such instabilities are given by Biskamp (2000, pp. 258–319).

A leading candidate for many years has been the lower hybrid drift instability (LHDI), which is destabilized in low- β^3 plasmas in regions of density gradients and cross-field currents (Krall & Liewer 1971). However, $\nabla\mathbf{B}$ drifts in high- β plasmas act to stabilize the LHDI. Because β is large in the central regions of an antiparallel current sheet, the LHDI is destabilized primarily in the regions of strong gradients away from the center of a current sheet. A consequence of this is that the resistivity enhancement is expected to occur along the boundary of the reconnection layer rather than in the central regions where it would be most effective at facilitating faster reconnection. Experimental results from the MRX device have shown that while the LHDI is destabilized, fluctuations resulting from the instability do not correlate with faster reconnection (Carter et al. 2002). Other candidate instabilities reviewed by Biskamp (2000) include the ion-sound instability and the whistler anisotropy instability. An additional electromagnetic drift instability derived in the context of reconnection in the laboratory has been considered by Ji et al. (2004), Kulsrud et al. (2005), Ji et al. (2005), and Wang et al. (2009). Ji et al. (2004) find that such electromagnetic fluctuations are positively correlated with a resistivity enhancement during laboratory reconnection events in experiment.

³Here, $\beta \equiv p/(B^2/2\mu_0)$ is the ratio of plasma pressure to magnetic pressure.

1.2.4 Turbulent Reconnection

Because of its ability to enhance diffusion processes, macroscopic turbulence has long been postulated as a means of enabling fast magnetic reconnection, especially in astrophysics contexts where resistivity is extremely small (e.g., Strauss 1988; Lazarian & Vishniac 1999). Indeed, many simulations suggest that turbulence is capable of enhancing the reconnection rate (Matthaeus & Lamkin 1986; Fan et al. 2004; Servidio et al. 2009; Loureiro et al. 2009; Kowal et al. 2009). Because reconnection is often bursty and explosive, it is also not surprising that reconnection is able to drive turbulent fluctuations. Such fluctuations have been observed in nature (Eastwood et al. 2009) and in the laboratory (Ji et al. 2005).

Lazarian & Vishniac (1999) argue that magnetic field line wandering due to turbulence will yield multiple simultaneous reconnection events in a three-dimensional reconnection layer and allow the rate of reconnection to be largely independent of resistivity. Kowal et al. (2009) present three-dimensional simulations of turbulent reconnection with a guide field comparable to the reconnecting magnetic field strength in which the turbulence is injected on a length scale larger than the current sheet thickness but less than the current sheet length (because of computing limitations). Their results are in agreement with many of the predictions by Lazarian & Vishniac (1999). Loureiro et al. (2009) find in similar simulations that turbulence is able to enhance the reconnection rate even in two dimensions. The model by Lazarian & Vishniac is manifestly three-dimensional, and consequently is unable to explain these results. In a different approach, Servidio et al. (2009) perform simulations of reconnection within a two-dimensional turbulent cascade and find a range of characteristic reconnection length scales and a broad distribution of reconnection rates. The lack of sufficient computing power has limited the ability to perform well-resolved simulations of

reconnection during a three-dimensional turbulent cascade with outer scales much larger than both the length and thickness of a current sheet. An important question in coming years will be how reconnection self-consistently fits into a turbulent cascade.

1.2.5 Two-Fluid Reconnection

In the last two decades, considerable progress has been made on understanding collisionless magnetic reconnection. Particular attention has been paid to the role of two-fluid effects⁴ in enabling fast reconnection. In the Geospace Environment Modeling (GEM) benchmark challenge, simulations of antiparallel magnetic reconnection using resistive MHD, two-fluid, hybrid, and particle-in-cell (PIC) codes found that for this problem all simulations including two-fluid effects showed fast reconnection (Birn et al. 2001) whereas resistive MHD simulations show slow reconnection. A typical NIMROD simulation of two-fluid reconnection starting from a Harris sheet equilibrium is shown in Figure 1.3 and features an X-point diffusion region instead of the extended diffusion region seen for resistive MHD simulations in Figure 1.2.

On scales shorter than the ion inertial length c/ω_{pi} , ions and electrons decouple. Ions respond sluggishly, while electrons are able to respond quickly to electromagnetic forces because of their low inertia. The magnetic field effectively becomes frozen into the electron fluid instead of the bulk plasma. Two-fluid simulations of magnetic reconnection show that an X-point geometry is formed when the resistive skin depth is shorter than an ion inertial length. This is in contrast to the double-Y geometry of Sweet-Parker current sheets which

⁴In the context of magnetic reconnection, two-fluid effects almost always refer to decoupling between ions and electrons. In other contexts not considered in this thesis, two-fluid effects can refer to decoupling between ions and neutrals.

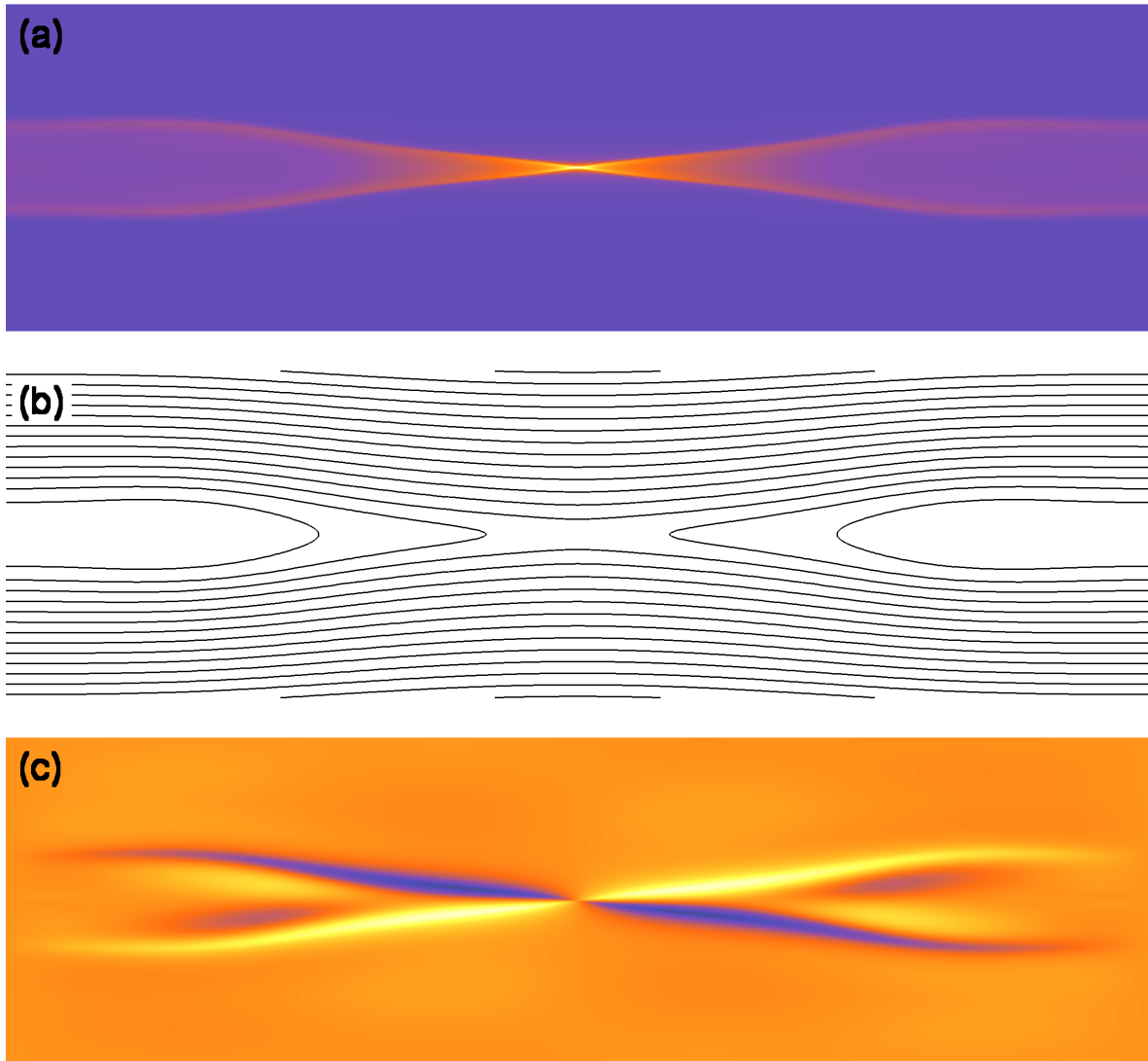


Fig. 1.3.—: A characteristic two-fluid simulation result for magnetic reconnection starting from a periodic Harris sheet equilibrium using the NIMROD code. Shown are contours of (a) out-of-plane current density, (b) magnetic flux, and (c) out-of-plane magnetic field. Note the presence of a strongly localized diffusion region, an X-point magnetic field geometry, and a quadrupole out-of-plane magnetic field near the X-point.

form when the resistive MHD approximation is valid. The Hall term itself cannot break magnetic field lines; rather, an additional component of the generalized Ohm's law such as resistivity, electron inertia, or off-diagonal components of the electron pressure tensor are required. The Hall effect acts to modify the structure surrounding the diffusion region without actually causing the diffusion itself.

Unlike resistive MHD, two-fluid systems contain important dispersive waves, including the whistler wave and the kinetic Alfvén wave (KAW). Mandt et al. (1994) attribute the speed of two-fluid reconnection to the dispersive nature of these waves. In particular, the frequencies of these waves are proportional to the square of the wavenumber, $\omega \sim k^2$. Consequently, the phase velocity is related to the wavenumber by the relation $V_\phi \equiv \omega/k \sim k$. Hence, the phase velocities of the whistler and KAW are faster for shorter disturbance length scales. In X-point reconnection, the length scale perpendicular to the outflow is small close to the X-point, but according to this picture the flux of plasma away from the X-point will be roughly constant regardless of the width of the outflow region. It is this property, according to Mandt et al. (1994), that makes two-fluid reconnection fast.

A distinctive feature of two-fluid antiparallel magnetic reconnection is the formation of an out-of-plane quadrupole magnetic field. Because the magnetic field is frozen into the electron fluid, the electron flow associated with the out-of-plane current in the reconnection layer pulls in-plane magnetic field lines in the out-of-plane direction (Sonnerup 1979; Mandt et al. 1994). This quadrupole field is a key signature of two-fluid reconnection and has been observed through *in situ* satellite observations in the Earth's magnetosphere (e.g., Øieroset et al. 2001) and in laboratory plasma experiments (Ren et al. 2005, 2008; Ren 2007; Yamada et al. 2006; Matthaeus et al. 2005; Brown et al. 2006). However, this quadrupole field is typically less prevalent during two-fluid reconnection with a guide field (e.g., Pritchett &

Coroniti 2004) and two-fluid asymmetric reconnection (e.g., Mozer et al. 2008).

Despite the ability of the Hall term to facilitate fast magnetic reconnection in fluid simulations, doubt has been cast on the applicability and completeness of the Hall reconnection model for collisionless plasmas. Karimabadi et al. (2004) find that fast reconnection can occur even when the Hall effect is removed from a hybrid simulation with kinetic ions and fluid electrons. Bessho & Bhattacharjee (2005) present PIC simulations of fast reconnection in an electron-positron plasma in which the Hall term is not present. Large-scale PIC simulations by Daughton et al. (2006) and Fujimoto (2006) show the development of an extended electron diffusion region which ends up slowing the reconnection rate. Daughton et al. argue that the repeated formation and ejection of plasmoids can keep the electron diffusion region short and allow reconnection to be fast. Shay et al. (2007) and Karimabadi et al. (2007) report a two-scale structure to the electron layer not present in resistive Hall MHD simulations including an inner electron diffusion region and extended electron jets. Drake et al. (2008), however, argue that the Hall electric field plays an important role in limiting the length of the inner diffusion region and electron outflow exhaust. The structure of the electron diffusion region is currently being investigated experimentally (e.g., Ren et al. 2008), through *in situ* satellite measurements in the Earth's magnetosphere (e.g., Phan et al. 2007), in fully kinetic simulations (e.g., Daughton et al. 2006; Fujimoto 2006; Shay et al. 2007; Karimabadi et al. 2007; Drake et al. 2008), in fluid simulations (e.g., Sullivan & Bhattacharjee 2009), and theoretically (e.g., Simakov & Chacón 2008; Malyshkin 2008; Uzdensky 2009).

1.2.6 Asymmetric Reconnection

The models described so far in this section have assumed that the process of magnetic reconnection is approximately symmetric. However, in many systems in nature and the laboratory, the assumption that a reconnection layer is symmetric to a 180° rotation about the magnetic field null must be relaxed. Reconnection with asymmetry in the inflow direction occurs in the Earth’s dayside magnetopause (e.g., Phan & Paschmann 1996), in the Earth’s magnetotail (Øieroset et al. 2004), during the merging of unequal flux tubes in the solar corona (Linton 2006), during turbulence (Servidio et al. 2009), and in laboratory plasmas (e.g., Yamada et al. 1994; Rogers & Zakharov 1995; see also Chapter 2). Reconnection with asymmetry in the outflow direction occurs during some solar flares and coronal mass ejections where one outflow jet is directed into the chomosphere and the other is directed away from the Sun, in some astrophysical disks (e.g., Cassinelli et al. 2002; ud-Doula et al. 2006) in the Earth’s magnetotail, and during spheromak merging experiments in the laboratory (e.g., Inomoto et al. 2006; see also Chapter 2).

Cassak & Shay (2007) present scaling relationships for steady magnetic reconnection with asymmetry in the inflow direction. Their analysis is repeated here. The subscripts “1” and “2” correspond to the two upstream sides of the reconnection layer. Otherwise, the definitions from Section 1.2.1 are used. Considerations regarding conservation of mass yield the scaling relation

$$L(\rho_1 V_1 + \rho_2 V_2) \sim 2\delta \rho_{out} V_{out}, \quad (1.11)$$

where the left hand side of the above relation represents the mass influx and the right hand side represents the mass efflux. Assuming that pressure does not play an important role in the scaling, balancing the magnetic energy influx with the kinetic energy efflux yields the

relation

$$L \left(\frac{B_1^2}{2\mu_0} V_1 + \frac{B_2^2}{2\mu_0} V_2 \right) \sim 2\delta \left(\frac{\rho_{out} V_{out}^2}{2} \right) V_{out}. \quad (1.12)$$

In a steady state, the out-of-plane electric field must be constant. Consequently, Faraday's law yields the relation

$$V_1 B_1 \sim V_2 B_2. \quad (1.13)$$

From equations (1.11)–(1.13), Cassak & Shay derive the scaling of the outflow speed to be

$$V_{out}^2 \sim \frac{B_1 B_2}{2\mu_0} \frac{B_1 + B_2}{\rho_1 B_2 + \rho_2 B_1}. \quad (1.14)$$

This equation can be simplified by using the relation,

$$\rho_{out} \sim \frac{\rho_1 B_2 + \rho_2 B_1}{B_1 + B_2}, \quad (1.15)$$

which assumes that the outflow density scales as the mean density between two newly reconnected flux tubes with equal flux. The outflow velocity can then be written as

$$V_{out}^2 \sim \frac{B_1 B_2}{2\mu_0 \rho_{out}}. \quad (1.16)$$

The outflow velocity is a hybrid Alfvén velocity based on the geometric mean of the upstream magnetic field strengths and the downstream density. The scaling of the reconnection electric field is then given by

$$E \sim \frac{2V_{out}\delta}{L} \left(\frac{B_1 B_2}{B_1 + B_2} \right). \quad (1.17)$$

In addition, the flow stagnation point and magnetic field null will in general not be colocated during reconnection with asymmetry in the inflow direction. The scaling relations from Cassak & Shay (2007) have been tested on numerous occasions (Borovsky & Hesse 2007; Cassak & Shay 2007, 2008, 2009; Borovsky et al. 2008; Pritchett 2008; Birn et al. 2008; Mozer et al. 2008; Servidio et al. 2009). Chapter 3 of this thesis includes a similar analysis for magnetic reconnection with asymmetry in the outflow direction.

1.3 The Interplay Between Small and Large Scales During Magnetic Reconnection

Magnetic reconnection is inherently a multiscale process in which small-scale physics and large-scale dynamics both play important roles. Global dynamics determine upstream and downstream conditions of the reconnection process, the parameter regimes of the reconnection layer, and how much flux is available to be reconnected. Local effects within the reconnection layer then determine the reconnection rate and whether the process is steady or bursty. Because reconnection is such an energetic process, small-scale physics within a reconnection layer is able to feed back on global scales both by expelling mass and energy and by changing the magnetic field topology. The changes on large scales are then able to feed back on small scales.

Simulating a multiscale process is difficult, especially when scale separation is extreme. Historically, simulations of reconnection performed to investigate small-scale physics (e.g., Biskamp 1986; Shay & Drake 1998; Hesse et al. 1999; Birn et al. 2001; Yin & Winske 2003; Karimabadi et al. 2004; Cassak et al. 2005; Bessho & Bhattacharjee 2005; Daughton et al. 2006; Drake et al. 2008) usually start with a simplified initial equilibrium such as a Harris sheet and simplified boundary conditions. Simulations including reconnection physics as part of a global problem have until recently been limited to resistive MHD (e.g., Birn et al. 1996; Birn et al. 2000; Lukin et al. 2001; Lukin & Jardin 2003). Recently, it has become computationally feasible to include small-scale physics in a global simulation (e.g., Dorfman et al. 2008). However, the maximum scale separation is still modest, and thus the inclusion of small-scale physics beyond resistive MHD remains very difficult for astrophysical situations. Consequently, computational efforts to understand the interplay between small-

scale physics and global dynamics are most readily done for situations with more modest scale separations, such as in laboratory plasmas. Chapter 2 of this thesis describes such an effort.

1.4 Introduction to NIMROD

The numerical results presented in this thesis were performed using the NIMROD code (Non-Ideal Magnetohydrodynamics with Rotation, Open Discussion; Sovinec et al. 2004). NIMROD solves the equations of extended MHD using a finite element representation for the poloidal plane and a finite Fourier series representation for the toroidal or out-of-plane direction. The use of finite elements allows great geometric flexibility without loss of convergence, making NIMROD an ideal choice for simulating a variety of axisymmetric plasma configurations. Mesh packing in the poloidal plane is used in most NIMROD simulations to ensure that regions of strong gradients are sufficiently resolved and that computing power is not unnecessarily wasted in regions with weak gradients.⁵ The numerical method used in NIMROD breaks fields into steady-state and perturbed components, making it straightforward to study both the linear and nonlinear evolution of plasma instabilities. The use of high order polynomial basis functions enables NIMROD to accurately represent highly anisotropic heat conduction even when the magnetic field is not aligned with the mesh. NIMROD uses a semi-implicit leapfrog time advance, with the velocity advance staggered half a step in time from the magnetic field, number density, and temperature advances. To achieve numerical stability at large Δt , NIMROD's time advance introduces numerical dispersion which slows the propagation of the dispersive waves present in two-fluid plasmas

⁵In contrast to adaptive mesh refinement (AMR) simulations, the locations of finite elements in NIMROD do not change over the course of a simulation.

at high wavenumber (Sovinec et al. 2005; Schnack et al. 2006).

NIMROD has been used to successfully model a variety of plasma phenomena in substantially different settings. In the laboratory, NIMROD has been applied to tokamaks (e.g., Brennan et al. 2005), spheromaks (e.g., Sovinec et al. 2001; Hooper et al. 2005), reversed field pinches (e.g., Reynolds et al. 2008), and field-reversed configurations (e.g., Milroy & Steinhauer 2008). A δf PIC method adapted for finite elements (Fivaz et al. 1998) has been used to study the effects of a minority energetic particle population on internal kink modes and fishbone instabilities starting from tokamak-like equilibria (Kim 2008). In space physics, NIMROD has been used to study the onset of magnetospheric substorms via the ballooning instability in the Earth’s magnetotail (Zhu et al. 2007). In astrophysics, NIMROD is being used to study plasma rotation as a mechanism for stabilizing kink modes in astrophysical jets (Carey & Sovinec 2009).

NIMROD solves the equations of extended MHD in a single-fluid framework. For resistive MHD simulations, the combined Faraday/Ohm’s law is given by

$$\frac{\partial \mathbf{B}}{\partial t} = -\nabla \times (\eta \mathbf{J} - \mathbf{V} \times \mathbf{B}) + \kappa_{divb} \nabla \nabla \cdot \mathbf{B}, \quad (1.18)$$

where the term $\kappa_{divb} \nabla \nabla \cdot \mathbf{B}$ is an artificial term used to control divergence error. For the two-fluid simulations reported in Chapter 2, the combined Faraday/Ohm’s law takes the form

$$\frac{\partial \mathbf{B}}{\partial t} = -\nabla \times \left(\eta \mathbf{J} - \mathbf{V} \times \mathbf{B} + \frac{\mathbf{J} \times \mathbf{B}}{ne} - \frac{\nabla p_e}{ne} \right) + \kappa_{divb} \nabla \nabla \cdot \mathbf{B}, \quad (1.19)$$

where the Hall term, given by $\mathbf{J} \times \mathbf{B}/ne$, ties the magnetic field to the electron fluid rather than the bulk plasma. A scalar electron pressure is used. The terms in parentheses in equations (1.18) and (1.19) represent the electric field in the laboratory reference frame for

the two physical models. The low-frequency Ampere's law is given by

$$\mu_0 \mathbf{J} = \nabla \times \mathbf{B}. \quad (1.20)$$

The momentum equation used in the simulations reported in this thesis is given by

$$\rho \left(\frac{\partial}{\partial t} + \mathbf{V} \cdot \nabla \right) \mathbf{V} = \mathbf{J} \times \mathbf{B} - \nabla p - \nabla \cdot \Pi_i(\mathbf{V}), \quad (1.21)$$

where the ion stress tensor $\Pi_i(\mathbf{V})$ is chosen to represent the appropriate closure. For the simulations presented in this thesis, the stress tensor is given by

$$\Pi_i = -\rho\nu\nabla\mathbf{V}, \quad (1.22)$$

where ν is the kinematic viscosity. The continuity equation is given by

$$\frac{\partial n}{\partial t} + \nabla \cdot (n\mathbf{V}) = \nabla \cdot D\nabla n, \quad (1.23)$$

where D is an artificial number density diffusivity used to prevent accumulation of noise in number density. The energy equation is given by

$$\frac{n}{\gamma - 1} \left(\frac{\partial T_\alpha}{\partial t} + \mathbf{V}_\alpha \cdot \nabla T_\alpha \right) = -p_\alpha \nabla \cdot \mathbf{V}_\alpha - \nabla \cdot \mathbf{q}_\alpha + Q_\alpha, \quad (1.24)$$

where the subscript α represents species. The heating term Q_α includes Ohmic and viscous heating. For simulations with isotropic thermal conductivity, the heat flux \mathbf{q}_α is given by

$$\mathbf{q}_\alpha = -n\chi\nabla T. \quad (1.25)$$

For simulations with anisotropic thermal conductivity, the heat flux density is given by

$$\mathbf{q}_\alpha = -n \left[\chi_{\parallel,\alpha} \hat{\mathbf{b}}\hat{\mathbf{b}} + \chi_{\perp,\alpha} \left(\mathbf{I} - \hat{\mathbf{b}}\hat{\mathbf{b}} \right) \right] \cdot \nabla T_\alpha, \quad (1.26)$$

where \mathbf{b} is a unit vector in the direction of the magnetic field. Quasineutrality and rapid ion/electron equilibration are assumed. The numerical model in the context of simulations of MRX is further discussed in Section 2.2.

1.5 Overview of Thesis

To address the interplay between local and global effects during magnetic reconnection, I present simulations of magnetic reconnection using the geometry and driving mechanism of MRX (Yamada et al. 1997) in Chapter 2. MRX is a laboratory astrophysics experiment designed to study the basic physics of magnetic reconnection in a controlled setting. Both the “push” and “pull” modes of operation are simulated with and without the inclusion of two-fluid effects. Downstream pressure acts to reduce the outflow velocity to a fraction of the Alfvén velocity. Moreover, downstream pressure acts differently during the two modes of operation. During pull reconnection, both downstream exits of the reconnection layer are impeded by the presence of high downstream pressure, whereas during push reconnection, only one of the two exits is greatly obstructed. Push reconnection is observed to occur more quickly during these simulations than pull reconnection. Two-fluid effects do facilitate faster reconnection, but geometric effects are found to be more important than two-fluid effects in determining the reconnection rate in these models. Much of the communication between small and large scales is due to pressure gradients that develop due to a pileup of reconnection exhaust and feed back on the reconnection layer.

In Chapter 3, I present a framework to describe steady magnetic reconnection with asymmetry in the outflow direction. In particular, the downstream pressure is not assumed to be identical for both exits from the reconnection layer. In solar physics, these considerations are relevant for reconnection during some solar flares, coronal mass ejections, and flux cancellation events. Reconnection in the near-Earth magnetotail will often show asymmetry in the outflow direction due to the presence of a large pressure gradient. During spheromak merging in laboratory plasma experiments, asymmetry in the outflow direction results from

cylindrical geometry effects. Scaling relations for such a setup are derived for both linear and cylindrical geometry. These scaling relations can be used to derive an expression for the outflow velocity from both ends given other upstream and downstream parameters. The flow stagnation point and magnetic field null will overlap only in the absence of a pressure gradient at the flow stagnation point. In agreement with results from Chapter 2 and simulations by Oka et al. (2008), the reconnection rate is found to be greatly affected only when outflow from both sides of the current sheet is obstructed.

The summary and conclusions for this thesis are contained within Chapter 4. Conclusions for Chapters 3 and 4 are presented in Section 4.1. The astrophysical implications of the research performed for this thesis are discussed in Section 4.2. Future work and remaining problems are considered in Section 4.3.

In Appendix A, I include a discussion of technical modifications made to NIMROD during simulations of MRX. It is intended for users of NIMROD, especially those who will be performing a similar application or need to develop a mesh that is not logically rectangular. Others may find it useful as a gauge of what programming may be required for a simulation of this magnitude. Basic familiarity with NIMROD is assumed for this appendix.

References

- Angelopoulos, V., McFadden, J. P., Larson, D., Carlson, C. W., Mende, S. B., Frey, H., Phan, T., Sibeck, D. G., Glassmeier, K.-H., Auster, U., Donovan, E., Mann, I. R., Rae, I. J., Russell, C. T., Runov, A., Zhou, X.-Z., & Kepko, L. 2008, *Science*, 321, 931
- Aschwanden, M. J. 2004, *Physics of the Solar Corona* (Chichester, UK: Springer-Praxis)
- Baty, H., Priest, E. R., & Forbes, T. G. 2006, *Phys. Plasmas*, 13, 022312

- Bessho, N., & Bhattacharjee, A. 2005, *Phys. Rev. Lett.*, 95, 245001
- Bhattacharjee, A. 2004, *ARA&A*, 42, 365
- Bhattacharjee, A., Huang, Y.-M., Yang, H., & Rogers, B. 2009, arXiv:0906.5599
- Birn, J., Hesse, M., & Schindler, K. 1996, *J. Geophys. Res.*, 101, 12939
- Birn, J., Gosling, J. T., Hesse, M., Forbes, T. G., & Priest, E. R. 2000, *ApJ*, 541, 1078
- Birn, J., Drake, J. F., Shay, M. A., Rogers, B. N., Denton, R. E., Hesse, M., Kuznetsova, M., Ma, Z. W., Bhattacharjee, A., Otto, A., & Pritchett, J. 2001, *J. Geophys. Res.*, 106, 3715
- Birn, J., Borovsky, J. E., & Hesse, M. 2008, *Phys. Plasmas*, 15, 032101
- Biskamp, D. 1986, *Phys. Fluids*, 29, 1520
- Biskamp, D. 1993, *Nonlinear Magnetohydrodynamics* (Cambridge, UK: Cambridge University Press)
- Biskamp, D. 2000, *Magnetic Reconnection in Plasmas* (Cambridge, UK: Cambridge University Press)
- Blackman, E. G. 1998, *ApJL*, 496, L17
- Borovsky, J. E., & Hesse, M. 2007, *Phys. Plasmas*, 14, 102309
- Borovsky, J. E., Hesse, M., Birn, J., & Kuznetsova, M. M. 2008, *J. Geophys. Res.*, 113, A07210
- Brennan, D. P., Kruger, S. E., Gianakon, T. A., & Schnack, D. D. 2005, *Nucl. Fusion*, 45, 1178
- Brown, M. R., Cothran, C. D., & Fung, J. 2006, *Phys. Plasmas*, 13, 056503

- Bulanov, S. V., Syrovatsky, S. I., & Sakai, J. 1978, JETP Lett., 28, 177
- Carey, C. S., & Sovinec, C. R. 2009, ApJ, 699, 362
- Carter T. A., Yamada, M., Ji, H., Kulsrud, R. M., & Trintchouk, F. 2002, Phys. Plasmas, 9, 3272
- Cassak, P. A., Shay, M. A., & Drake, J. F. 2005, Phys. Rev. Lett., 95, 235002
- Cassak, P. A., & Shay, M. 2007, Phys. Plasmas, 14, 102114
- Cassak, P. A., & Shay, M. 2008, Geophys. Res. Lett., 35, L19102
- Cassak, P. A., & Shay, M. 2009, Phys. Plasmas, 16, 055704
- Cassinelli, J. P., Brown, J. C., Maheswaran, M., Miller, N. A., & Telfer, D. C. 2002, ApJ, 578, 951
- Chae, J., Moon, Y.-J., & Park, S.-Y. 2003, J. Korean Astron. Soc., 36, S13
- Chang, Z., & Callen, J. D. 1990, Nucl. Fusion, 30, 219
- Daughton, W., Scudder, J., & Karimabadi, H. 2006, Phys. Plasmas, 13, 072101
- Dorfman, S., Daughton, W., Roytershteyn, V., Ji, H., Ren, Y., & Yamada, M. 2008, Phys. Plasmas, 15, 102107
- Drake, J. F., Shay, M. A., & Swisdak, M. 2008, Phys. Plasmas, 15, 042306
- Eastwood, J. P., Phan, T. D., Bale, S. D., & Tjulin, A. 2009, Phys. Rev. Lett., 102, 035001
- Faganello, M., Califano, F., & Pegoraro, F. 2009, New J. Phys., 11, 063008
- Fan, Q.-L., Feng, X.-S., & Xiang, C.-Q. 2004, Phys. Plasmas, 11, 5605
- Fivaz, M., Brunner, S., de Ridder, G., Sauter, O., Tran, T. M., Vaclavik, J., Villard, L., & Appert, K. 1998, Comp. Phys. Comm., 111, 27

- Fujimoto, K. 2006, *Phys. Plasmas*, 13, 072904
- Furth, H. P., Killeen, J., & Rosenbluth, M. N. 1963, *Phys. Fluids*, 6, 459
- Giovanelli, R. G. 1946, *Nature*, 158, 81
- Goetz, J. A., Dexter, R. N., & Prager, S. C. 1991, *Phys. Rev. Lett.*, 66, 608
- Gosling, J. T., Eriksson, S., Blush, L. M., Phan, T. D., Luhmann, J. G., McComas, D. J., Skoug, R. M., Acuna, M. H., Russell, C. T., & Simunac, K. D. 2007, *Geophys. Res. Lett.*, 34, L20108
- Han, J. L., Manchester, R. N., Lyne, A. G., Qiao, G. J., & van Straten, W. 2006, *ApJ*, 642, 868
- Harris, E. G. 1962, *Nuovo Cimento*, 23, 115
- Haverkorn, M., & Goss, W. M., eds. 2007, *SINS—Small Ionized and Neutral Structures in the Diffuse Interstellar Medium*, ASP Conf. Ser. Vol. 365 (San Francisco, CA: ASP)
- Heitsch, F., & Zweibel, E. G. 2003, *ApJ*, 583, 229
- Hesse, M., Schindler, K., Birn, J., & Kuznetsova, M. 1999, *Phys. Plasmas*, 6, 1781
- Hones, E. W., Jr. 1985, *Australian Journal of Physics*, 38, 981
- Hooper, E. B., Kopriva, T. A., Cohen, B. I., Hill, D. N., McLean, H. S., Wood, R. D., & Woodruff, S. 2005, *Phys. Plasmas*, 12, 092503
- Inomoto, M., Gerhardt, S. P., Yamada, M., Ji, H., Belova, E., Kuritsyn, A., & Ren, Y. 2006, *Phys. Rev. Lett.*, 97, 092503
- Ji, H., Yamada, M., Hsu, S., & Kulsrud, R. 1998, *Phys. Rev. Lett.*, 80, 3256

- Ji, H., Yamada, M., Hsu, S., Kulsrud, R., Carter, T., & Zaharia, S. 1999, *Phys. Plasmas*, 6, 1743
- Ji, H., Terry, S., Yamada, M., Kulsrud, R., Kuritsyn, A., & Ren, Y. 2004, *Phys. Rev. Lett.*, 92, 115001
- Ji, H., Kulsrud, R., Fox, W., & Yamada, M. 2005, *J. Geophys. Res.*, 110, A08212
- Karimabadi, H., Krauss-Varban, D., Huba, J. D., & Vu, H. X. 2004, *J. Geophys. Res.*, 109, A09205
- Karimabadi, H., Daughton, W., & Scudder, J. 2007, *Geophys. Res. Lett.*, 34, L13104
- Kim, C. C., & the NIMROD team 2008, *Phys. Plasmas*, 15, 072507
- Kowal, G., Lazarian, A., Vishniac, E. T., & Otmianowska-Mazur, K. 2009, *ApJ*, 700, 63
- Krall, N. A., & Liewer, P. C. 1971, *Phys. Rev. A*, 4, 2094
- Krall, N. A., & Trivelpiece, A. W. 1973, *Principles of Plasma Physics* (Tokyo: McGraw-Hill Kogakusha)
- Kulsrud, R. 2001, *Earth Planets Space*, 53, 417
- Kulsrud, R., Ji, H., Fox, W., & Yamada, M. 2005, *Phys. Plasmas*, 12, 082301
- Kuznetsova, M. M., Hesse, M., Rastätter, L., Taktakishvili, A., Toth, G., De Zeeuw, D. L., Ridley, A., & Gombosi, T. I. 2007, *J. Geophys. Res.*, 112, A10210
- Lazarian, A., & Vishniac, E. T. 1999, *ApJ*, 517, 700
- Lin, J., & Forbes, T. G. 2000, *J. Geophys. Res.*, 105, 2375
- Linton, M. G. 2006, *J. Geophys. Res.*, 111, A12S09
- Litvinenko, Y. E., & Martin, S. F. 1999, *Sol. Phys.*, 190, 45

- Loureiro, N. F., Schekochihin, A. A., & Cowley, S. C. 2007, *Phys. Plasmas*, 14, 100703
- Loureiro, N. F., Uzdensky, D. A., Schekochihin, A. A., Cowley, S. C., & Yousef, T. A. 2009, arXiv:0904.0823
- Lukin, V. S., Qin, G., Matthaeus, W. H., & Brown, M. R. 2001, *Phys. Plasmas*, 8, 1600
- Lukin, V. S., & Jardin, S. C. 2003, *Phys. Plasmas*, 10, 3131
- Malyshkin, L. M. 2008, *Phys. Rev. Lett.* 101, 225001
- Mandt, M. E., Denton, R. E., & Drake, J. F. 1994, *Geophys. Res. Lett.*, 21, 73
- Martin, S. F., Livi, S. H. B., & Wang, J. 1985, *Australian J. Phys.*, 38, 929
- Masuda, S., Kosugi, T., Hara, H., Tsuneta, S., & Ogawara, Y. 1994, *Nature*, 371, 495
- Matthaeus, W. H., & Lamkin, S. L. 1986, *Phys. Fluids*, 29, 2513
- Matthaeus, W. M., Cothran, C. D., Landreman, M., & Brown, M. R. 2005, *Geophys. Res. Lett.*, 32, 23104
- Milroy, R. D., & Steinhauer, L. C. 2008, *Phys. Plasmas*, 15, 022508
- Mozer, F. S., Angelopoulos, V., Bonnell, J., Glassmeier, K. H., & McFadden, J. P. 2008, *Geophys. Res. Lett.*, 35, L17S04
- Øieroset, M., Phan, T. D., Fujimoto, M., Lin, R. P., & Lepping, R. P. 2001, *Nature*, 412, 414
- Øieroset, M., Phan, T. D., Fujimoto, M. 2004, *Geophys. Res. Lett.*, 31, L12801
- Oka, M., Fujimoto, M., Nakamura, T. K. M., Shinohara, I., Nishikawa, K.-I. 2008, *Phys. Rev. Lett.*, 101, 205004
- Palotti, M. L., Heitsch, F., Zweibel, E. G., & Huang, Y.-M. 2008, *ApJ*, 678, 234

- Parker, E. N. 1957, *J. Geophys. Res.*, 62, 509
- Parker, E. N. 1992, *ApJ*, 401, 137
- Petschek, H. E. 1964, in *AAS/NASA Symposium on the Physics of Solar Flares*, ed. W. N. Hess, (Washington, D.C.: NASA), 425
- Phan, T. D., & Paschmann, G. 1996, *J. Geophys. Res.*, 101, 7801
- Phan, T. D., Paschmann, G., Twitty, C., Mozer, F. S., Gosling, J. T., Eastwood, J. P., Øieroset, M., Rème, H., & Lucek, E. A. 2007, *Geophys. Res. Lett.*, 34, L14104
- Priest, E. R., & Forbes, T. G. 1986, *J. Geophys. Res.*, 91, 5579
- Priest, E., & Forbes, T. 2000, *Magnetic Reconnection: MHD Theory and Applications* (Cambridge, UK: University Press)
- Pritchett, P. L., & Coroniti, F. V. 2004, *J. Geophys. Res.*, 109, A01220
- Pritchett, P. L. 2008, *J. Geophys. Res.*, 113, A06210
- Ren, Y., Yamada, M., Gerhardt, S., Ji, H., Kulsrud, R., & Kuritsyn, A. 2005, *Phys. Rev. Lett.* 95, 055003
- Ren, Y., Ph.D. thesis, Princeton University, 2007
- Ren, Y., Yamada, M., Ji, H., Dorfman, S., Gerhardt, S. P., & Kulsrud, R. 2008, *Phys. Plasmas*, 15, 082113
- Reynolds, J. M., Sovinec, C. R., & Prager, S. C. 2008, *Phys. Plasmas*, 15, 062512
- Rogers, B., & Zakharov, L. 1995, *Phys. Plasmas*, 2, 3420
- Sano, T. 2005, *AIP Conf. Proc.* 784, *Magnetic Fields in the Universe: From Laboratory and Stars to Primordial Structures*, ed. E. M. de Gouveia Dal Pino, G. Lugones, & A.

- Lazarian (Melville, NY: AIP), 635
- Sano, T. 2007, *Ap&SS*, 307, 191
- Schnack, D. D., Barnes, D. C., Brennan, D. P., Hegna, C. C., Held, E., Kim, C. C., Kruger, S. E., Pankin, A. Y., & Sovinec, C. R. 2006, *Phys. Plasmas*, 13, 058103
- Servidio, S., Matthaeus, W. H., Shay, M. A., Cassak, P. A., & Dmitruk, P. 2009, *Phys. Rev. Lett.*, 102, 115003
- Shay, M. A., & Drake, J. F. 1998, *Geophys. Res. Lett.*, 25, 3759
- Shay, M. A., Drake, J. F., & Swisdak, M. 2007, *Phys. Rev. Lett.*, 99, 155002
- Simakov, A. N., & Chacón, L. 2008, *Phys. Rev. Lett.*, 101, 105003
- Sonnerup, U. O. 1979, in *Solar System Plasma Physics*, ed. L. T. Lanzerotti, C. Kennel, & E. N. Parker (Amsterdam: North-Holland), 45
- Sovinec, C. R., Finn, J. M., & Del-Castillo-Negrete, D. 2001, *Phys. Plasmas*, 8, 475
- Sovinec, C. R., Glasser, A. H., Gianakon, T. A., Barnes, D. C., Nebel, R. A., Kruger, S. E., Schnack, D. D., Plimpton, S. J., Tarditi, A., & Chu, M. S., the NIMROD Team 2004, *J. Comput. Phys.*, 195, 355
- Sovinec, C. R., Schnack, D. D., Pankin, A. Y., Drennan, D. P., Tian, H., Barnes, D. C., Kruger, S. E., Held, E. D., Kim, C. C., Li, X. S., Kaushik, D. K., Jardin, S. C., the NIMROD Team 2005, *J. Phys. Conf. Ser.*, 16, 25
- Spitzer, L., & Härm, R. 1953, *Phys. Rev.*, 89, 977
- Stone, J. M., & Zweibel, E. G. 2009, *ApJ*, 696, 233
- Sullivan, B. P., & Bhattacharjee, A. 2009, arXiv:0905.4765

- Strauss, H. R. 1988, ApJ, 326, 412
- Sweet, P. A. 1958, in IAU Symp. 6, *Electromagnetic Phenomena in Cosmical Physics*, ed. B. Lehnert (Dordrecht: Kluwer) 123
- Syrovatsky, S. I. 1971, Sov. Phys. JETP, 33, 933
- Syrovatsky, S. I. 1981, ARA&A, 19, 163
- Taylor, J. B. 1986, Rev. Mod. Phys., 58, 741
- Tsuneta, S. 1996, ApJ, 456, 840
- ud-Doula, A., Townsend, R. H. D., & Owocki, S. P. 2006, ApJL, 640, L191
- Uzdensky, D. 2009, Phys. Plasmas, 16, 040702
- Walsh, R. W., & Ireland, J. 2003, Aston. Astrophys. Rev., 12, 1
- Wang, Y., Kulsrud, R., & Ji, H. 2008, Phys. Plasmas, 15, 122105
- Weisberg, J. M., Cordes, J. M., Kuan, B., Devine, K. E., Green, J. T., & Backer, D. C. 2004, ApJS, 150, 317
- Widrow, L. M. 2002, Rev. Mod. Phys., 74, 775
- Yamada, M., Levinton, F. M., Pomphrey, N., Budny, R., Manickam, J., & Nagayama, Y. 1994, Phys. Plasmas, 1, 3269
- Yamada, M., Ji, H., Hsu, S., Carter, T., Kulsrud, R., Bretz, N., Jobes, F., Ono, Y., & Perkins, F. 1997, Phys. Plasmas, 4, 1936
- Yamada, M., Ren, Y., Ji, H., Breslau, J., Gerhardt, S., Kulsrud, R., & Kuritsyn, A. 2006, Phys. Plasmas, 13, 2119
- Yan, M., Lee, L. C., & Priest, E. R., 1992, J. Geophys. Res., 97, 8277

Yin, L., & Winske, D. 2003, 10, 1595

Zhu, P., Sovinec, C. R., Hegna, C. C., Bhattacharjee, A., & Germaschewski, K. 2007, J.
Geophys. Res., 112, A06222

Zweibel, E. G., & Yamada, M. 2009, ARA&A, in press

Chapter 2

Global Axisymmetric Simulations of Two-Fluid Reconnection in an Experimentally Relevant Geometry

This chapter is adapted from: Murphy, N. A., & Sovinec, C. R. 2008, Phys. Plasmas, 15, 042313.

2.1 Introduction

Most two-fluid and particle-in-cell (PIC) simulations of reconnection are restricted to a simplified geometry (e.g., Birn et al. 2001), and most global simulations incorporating realistic geometry focus primarily on resistive MHD (e.g., Watanabe et al. 1999; Lukin et al. 2001; Lukin & Jardin 2003). The simulations presented in this chapter extend previous efforts by including two-fluid effects in global simulations of reconnection in an experimentally relevant geometry. Although this model does not capture all of the kinetic effects that may be important during reconnection (e.g., Daughton et al. 2006), it does allow a detailed investigation of the coupling between small scale Hall physics and the large scale magnetic field geometry.

The Magnetic Reconnection Experiment (MRX) (Yamada et al. 1997a) is located at the Princeton Plasma Physics Laboratory and is designed to study controlled nearly axisymmetric reconnection. The extensive list of results from this device include work on the shape of the current sheet (Yamada et al. 1997b), verification of a generalized Sweet-Parker model (Ji et al. 1998), studies of ion heating (Hsu et al. 2000; Hsu et al. 2001) and lower-hybrid drift turbulence (Carter et al. 2002a; Carter et al. 2002b), the measurement of the transverse and parallel Spitzer resistivities (Trintchouk et al. 2003; Kuritsyn et al. 2006), an investigation of electromagnetic fluctuations in the current sheet (Ji et al. 2004a; Ji et al. 2004b; Dorfman et al. 2006) active perturbation of the current sheet (Dorfman et al. 2006), and a study of the formation, stability, and sustainment of field-reversed configurations (Gerhardt et al. 2006; Gerhardt et al. 2007). A 2004 upgrade to the device gave MRX the capability to investigate lower collisionality plasmas (Ren et al. 2005; Yamada et al. 2006)

and to change the flux core separation (Kuritsyn 2005; Kuritsyn et al. 2007). Recent work has focused on two-fluid effects in reconnection, including observations of the quadrupole field (Ren et al. 2005; Yamada et al. 2006; Ren 2007; Ren et al. 2008) as well as symmetry breaking due to the Hall effect during counter-helicity push reconnection (Inomoto et al. 2006). The out-of-plane quadrupole magnetic field has also been observed during counter-helicity spheromak merging in the Swarthmore Spheromak Experiment (SSX) (Matthaeus et al. 2005) and in spacecraft observations of the Earth’s magnetosphere (e.g., Mozer et al. 2002).

MRX has been simulated by three other groups. Watanabe et al. (1999) report island formation during co-helicity merging with a spatially nonuniform resistivity. Lukin & Jardin (2003) use the TRIM code (TRIangular Magnetohydrodynamics; see Schnack et al. 1998) to simulate co- and counter-helicity pull reconnection in MRX. This group adds a ‘model Hall’ term which, due to restrictive time-step constraints, is limited to one-sixth of the true strength of the Hall term. Dorfman et al. (2008) perform PIC simulations of reconnection in MRX with a focus on the size and structure of the electron diffusion region rather than on the coupling between local and global effects. These simulations extend and complement previous work to fully include the Hall effect with a focus on the role of global effects during the reconnection process.

MRX, unlike the earlier reconnection experiments of Stenzel and Gekelman (1981), drives reconnection through toroidal flux cores. Cylindrical geometry effects would normally be expected to be unimportant because the width δ of the reconnection layer is much less than the major radius R , especially during pull reconnection. However, the simulations reported here show that cylindrical geometry has noticeable effects on the reconnection process. In pull reconnection, for example, the inboard (low radius) side of the current sheet

becomes depleted of density more quickly than the outboard (high radius) side due to the smaller available volume, resulting in asymmetric inflow. While most studies of reconnection either assume or find the process to be symmetric to a 180° rotation about the center of reconnection, some recent work has explicitly studied reconnection with asymmetric inflow (Ugai 2000; Kondoh et al. 2004; Swisdak et al. 2003; Linton 2006; Cassak & Shay 2007; Borovsky & Hesse 2007).

The choice of MRX as the basis for an investigation of the interplay between local and global effects in reconnection is advantageous due to the well-understood experimental setup and the availability of laboratory data. In addition, the plasma parameters are not too extreme for direct simulation. The goal of this chapter is not to simulate MRX in detail, but rather to use the geometry and setup of the device to investigate the role of global effects during the reconnection process.

Section 2.2 contains a description of the two-fluid and resistive MHD models used for these simulations of MRX. Section 2.3 provides an overview of the simulation setup as well as initial and boundary conditions. Technical modifications made to NIMROD are further discussed in Appendix A. Sections 2.4 and 2.5 present simulation results for antiparallel resistive MHD and two-fluid reconnection, respectively, and provide a discussion of the relevant physics. Section 2.6 contains details of two-fluid co- and counter-helicity simulations of reconnection in MRX. Conclusions for this chapter are included in Section 4.1.

2.2 Two-Fluid Model

As discussed in Section 1.4, the NIMROD (Non-Ideal Magnetohydrodynamics with Rotation, Open Discussion) code (Sovinec et al. 2004) solves the equations of two-fluid MHD cast in a single-fluid form. The solution is represented by a quadrilateral finite element

mesh in the poloidal plane and a finite Fourier series in the azimuthal direction. However, all simulations performed specifically for this chapter are axisymmetric. The semi-implicit leapfrog time advance used for the simulations reported in this chapter allows the full inclusion of the Hall term without a severe time step limitation (Sovinec et al. 2005; Schnack et al. 2006).

The combined Faraday/Ohm's Law used for two-fluid simulations is given by

$$\frac{\partial \mathbf{B}}{\partial t} = -\nabla \times \left(\eta \mathbf{J} - \mathbf{V} \times \mathbf{B} + \frac{\mathbf{J} \times \mathbf{B}}{ne} - \frac{\nabla p_e}{ne} \right). \quad (2.1)$$

The choice for resistivity of $\eta = 10^{-4} \Omega \cdot \text{m}$ ($\eta/\mu_0 = 80 \text{ m}^2 \text{ s}^{-1}$) corresponds to the parallel Spitzer resistivity for a plasma with an electron temperature of $T_e = 15 \text{ eV}$. A scalar electron pressure is assumed, so potentially important effects associated with the off-diagonal terms in the electron pressure tensor are absent. These missing effects may alter the structure of the electron diffusion region, although the reconnection rate is not greatly affected (Birn et al. 2001). Because the electron inertial length $c/\omega_{pe} \sim 1 \text{ mm}$ is small compared to a resistive skin depth of a few centimeters, electron inertia is neglected in these simulations. Investigations in the SSX device have also noted that in the reconnection region, the electron inertia term will be orders of magnitude smaller than the resistive term (Cothran et al. 2005). No hyperresistivity is used, leaving resistivity as the mechanism that breaks magnetic field lines.

For the resistive MHD simulations reported in Section 2.4, equation (2.1) reduces to

$$\frac{\partial \mathbf{B}}{\partial t} = -\nabla \times (\eta \mathbf{J} - \mathbf{V} \times \mathbf{B}). \quad (2.2)$$

Ampere's Law without displacement current is

$$\mu_0 \mathbf{J} = \nabla \times \mathbf{B}. \quad (2.3)$$

The divergence constraint is

$$\nabla \cdot \mathbf{B} = 0. \quad (2.4)$$

Because this condition is not met exactly by the numerical representation, a divergence cleaning technique is used (Sovinec et al. 2004). The momentum equation with viscosity is given by

$$\rho \left(\frac{\partial \mathbf{V}}{\partial t} + \mathbf{V} \cdot \nabla \mathbf{V} \right) = \mathbf{J} \times \mathbf{B} - \nabla p + \nabla \cdot \rho \nu \nabla \mathbf{V}. \quad (2.5)$$

For simplicity, the magnetic Prandtl number is chosen to be unity. Continuity is given by

$$\frac{\partial n}{\partial t} + \nabla \cdot (n \mathbf{V}) = \nabla \cdot D \nabla n. \quad (2.6)$$

The number density diffusivity D , chosen to be $80 \text{ m}^2 \text{ s}^{-1}$, is used primarily as a numerical smoothing parameter to ensure a well-behaved solution. Numerical tests show that for this value of D the central density of the current sheet in a typical simulation is reduced by $\lesssim 1\%$. For simplicity, the ion and electron temperatures are assumed to be equal. Temperature evolution is given by

$$\frac{n}{\gamma - 1} \left(\frac{\partial T}{\partial t} + \mathbf{V} \cdot \nabla T \right) = -\frac{p}{2} \nabla \cdot \mathbf{V} - \nabla \cdot \mathbf{q} + Q, \quad (2.7)$$

where

$$Q = \eta J^2 + \nu \rho \nabla \mathbf{V}^T : \nabla \mathbf{V}, \quad (2.8)$$

and

$$\mathbf{q} = -n \chi \nabla T, \quad (2.9)$$

with a thermal diffusivity of $\chi = 400 \text{ m}^2 \text{ s}^{-1}$ in most computations. A comparison of results with anisotropic heat conduction

$$\mathbf{q} = -n \left[\chi_{\parallel} \hat{\mathbf{b}} \hat{\mathbf{b}} + \chi_{\perp} (\mathbf{I} - \hat{\mathbf{b}} \hat{\mathbf{b}}) \right] \cdot \nabla T, \quad (2.10)$$

with $\chi_{\parallel} = 3 \times 10^5 \text{ m}^2 \text{ s}^{-1}$ and $\chi_{\perp} = 3 \times 10^2 \text{ m}^2 \text{ s}^{-1}$, where $\hat{\mathbf{b}}$ is a unit vector in the direction of the magnetic field, is discussed in Section 2.5.1.

NIMROD solves the equations of extended MHD, but does not contain all of the kinetic effects that are simulated in particle-in-cell codes. Notably absent are electron turbulence, particle demagnetization near field nulls, and acceleration of energetic particles. Nevertheless, other studies (e.g., Mandt et al. 1994) have shown that the reconnection rate is largely independent of the mechanism that breaks the frozen-in condition, so NIMROD is well-suited to investigate the interplay between local and global effects on the reconnection process. The two-fluid model used here has been successfully tested on a variety of benchmark problems, including the g-mode (Schnack et al. 2006) and the two-fluid tearing mode (Sovinec et al. 2006).

2.3 MRX Simulation Setup

The presence of dual flux cores requires that the computational domain be multiply connected. Hence it is untenable to use a logically rectangular mesh of quadrilateral finite elements to represent the poloidal plane. To generate the grid for MRX, the positions of the vertices of each element along the outer boundary are specified. The remaining interior element vertex positions are found through an iterative process where the new position of a vertex is found through a weighted average of the surrounding vertices. The weight function depends on position and is chosen to provide high resolution in regions of strong gradients (e.g., the current sheet and the quadrupole field regions). Different weight functions are chosen for different modes of operation and for different physical models. A low resolution version of the finite element grid used for two-fluid pull reconnection is shown in Figure 2.1. For cylindrical geometry simulations, an approximation to the actual flux

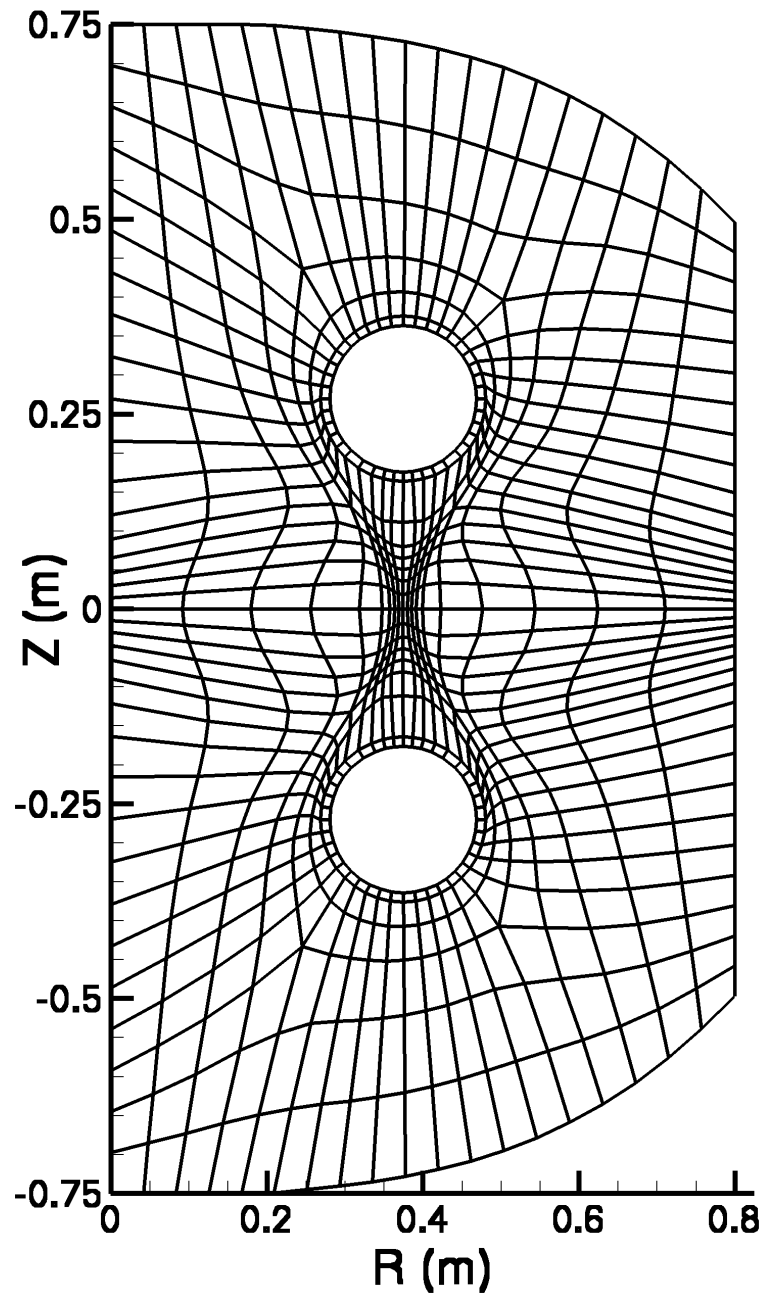


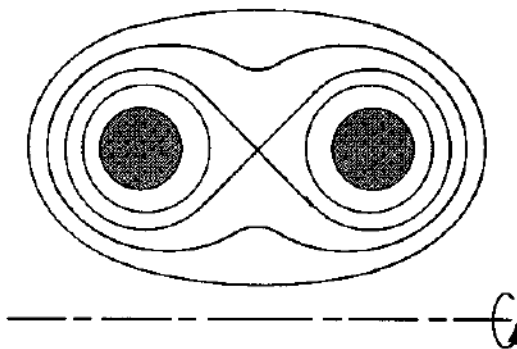
Fig. 2.1.—: A low resolution version of the finite element grid used for cylindrical geometry simulations of two-fluid pull reconnection in MRX. Note that high resolution is present both in the reconnection region and along the expected position of the quadrupole field.

conserver shape is used as the outer boundary. Some simulations use linear geometry in order to isolate the effects of cylindrical geometry and to simplify the analysis. In particular, Figures 2.7, 2.8, 2.13, 2.15, 2.16, 2.17, and 2.19 all show results from linear geometry computations. For these simulations, a rectangular outer boundary is used. The flux cores are included in each of these geometries. All simulations presented here are axisymmetric and use bicubic finite element basis functions which are fourth order accurate when solutions are sufficiently smooth. Further details on the establishment of the grid for simulations of MRX are discussed in Appendix A.

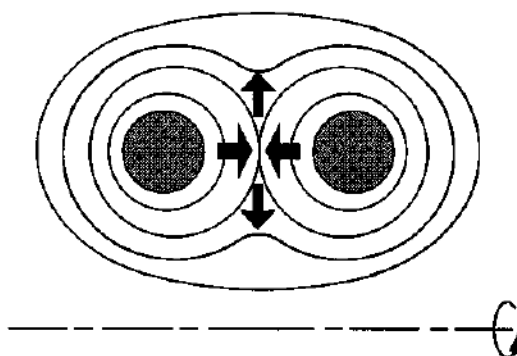
The modes of operation of MRX are shown in Figure 2.2. In ‘pull’ reconnection, magnetic flux surfaces are pulled into the flux cores. This setup is reminiscent of reconnection in the Earth’s magnetotail and in coronal mass ejections. In the experiment, this results in a reconnection sheet with radial inflow and axial outflow. In ‘push’ reconnection, magnetic flux surfaces are pushed out of the flux cores. This results in axial inflow and radial outflow. A third mode of operation involving spheromak merging is not simulated in this work. The majority of published results from the MRX device is from the pull mode of operation.

The initial magnetic field is set up through coils at the center of each flux core with positions and current $(R, Z, I) = (37.5 \text{ cm}, \pm 27 \text{ cm}, -50 \text{ kA})$, with vertical field coils at $(R, Z, I) = (89 \text{ cm}, \pm 121 \text{ cm}, 134 \text{ kA})$ for simulations with cylindrical geometry. This sets a vacuum X-point at the midpoint between the two flux core positions. The initial field for these simulations is purely poloidal. An azimuthal electric field is applied on the flux core surfaces to induce poloidal magnetic field. Depending on the direction, this electric field drives either push or pull reconnection. In the experiment, some azimuthal field is always generated during the plasma formation process; however, no azimuthal field is induced directly by the flux cores in null-helicity simulations. The electric field is linearly ramped

No reconnection
when $dl_{PF}/dt = 0$



"Push" reconnection
when $dl_{PF}/dt > 0$



"Pull" reconnection
when $dl_{PF}/dt < 0$

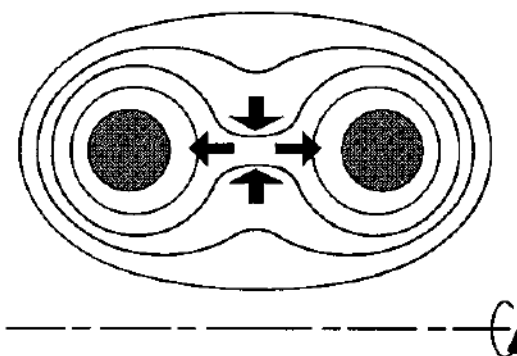


Fig. 2.2.—: The push and pull modes of operation in MRX. [Reprinted with permission from Yamada et al. 1997, Phys. Plasmas, 4, 1936. Copyright 1997, American Institute of Physics.]

up from zero to the full value given in Table 2.1 over $0.1 \mu\text{s}$. For the co- and counter-helicity simulations of push reconnection reported in Section 2.6, a poloidal electric field is applied to the flux core surfaces to induce an azimuthal magnetic field in addition to the azimuthal electric field. The duration of reconnection in the experiment is $\sim 50 \mu\text{s}$, and the simulations represent $15 - 20 \mu\text{s}$ of this period. The magnitude of the applied voltage is chosen to give a reconnecting electric field comparable to that observed in experiment. Typical simulation parameters are shown in Table 2.1.

Like previous simulations of MRX (Lukin & Jardin 2003; Watanabe et al. 1999), resistivity is enhanced around the flux core surfaces. The diffusivity profile used in this work is of the form

$$\frac{\eta}{\eta_0} = 1 + C_\eta \left[\exp\left(-\frac{(r_1 - r_c)^2}{(Ar_c)^2}\right) + \exp\left(-\frac{(r_2 - r_c)^2}{(Ar_c)^2}\right) \right], \quad (2.11)$$

where r_1 and r_2 are the distances from a point in the domain to the centers of the two flux cores and $r_c = 9.4 \text{ cm}$ is the flux core minor radius. The choices of the coefficients A and C_η are $A = 0.3$ and $C_\eta = 3$. Additional diffusivity shaping is used along the exterior of the domain to prevent the development of unresolved boundary layers. No diffusivity enhancement is used in the reconnection region in any of the simulations reported in this chapter. Apart from the position dependence described above, the resistivity η is held constant and is not a function of temperature or current density.

The simulations assume perfectly conducting no-slip boundary conditions along the exterior wall. The normal component of velocity on the flux core surfaces is given by the $\mathbf{E} \times \mathbf{B}$ drift. The number density on the flux core surfaces is kept at the initial value of number density in the simulation. This is a reasonable approximation because the flux core surface can act both as a sink and source of material in the experiment. For consistency

Table 2.1. Simulation parameters

Parameter	Value
Initial Number Density	$5 \times 10^{19} \text{ m}^{-3}$
Initial Temperature	15 eV
Ion Species	D ⁺
Flux Core Loop Voltage (V_{loop})	1000 V
Characteristic Magnetic Field	350 G
Characteristic Length Scale ^a	25 cm
Characteristic Alfvén Speed (V_A)	75 km s ⁻¹
Characteristic Sound Speed (V_S)	35 km s ⁻¹
Thermal Diffusivity (χ)	400 m ² s ⁻¹
Resistivity (η)	$10^{-4} \Omega \cdot \text{m}$
Viscosity (ν)	80 m ² s ⁻¹
Lundquist Number (S)	240
Ion Inertial Length (c/ω_{pi})	4.5 cm

^aChosen to be an intermediate value between the current sheet length and the system size.

with much of the work reported by the experiment (e.g., Ren et al. 2005; Yamada et al. 2006), the ion species is assumed to be deuterium. With this choice of species, the ion inertial length is given by $c/\omega_{pi} = 4.5$ cm.

2.4 Resistive MHD Null-Helicity Simulations

This section contains an overview and discussion of simulations of resistive MHD reconnection for both the push and pull modes of operation. Resistive MHD cases reproduce many global effects observed in the experiment and also provide instructive comparisons with the two-fluid simulations discussed in Section 2.5. Because the initial magnetic field is purely poloidal in these two-dimensional simulations and the applied electric field is purely azimuthal, no mechanism in the resistive MHD framework exists to generate in-plane currents or out-of-plane magnetic field. Unless otherwise noted, all figures in this section are from $t = 11.2 \mu\text{s}$ after the start of each simulation, when the current sheet is well developed.

2.4.1 Resistive MHD Pull Reconnection

Simulations of resistive MHD pull reconnection with the plasma parameters listed in Table 2.1 result in a Sweet-Parker-like current sheet. The azimuthal current density and plasma pressure are shown in Figure 2.3. The width δ of the current sheet is found through a fit to the function

$$B_Z(R) = B_0 \tanh\left(\frac{R - R_0}{\delta}\right) + b_1(R - R_0). \quad (2.12)$$

The last term takes into account that B_Z does not approach a constant far from the current sheet. This is similar to the equation used in Yamada et al. (2000) to describe the neutral sheet profile. The length of the current sheet $L_{0.5}$ is defined as the distance in the outflow

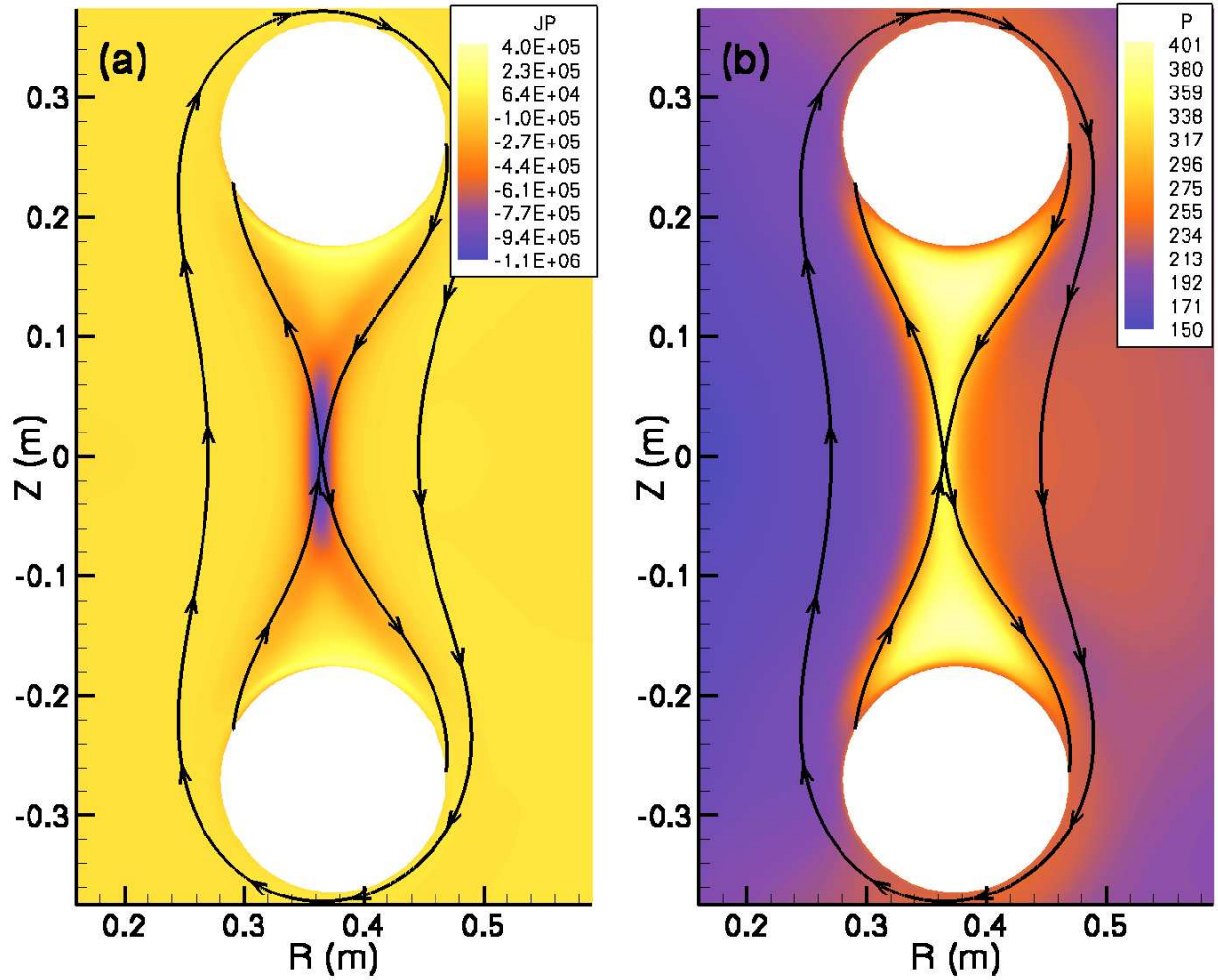


Fig. 2.3.—: Simulations of pull reconnection using a resistive MHD model show the development of Sweet-Parker-like current sheets. Shown are (a) the azimuthal current density and (b) the plasma pressure (in SI units) along with streamtraces of the magnetic field.

direction between the peak of the reconnecting current and where the reconnecting current density reaches half of the peak value. For Figure 2.3, $\delta \approx 1.2$ cm and $L_{0.5} \approx 8$ cm. The outflow velocity is ~ 20 km s⁻¹. This is noticeably slower than $V_A \sim 75$ km s⁻¹ expected from Sweet-Parker theory due to both viscosity and the high downstream pressure [seen in Figure 2.3(b)] that results from outflow being confined between the separatrices and the flux cores. For the value of viscosity used in this chapter ($\text{Pm} = 1$), the peak outflow speed is ~ 25 – 30% slower than in an otherwise identical simulation with $\text{Pm} = 0.0625$. The viscous limit is considered using a simulation with $\text{Pm} = 15$, using a viscosity comparable to the unmagnetized Braginskii value. In this case, the peak outflow is ~ 40 – 50% slower than the $\text{Pm} = 0.0625$ case. For $\text{Pm}=1$ simulations reported in this chapter, the effects of pressure on the outflow are therefore more important than the effects of viscosity. The ratio of downstream and central pressure to the inflow pressure produced in the simulation (roughly a factor of 2) is comparable to the ratio of densities shown in Figure 8 of Ji et al. (1999).

The inboard side of the current sheet has noticeably lower plasma pressure than the outboard side during pull reconnection in cylindrical geometry, as evident in Figure 2.3(b). This is a consequence of the lower volume on the inboard side than on the outboard side and leads to asymmetric inflow with a radially inward drift of the current sheet, which is discussed in more detail later in the section. The relatively low inboard pressure has also been observed in experiment (Kuritsyn 2005). With a sound speed of approximately 35 km s⁻¹, pressure does not equilibrate along magnetic field lines that encircle the flux cores from one inflow region to the other on the time scale of the driven transient. The flow stagnation point and the field null are not colocated during reconnection, as shown in Figure 2.4.

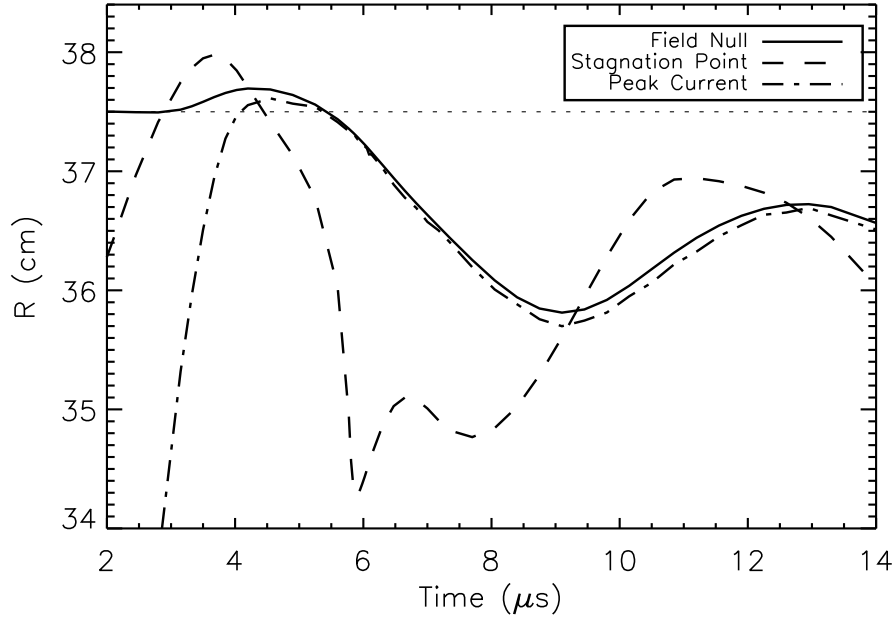


Fig. 2.4.—: The position of the magnetic field null, the flow stagnation point, and the maximum current density as a function of time during a null-helicity resistive MHD simulation of pull reconnection. Similar behavior is observed when the Hall term is included.

2.4.2 Resistive MHD Push Reconnection

Simulations of resistive MHD push reconnection in MRX's geometry (see Figure 2.5) show a Sweet-Parker-like current sheet similar to those seen in pull reconnection. For most of the physical parameters tested, both the length and width of the current sheet are shorter during push reconnection than during pull reconnection with the same magnitude of applied voltage. In Figure 2.5, $\delta \approx 0.7$ cm and $L_{0.5} \approx 4.3$ cm, as found through the push reconnection analogue to equation (2.12). The inflow is symmetric about $Z = 0$, whereas the outflow is asymmetric in the radial direction due to cylindrical geometry effects. The position of

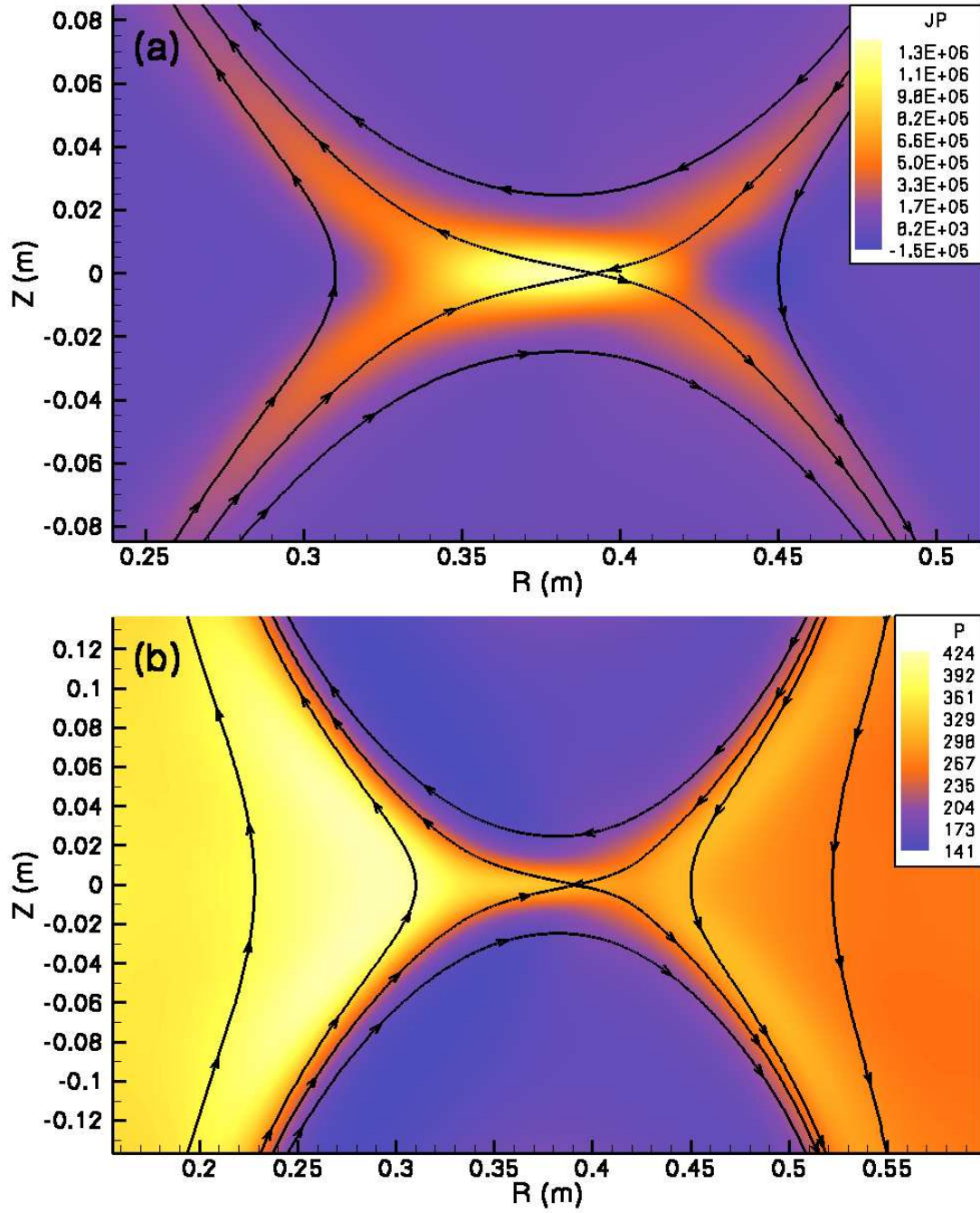


Fig. 2.5.—: Simulations of resistive MHD push reconnection in cylindrical geometry, showing (a) azimuthal current density and (b) plasma pressure, along with streamtraces of the poloidal magnetic field.

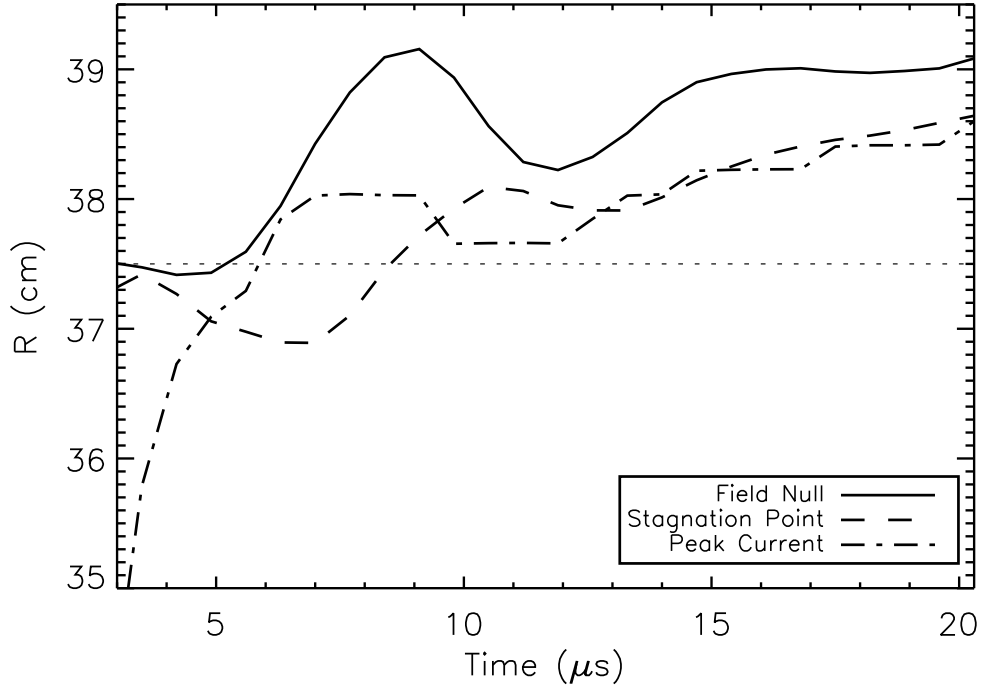


Fig. 2.6.—: The position of the magnetic field null, the flow stagnation point, and the maximum current density as a function of time during a null-helicity resistive MHD simulation of push reconnection.

the field null in Figure 2.5 is near the outboard side of the current sheet. The inboard downstream region has significantly higher plasma pressure than the outboard downstream region. The magnetic field null and flow stagnation point are in general not colocated (see Figure 2.6). The magnetic field null is located at higher radii than the flow stagnation point due to the presence of high downstream pressure on the inboard side of the current sheet. The outflow velocity patterns on the two sides of the X-point is not symmetric due both to cylindrical geometry effects and the significant buildup of plasma pressure in the inboard downstream region.

2.4.3 Discussion of Resistive MHD Results

2.4.3.1 Asymmetric Effects Associated with Cylindrical Geometry

In experiment and in previous simulations (Lukin & Jardin 2003), it has been noted that the current sheet moves radially inward at a rate of a few kilometers per second during pull reconnection. Quantitatively consistent radial motion is present in the null-helicity simulations reported in this chapter. The radial position of the magnetic field null, the flow stagnation point, and the peak azimuthal current density are all shown in Figure 2.4. It is apparent that reconnection in these simulations occurs in a moving reference frame. Starting around $5 \mu\text{s}$, the field null moves inward at a maximum rate of 6 km s^{-1} before commencing radially outward motion at around $9 \mu\text{s}$. The flow stagnation point and the magnetic field null are not at the same position, except around times when the instantaneous velocity of the field null is zero. When the field null has an inward (outward) motion, the stagnation point is at a lower (higher) radius. The peak current density tends to be at a slightly lower radius than the field null.

To understand the cause of the radial drift, it is important to note simulation conditions where it does not occur. First, this radial drift in position does not occur in $\beta = 0$ simulations, indicating that pressure effects are necessary. Second, this drift does not occur in MRX-like simulations in linear geometry with symmetric boundaries and finite β . In this case, the field null, the flow stagnation point, and the peak current density are colocated at the midpoint between the two flux cores. Comparing the simulation results, a large scale pressure gradient between the inboard and outboard sides of the reconnection region only develops in the finite β cylindrical geometry case where approximately even inflow from both sides of the current sheet depletes density from the inboard side more quickly than

from the outboard side. This leads to the outboard side of the current sheet having a peak pressure which is 25-50% higher than on the inboard side, as can be seen in Figure 2.3(b). This leads to a net inward radial force that pushes the current sheet to lower radii. An additional consequence is that the flow stagnation point is on the inboard side of the field null during inward motion.

As the current sheet moves inward, the vertical magnetic field is compressed. Eventually, this causes the outward directed force associated with magnetic pressure to exceed the inward directed force associated with plasma pressure. This leads to a reversal of the motion of the current sheet around $t = 9 \mu\text{s}$, as seen in Figure 2.4. As the current sheet moves outward, the force associated with magnetic pressure decreases until around $t = 13 \mu\text{s}$ when the current sheet motion reverses once more. The characteristic time scale for this process is comparable to the period of a standing Alfvén wave with nodes at the flux cores. While inward motion of the current sheet is observed during pull reconnection in experiment (e.g., Dorfman et al. 2006), multiple reversals of the current sheet motion are atypical.

Rather than the asymmetric inflow that is present in simulations of pull reconnection, it is the outflow that is asymmetric during push reconnection. A pressure buildup on the inboard side of the current sheet develops due to the same volume effects leading to the pressure cavity in pull reconnection. As a result of this pressure buildup, the X-point is located near the outboard side of the current sheet [as seen in Figure 2.5(a)]. Normally, such a pressure buildup would be expected to suppress inward directed outflow. Because the X-point is located near the outboard side of the current sheet, the magnetic tension on the inboard side of the X-point is strong enough to counter the pressure gradient. The magnetic tension on the outboard side of the current sheet is correspondingly weaker, but the pressure force is directed radially outward throughout the current sheet and hence facilitates faster

radially outward directed outflow. The net result is that the peak inward and outward directed outflow velocities are similar ($\sim 20 \text{ km s}^{-1}$), although at the observed time the inward directed outflow is slightly faster. The flux of material from both sides of the current sheet is approximately the same.

2.4.3.2 Pressure Effects, Flux Availability, and Reconnection Rate

Experimental results from MRX show that the Sweet-Parker model must be modified to take into account the effects of downstream pressure (Ji et al. 1999). A conclusion from this work is that outflow confinement affects how quickly the reconnection process can occur. In pull reconnection, plasma is confined between the separatrices and the flux cores. The low available volume results in the high downstream pressure buildup seen in Figure 2.3(b), which in turn reduces the reconnection rate. The large downstream pressure of 400 Pa is comparable to the upstream magnetic pressure of 360 Pa and much larger than the initial pressure of 240 Pa or the inflow pressures of 150 Pa (inboard) and 230 Pa (outboard). In push reconnection, downstream plasma is able to expand along the field lines outside the separatrices that surround the flux cores. While a large pressure maximum of 420 Pa is present on the inboard side of the current sheet [see Figure 2.5(b)], pressure facilitates outflow on the outboard side rather than impeding it. Hence, pressure effects have less of an impact on the push reconnection rate than the pull reconnection rate.

The time evolution of the reconnection process is also affected by the availability of poloidal flux. In pull reconnection, the amount of flux able to be reconnected is limited by the amount of flux initially available. In push reconnection, this limit does not exist because flux is continually injected into the system via the flux core boundary conditions. This consideration and the confinement properties of the two modes of operation both help

explain why push reconnection is quicker than pull reconnection.

In Figures 2.3(a) and 2.5(a), four arms of azimuthal current density that extend from the current sheet are apparent. These arms exist along the separatrices and are coincident with the strong pressure gradients between the upstream and downstream regions. The poloidal magnetic field is mostly parallel to the closely packed pressure contours. These arms are regions of high diamagnetic current density, $\mathbf{J}_* = -(\nabla p \times \mathbf{B})/B^2$, which develops through the evolving force balance and facilitates confinement of downstream plasma. The azimuthal current along these arms is in the same direction as the current in the reconnection layer.

2.4.3.3 Scalings with Driving Voltage and Resistivity

Global effects (such as driving voltage) and local effects (such as resistivity) both play a role in determining the rate of reconnection and the characteristics of the reconnection layer. Figures 2.7 and 2.8 show the results of scaling studies for resistivity η and driving voltage strength V_{loop} measured at $t = 11.2 \mu\text{s}$ when the current sheet is well developed (see Section 2.5.3.1 for a discussion of the reconnection rate as a function of time). The simulations use linear geometry to preserve symmetries and simplify the analysis, but still include the flux cores.

The value for δ is found by fitting the resulting axial magnetic field at $Z = 0$ to the function $B_Z(R) = -B_0 \tanh[(R - R_0)/\delta] + b_1 R$ for pull reconnection and $B_R(Z) = -B_0 \tanh[Z/\delta] + b_1 Z$ for push reconnection (e.g., Yamada et al. 2000). As mentioned previously, $L_{0.5}$ is the distance in the outflow direction between the location of peak out-of-plane current density and where the out-of-plane current density reaches half of its strongest value.

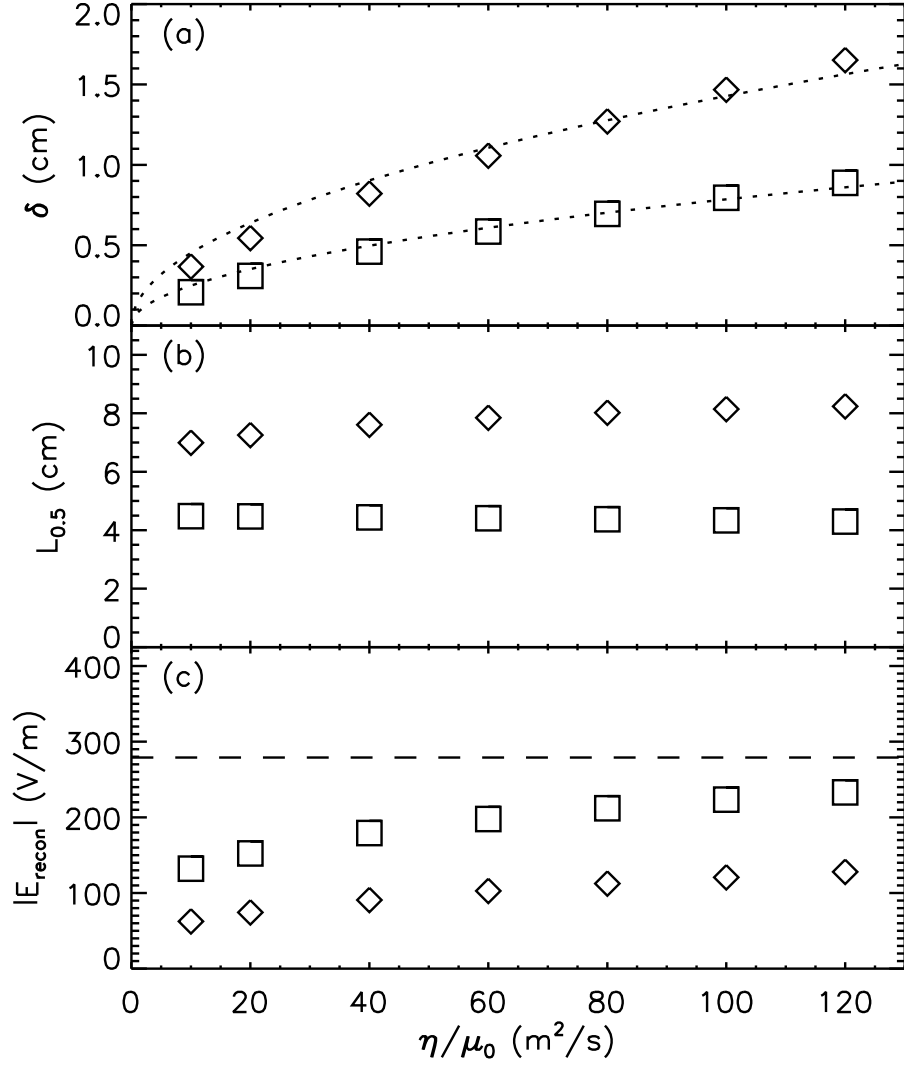


Fig. 2.7.— Comparisons of the (a) thickness δ , (b) length $L_{0.5}$, and (c) reconnecting electric field strength E_{recon} at $t = 11.2 \mu\text{s}$ for linear geometry simulations of push (squares) and pull (diamonds) reconnection using different values of resistivity. For this figure, $V_{\text{loop}} = 1000 \text{ V}$. The dotted lines represent the Sweet-Parker scaling $\delta \propto \eta^{1/2}$ for constant L , V_{in} , and B_{in} , and the dashed line represents the electric field E_{xvac} that would exist at the X-point in the absence of plasma.

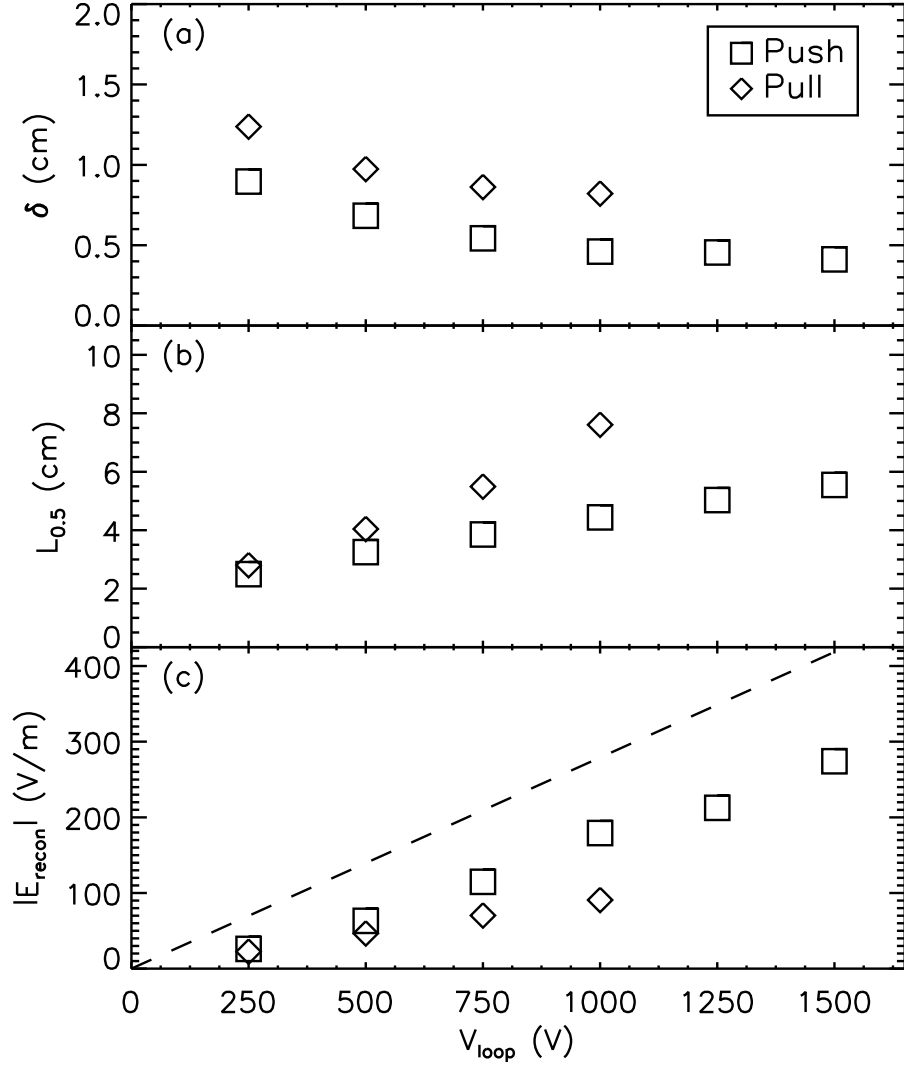


Fig. 2.8.—: Comparisons of the (a) thickness δ , (b) length $L_{0.5}$, and (c) reconnecting electric field strength E_{recon} at $t = 11.2 \mu\text{s}$ for linear geometry simulations of push (squares) and pull (diamonds) reconnection using different driving voltage strengths. The current sheet width decreases while the current sheet length and reconnecting electric field both increase. For this figure, $\eta/\mu_0 = 40 \text{ m}^2 \text{ s}^{-1}$. The dashed line represents E_{xvac} as a function of driving voltage.

In Figure 2.7(a), the relation $\delta \propto \eta^{1/2}$ is seen to be valid for both push and pull reconnection. The length $L_{0.5}$ is seen to be nearly constant over an order of magnitude in η in Figure 2.7(b), indicating that the length is set by global parameters rather than local parameters in resistive MHD with uniform diffusivity. This is in contrast to experimental results in which the quantity ηL is found to be approximately constant and anomalous resistivity effects cannot be ignored (Kuritsyn et al. 2007).

The aspect ratio of the current sheet is similar for both push and pull reconnection, but the physical dimensions are larger for pull reconnection. The reconnecting electric field is shown in Figure 2.7(c) and is compared to the electric field E_{xvac} that would exist at the X-point in the absence of plasma. For both linear and cylindrical geometry, E_{xvac} is found through very low Lundquist number simulations ($S \ll 1$) with equivalent drive. The push reconnection rate is higher than the pull reconnection rate due to the effects of geometry and downstream pressure. The difference between the actual reconnection rate and E_{xvac} is due to the finite impedance of the plasma. For a steady-state model, the reconnecting electric field strength by definition must be E_{xvac} ; however, a true steady state cannot exist in this configuration due to the inductive drive, ohmic and viscous heating, and outer boundary conditions.

Figure 2.8 shows δ , $L_{0.5}$, and E_{recon} as functions of driving voltage. It is apparent that driving voltage has a strong effect on each of these parameters. The width in Figure 2.8(a) decreases with stronger driving voltage, but for strongly driven reconnection, δ becomes less dependent on V_{loop} . In contrast to Figure 2.7(b), Figure 2.8(b) shows a strong dependence of the length of the current sheet on the driving voltage. This highlights the importance of global effects rather than local effects in determining the length of the current sheet in a resistive MHD model. The reconnecting electric field is found to be roughly proportional

to V_{loop} in Figure 2.8(c), although still below E_{vac} . During pull reconnection with $V_{\text{loop}} \gtrsim 1200$ V, the length of the current sheet becomes large enough that downstream pressure near the flux core surfaces is able to overcome tension and produce flows that feed back on the current sheet, resulting in reconnection being suppressed.

2.5 Two-Fluid Null-Helicity Simulations

This section contains a discussion of two-fluid simulations where the Ohm's law is $\mathbf{E} + \mathbf{V} \times \mathbf{B} = \eta \mathbf{J} + (\mathbf{J} \times \mathbf{B} - \nabla p_e) / ne$. The inclusion of the Hall term in the generalized Ohm's law breaks MHD symmetries, and it is now possible to generate out-of-plane magnetic field during null-helicity reconnection. In particular, all null-helicity cases show the quadrupole magnetic field signature of two-fluid reconnection. This section provides an overview of simulations of two-fluid pull and push reconnection, compares the characteristics of two-fluid reconnection to resistive MHD reconnection, and discusses the quadrupole shape and the nature of the electron outflow.

2.5.1 Two-Fluid Pull Reconnection

Two-fluid pull reconnection has been studied extensively in the MRX device, resulting in the clearest detections to date of the quadrupole field signature of two-fluid reconnection in a laboratory device (Ren et al. 2005; Yamada et al. 2006; Ren 2007). An example quadrupole for a deuterium discharge is seen in Figure 2.9(a). Typical measured values from experiment are a maximum quadrupole field strength of ~ 50 - 100 G and a reconnecting electric field of ~ 100 V/m (Yamada et al. 2006). There is a tendency for the outboard half of the quadrupole to peak closer to the X-point than the inboard half.

Figures 2.9(b) and 2.10 show simulation results from two-fluid pull reconnection $11.2 \mu\text{s}$

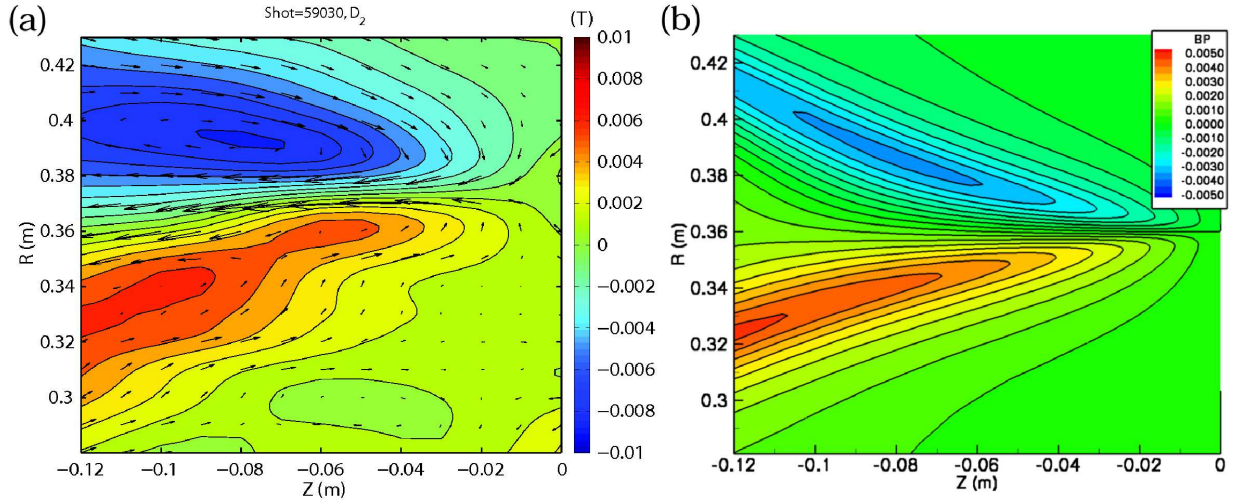


Fig. 2.9.—: (a) Experimental results showing azimuthal magnetic field contours along with electron velocity vectors during pull reconnection in a typical deuterium discharge in MRX, courtesy of Y. Ren (Ren 2007). (b) A closeup of azimuthal magnetic field contours during a simulation of two-fluid pull reconnection. Note the difference in the orientation of this figure with respect to the other figures in this chapter.

after the start of the simulation. At this time the maximum azimuthal field strength is 60 G and the reconnecting electric field is 138 V/m. Due to cylindrical geometry effects, the quadrupole is not symmetric to a 180° rotation about the X-point. Similar to experiment, the inboard lobes peak near the flux core surfaces, whereas the outboard lobes peak near the X-point. As in the resistive MHD case, there is a region of low plasma pressure on the inboard side of the current sheet. The buildup of pressure in the outflow region between the separatrices and the flux cores is similar to the MHD result. The separatrices are coincident with the quadrupole field, the region of strongest pressure gradients, and the border between

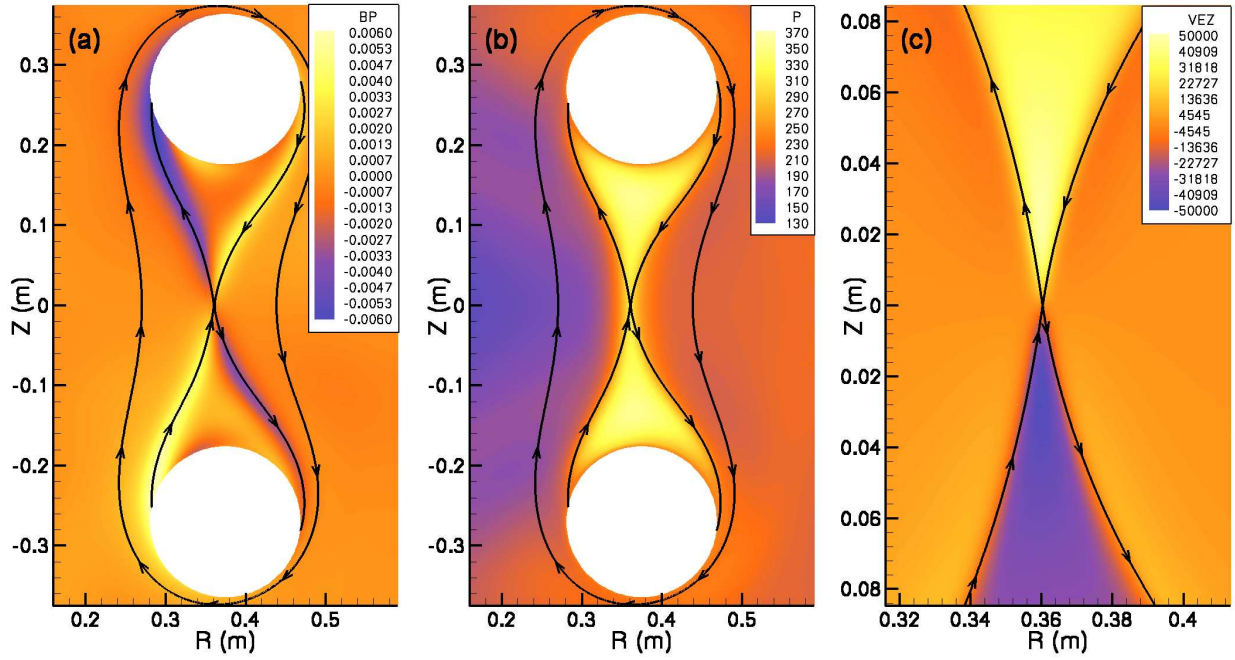


Fig. 2.10.—: Simulation results for two-fluid null-helicity pull reconnection with the geometry of MRX, showing (a) the azimuthal magnetic field, (b) pressure contours, and (c) the outflow component of the electron velocity, V_{eZ} . The three images also include streamtraces of the poloidal magnetic field. The separatrix is colocated with the quadrupole field and the boundary between the low-pressure inflow and high-pressure outflow regions.

the electron inflow and the electron outflow.

To gauge the impact of parallel heat conduction, simulations using realistic collisional thermal diffusivities of $\chi_{\parallel} = 3 \times 10^5 \text{ m}^2 \text{ s}^{-1}$ and $\chi_{\perp} = 3 \times 10^2 \text{ m}^2 \text{ s}^{-1}$ are compared to simulations using isotropic heat conduction with the thermal diffusivity of $\chi = 400 \text{ m}^2 \text{ s}^{-1}$ listed in Table 2.1. Comparisons are made at $t = 11.2 \mu\text{s}$, after the current sheet is well developed. The range in temperatures in the isotropic simulation is roughly 12 to 19 eV, but is reduced to 14 to 16 eV when strongly anisotropic heat conduction is used. However, pressure and density fields differ by $\lesssim 12\%$ between the two simulations. The reconnection rate is 8% stronger in the anisotropic case. Because pressure gradients in these simulations are driven primarily by variations in density, changing the model of thermal conduction induces only modest changes in the simulation results.

2.5.2 Two-Fluid Push Reconnection

Although the quadrupole field has not been observed during the push mode of operation in experiment, comparing simulations of push and pull reconnection helps gauge the importance of global effects on the reconnection process. The out-of-plane quadrupole field that develops is seen in Figure 2.11. As in the case for two-fluid pull reconnection, the quadrupole exists along the separatrices, which also form the boundary between the high pressure downstream region and the low pressure upstream region. The width of the quadrupole arms are noticeably smaller than in pull reconnection, and the separatrices surround the flux cores. Throughout the reconnection region there are bulk plasma flows in the azimuthal direction. The peak flow strength is typically $6 - 8 \text{ km s}^{-1}$ and is directed in the same direction as the reconnecting current.

As in the resistive MHD case, the outflow is asymmetric. Pressure buildup on the

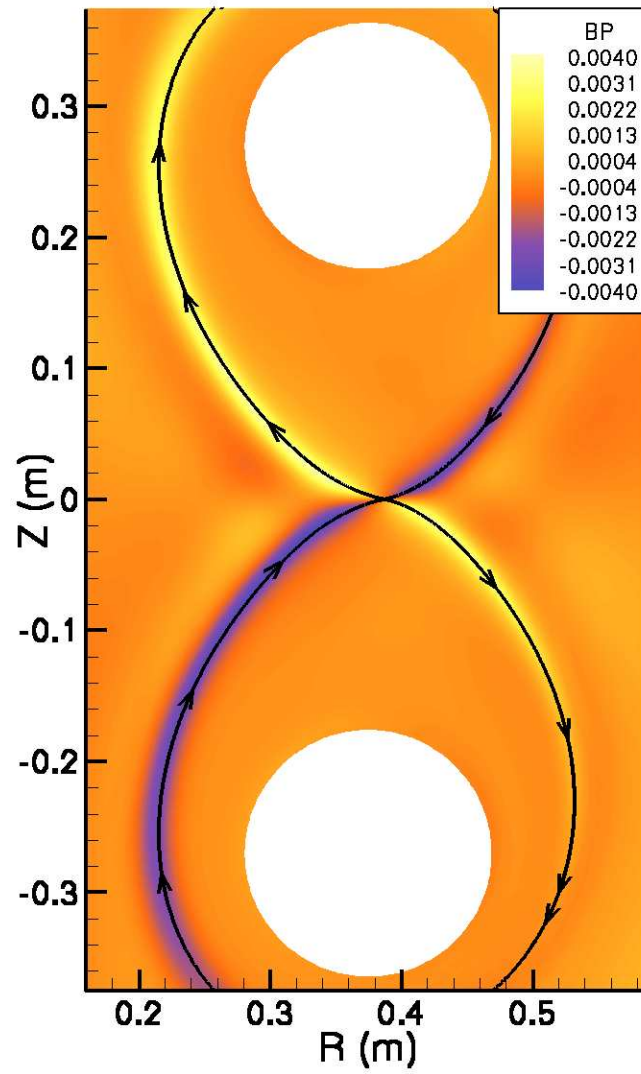


Fig. 2.11.—: Azimuthal magnetic field contours with a poloidal magnetic field streamtrace during a simulation of two-fluid push reconnection.

inboard side due to the lesser volume pushes the X-point radially outward, leading to strong tension forces on the inboard side that overcome the stronger pressure gradient. The outward directed outflow is slightly faster than the inward directed outflow. Late in the simulation and despite the asymmetric outflow, reconnection occurs as quickly as it is driven.

2.5.3 Discussion of Two-Fluid Results

2.5.3.1 Comparison with Resistive MHD Reconnection

Many of the same effects that were discussed in Section 2.4 are also present in two-fluid simulations. The position of the current sheet shows a time dependence which is similar to that in the resistive MHD case. This is not unexpected since the pressure asymmetries depend on volume effects which are present regardless of physical model. The diamagnetic arms of azimuthal current density are also present in Hall MHD simulations, coincident with the separatrices and the out-of-plane quadrupole field.

The most basic comparison between two-fluid and resistive MHD reconnection is the reconnection rate. Figure 2.12 shows the reconnection rate as a function of time for the simulations discussed in Sections 2.4 and 2.5. For a given mode of operation, the two-fluid simulation always has a stronger reconnecting electric field than the corresponding resistive MHD simulation. Additionally, for a given physical model, push reconnection is always quicker than pull reconnection. Immediately after reconnection commences, the two-fluid pull reconnection rate follows the two-fluid push reconnection rate closely. However, once effects associated with downstream pressure and flux availability limitations become important, the two-fluid pull reconnection rate levels off. After early times in these simulations, the mode of operation is more important in determining the reconnection rate than the

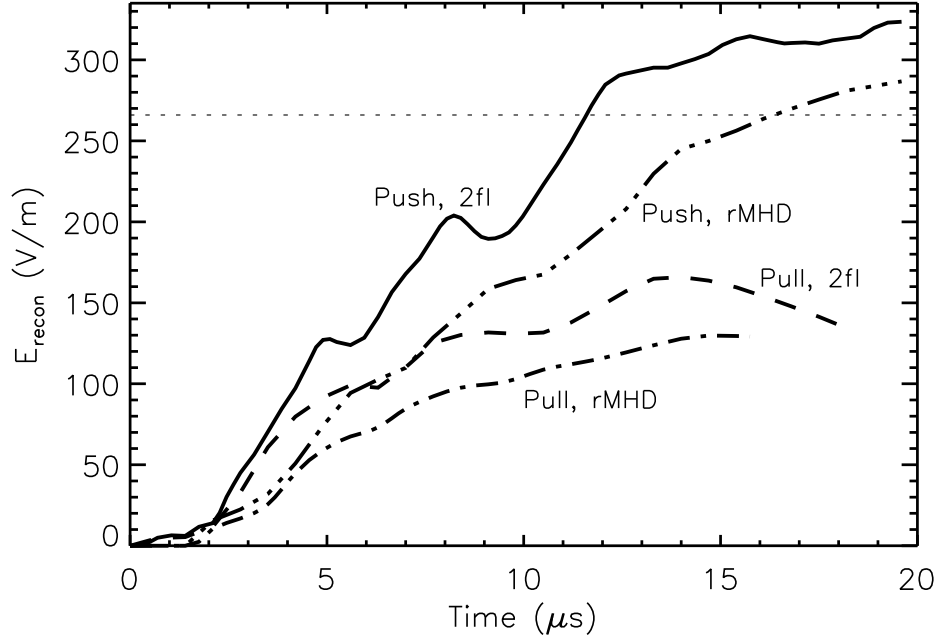


Fig. 2.12.—: The reconnecting electric field strength E_{recon} as a function of time for resistive MHD and two-fluid push and pull reconnection. The dotted line shows the electric field strength E_{xvac} that would exist at the initial X-point in the absence of plasma.

inclusion of two-fluid effects in the generalized Ohm's law.

Also plotted in Figure 2.12 is the electric field strength E_{xvac} that would exist at the X-point were the plasma not present. At $12 \mu\text{s}$, the reconnecting electric field for two-fluid push reconnection exceeds E_{xvac} , but immediately begins to level off. Because of the pileup of flux at previous times, the reconnection rate can exceed E_{xvac} for some time. After an initial transient, reconnection is essentially occurring as quickly as it is driven. Effects associated with downstream pressure and flux availability prevent the reconnecting electric field strength from approaching E_{xvac} during simulations of pull reconnection.

2.5.3.2 Azimuthal Flows

Azimuthal flows are present in simulations of both two-fluid push and pull reconnection with peak magnitudes of up to $V_i \sim 20 \text{ km s}^{-1}$. The flow is in the same direction as the reconnecting current and is almost the magnitude of the diamagnetic drift velocity. Experimental results during pull reconnection with Helium have shown a peak azimuthal velocity of several kilometers per second with the rotation predominantly on the outboard side of the current sheet (Hsu et al. 2001), whereas results with Hydrogen show the azimuthal flow peaking near the current sheet center with flows up to 12 km s^{-1} .

2.5.3.3 Electron Velocity Profile

The separation of electron and ion flows plays an important role in two-fluid reconnection, so it is important to compare V_e profiles with experiment. Figure 2.10(c) shows contours of the outflow component of electron velocity during two-fluid pull reconnection, V_{eZ} . The peak electron speed occurs at very short distances from the X-point along each of the outflow paths. This is expected for two-fluid null-helicity reconnection. The net flux of electrons at each value of Z in this region is approximately constant, which can be interpreted as a direct result of whistler physics controlling the shape of the reconnection outflow. As the length scale perpendicular to the outflow decreases closer to the X-point, the outflow velocity increases proportionately.

Experimental results have found that the electron outflow is superAlfvénic and peaks at a distance of $1 - 1.5 c/\omega_{pi}$ away from the X-point (Ren 2007). Figure 2.13(a) shows a comparison of the electron outflow profiles between a linear geometry simulation of two-fluid pull reconnection and experimental data. In contrast to experiment, the peak outflow in simulation is located very close to the X-point.

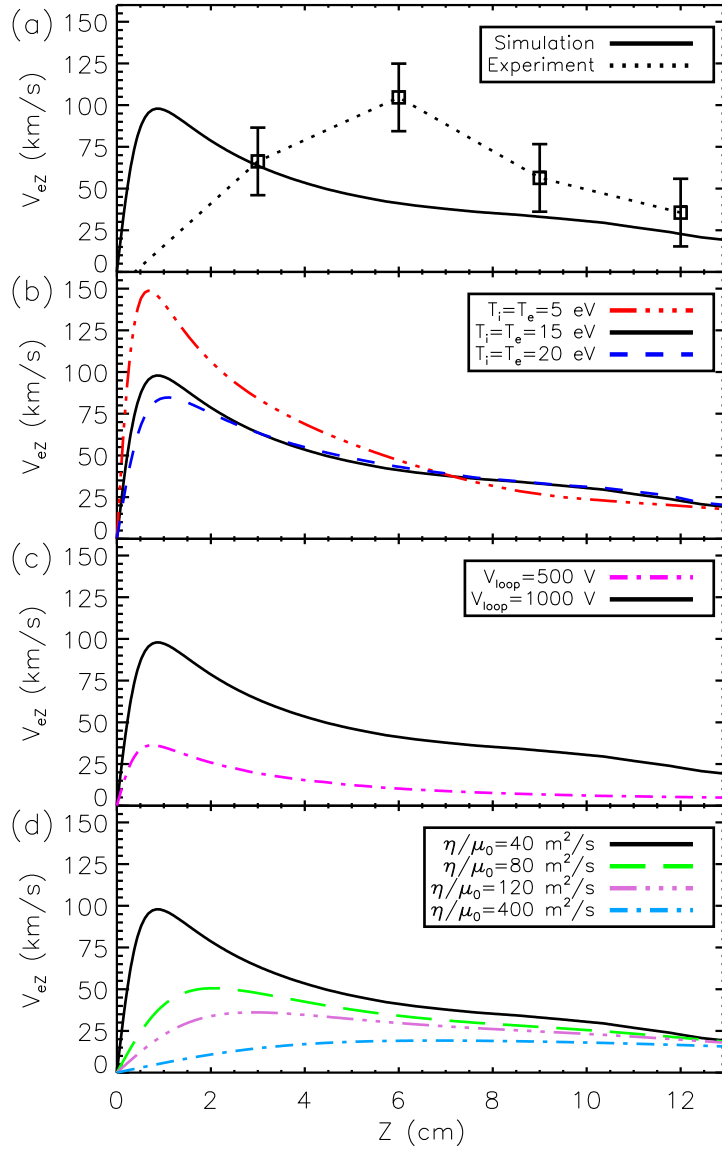


Fig. 2.13.—: The outflow component of electron velocity during a linear geometry simulation of two-fluid pull reconnection. In (a), a comparison is made to an equivalent experimental result (data courtesy of Y. Ren). In (b), (c), and (d), comparisons of electron outflow profiles are made for different initial temperatures, driving voltage strengths, and resistivities. Unless noted, $\eta/\mu_0 = 40 \text{ m}^2 \text{ s}^{-1}$.

To gain insight into what sets the electron outflow profile in these simulations, scaling studies of initial temperature, driving voltage, and resistivity are performed. Figure 2.13(b) shows that while the position of the peak electron outflow is not greatly affected by initial temperature, higher initial temperatures correspond to weaker peak outflows. This highlights the role downstream pressure plays in determining the nature of the electron outflow. Figure 2.13(c) shows that stronger driving voltages lead to much stronger electron outflows with peaks slightly further from $Z = 0$. Figure 2.13(d) shows that significantly larger global resistivity leads to slower outflows with peaks located significantly further from the X-point. Because these simulations are unable to achieve an electron outflow profile comparable to experiment within the appropriate range of physical parameters, it must be concluded that physics outside the two-fluid model with uniform resistivity is necessary to explain this discrepancy with experiment. The short electron diffusion region predicted by the standard picture of Hall reconnection (Mandt et al. 1994; Biskamp et al. 1997) and seen in the simulations reported in this chapter is not observed in experiment. It is plausible that the kinetic physics leading to the elongated electron diffusion regions seen in Daughton et al. (2006), Fujimoto (2006), Shay et al. (2007), Karimabadi et al. (2007), Phan et al. (2007), and Dorfman et al. (2008) may contribute to the broadness of the electron outflow profile in experiment.

2.5.3.4 Electron Outflow Opening Angle

Also of interest is the opening angle of the electron outflow. In Figure 2.10(c), the electron outflow opening half-angle (e.g., the angle between the separatrix and outflow direction) is measured to be $\sim 10^\circ$ for two-fluid pull reconnection. A decrease in the initial density by a factor of two results in a much wider cone, typically with a half-angle of

$\sim 20^\circ$. Lowering the driving voltage also has the effect of increasing the half-angle to $\sim 20^\circ$. Resistivity has the effect of blurring the boundary between the electron inflow and the electron outflow. A change in the ion species in simulation does not result in a significant change in outflow angle. A recent work by Singh (2007) argues that in the whistler regime, the electron outflow opening half-angle matches the linear group velocity cone angle of 19.5° . Close to the reconnection region, these simulations show no electron outflow opening angles $\gtrsim 20^\circ$. However, experimental results in Figure 4.19 of Ren (2007) show that the half-angle between the separatrices ranges from 15° to 30° , depending on the ion species. For deuterium, the range is from 15° to 20° .

2.5.3.5 Quadrupole Shape

The quadrupole shapes are directly compared between experiment and simulation in Figure 2.9. Neither of these results are symmetric to a 180° rotation about the center of reconnection [see also Figure 2.10(a)]. Because linear geometry simulations show a symmetric quadrupole field with the X-point at the midpoint between the two flux cores, it is apparent that asymmetry in simulation is due to cylindrical geometry effects. While the quadrupole lobes appear thinner and more clearly separated in simulation than in experiment, the peak magnitude of the outboard quadrupole is located near $Z = 8$ cm in both the simulation and experimental results. In contrast, a clear local maximum for the inboard quadrupole lobes is not within the region plotted in both Figure 2.9(a) and Figure 2.9(b). In simulation, the inboard quadrupole lobes are strongest near the flux core surfaces. However, that azimuthal fields induced during the plasma formation process may also influence the experimental results.

During pull reconnection, the quadrupole field is strongly affected by the flux cores.

While in push reconnection the quadrupole is everywhere concave towards the flux cores, it turns concave away from the flux cores near the X-point in pull reconnection [see Figures 2.10(a) & 2.11]. This indicates that, especially for pull reconnection, the flux core positions noticeably affect the spatial distribution of the quadrupole field. Other important features are that (1) the pull quadrupole lobes have greater breadth than the push quadrupole lobes, (2) the quadrupole is located along the separatrix for both push and pull reconnection, and (3) the quadrupole peak strength is greater during pull reconnection than push reconnection despite the push reconnection rate being greater than the pull reconnection rate.

2.5.4 Convergence

In Figure 2.14, I present a convergence study for the simulations of MRX presented in this chapter. In particular, I repeat the four simulations plotted in Figure 2.12 using different numbers of bicubic finite elements and compare parameters extracted from each simulation at $t = 10.5 \mu\text{s}$ (3000 timesteps into the simulation). The weight functions used for the weighted averaging technique (see Section 2.3 and Appendix A) are varied only locally near the flux cores to avoid the use of highly distorted elements but are unchanged in the reconnection region. The parameters chosen are (a) the peak magnitude of the resistive electric field, (b) the maximum pressure, and, for two-fluid simulations, (c) the peak magnitude of the out-of-plane quadrupole magnetic field. These parameters are chosen because their importance as quantities during the reconnection process. Because of the small amount of variation for each of these simulation setups, I conclude that the simulations presented in this chapter are well converged.

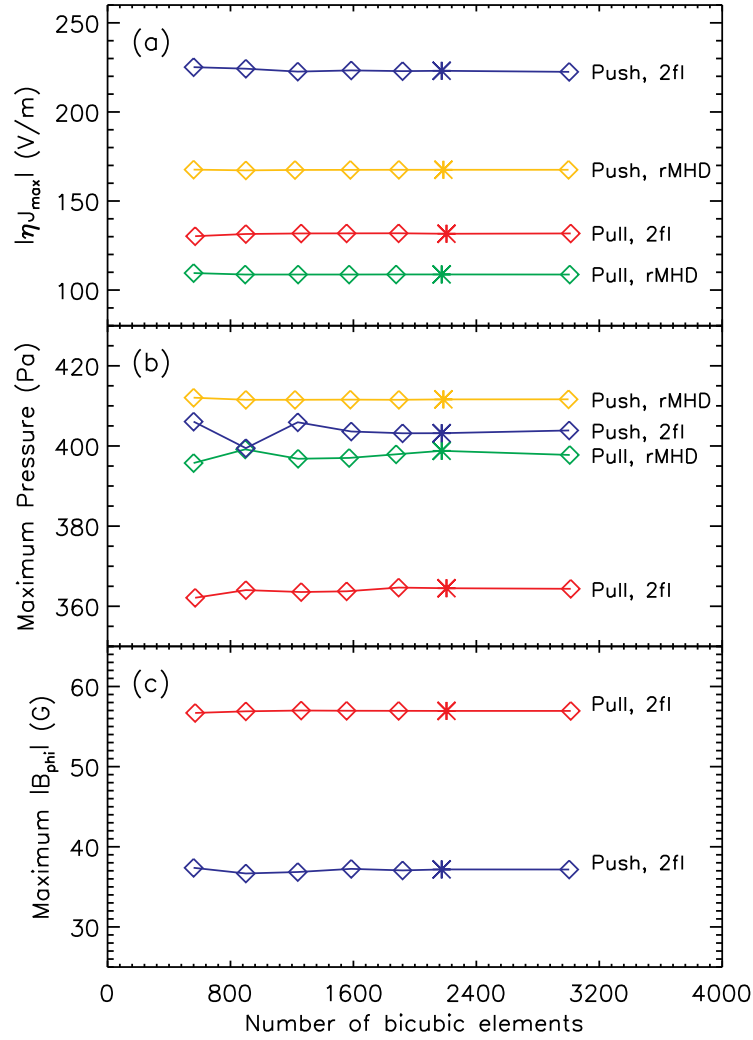


Fig. 2.14.—: Results from a convergence study in which the simulations presented in Figure 2.12 are repeated with different numbers of finite elements. Shown for each of these simulations are (a) the peak magnitude of the resistive electric field, (b) the maximum pressure, and, for two-fluid simulations, (c) the peak magnitude of the out-of-plane quadrupole magnetic field. Asterisks correspond to the simulations presented in Figure 2.12.

2.6 Co- and Counter-Helicity Two-Fluid Results

In the simulations reported in Sections 2.4 and 2.5, the electric field applied on the flux core surfaces is purely azimuthal, and hence the flux cores do not directly induce azimuthal field. The out-of-plane magnetic fields that are present in two-fluid simulations are generated through in-plane electric fields in the plasma. It is important to note again that for null-helicity resistive MHD reconnection, there is no in-plane electric field and hence no out-of-plane magnetic field is able to develop. In this section we consider the effects of inducing a azimuthal field directly from the flux cores. In co-helicity merging, the induced azimuthal field is in the same direction from both flux cores. In counter-helicity reconnection, the induced azimuthal fields are opposite in direction. This section will show that asymmetry due to the Hall effect leads to asymmetric outflow that then feeds back on the reconnection layer through pressure gradients.

2.6.1 Two-Fluid Co-Helicity Push Reconnection

Figure 2.15 shows the results of two-fluid co-helicity (guide field) push reconnection in a linear geometry simulation. Figure 2.15(a) shows that the current sheet is tilted with respect to $Z = 0$. Figures 2.15(b) and 2.15(c) show that the out-of-plane magnetic field pattern and plasma pressure distributions are also tilted. These features are not present during resistive MHD simulations. This tilting of the current sheet structure has not been unambiguously identified in MRX, but has been observed in experiments at the CS-3D device during guide field experiments with heavy ions (Frank et al. 2006), as well as in previous simulations (e.g., Hesse et al. 1999; Pritchett & Coroniti 2004).

To gain insight into the origin of this tilting effect, consider that during two-fluid antiparallel reconnection, there are strong in-plane currents associated with the electron

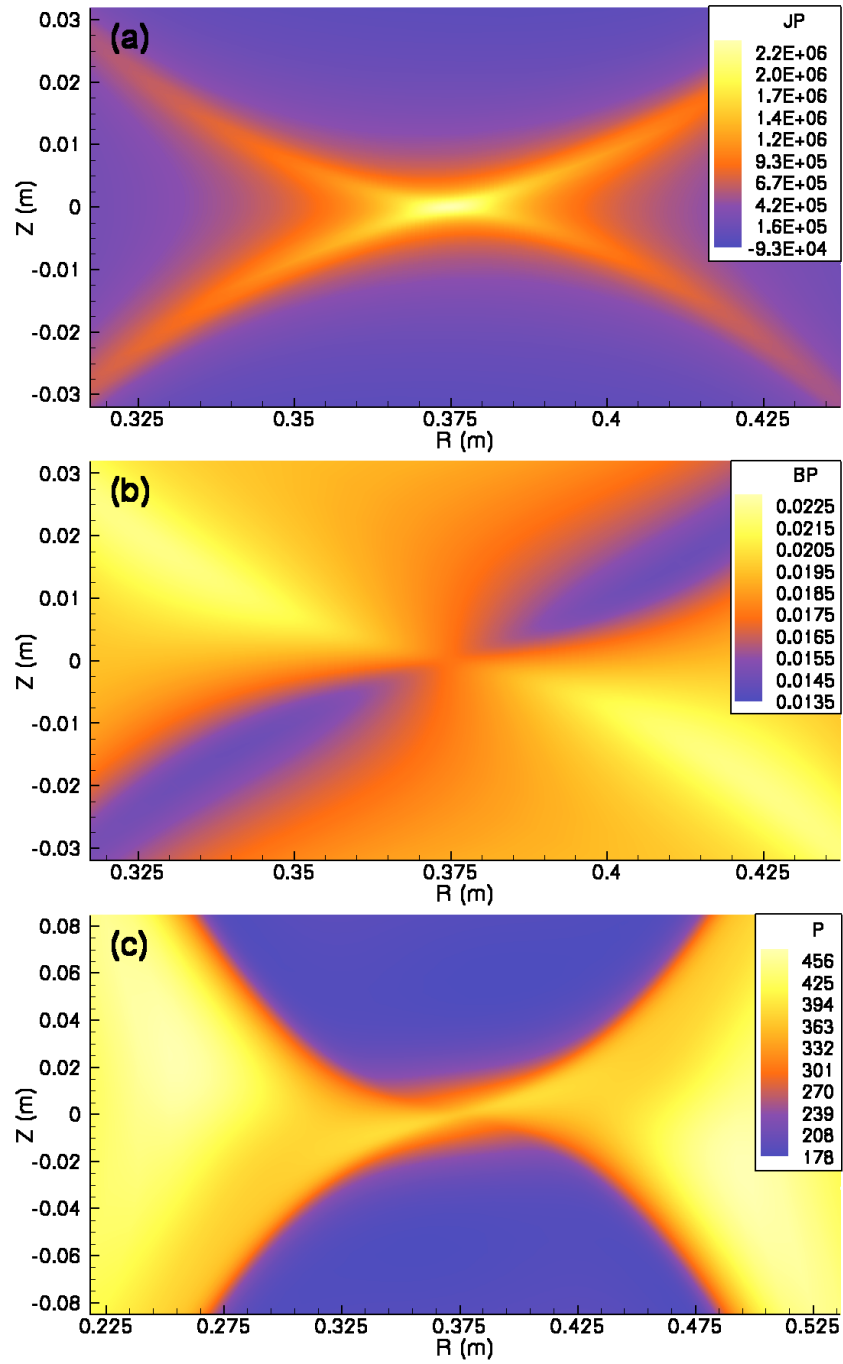


Fig. 2.15.—: Out-of-plane current density (a), out-of-plane magnetic field (b), and plasma pressure (c) during a linear geometry simulation of two-fluid co-helicity (guide field) push reconnection.

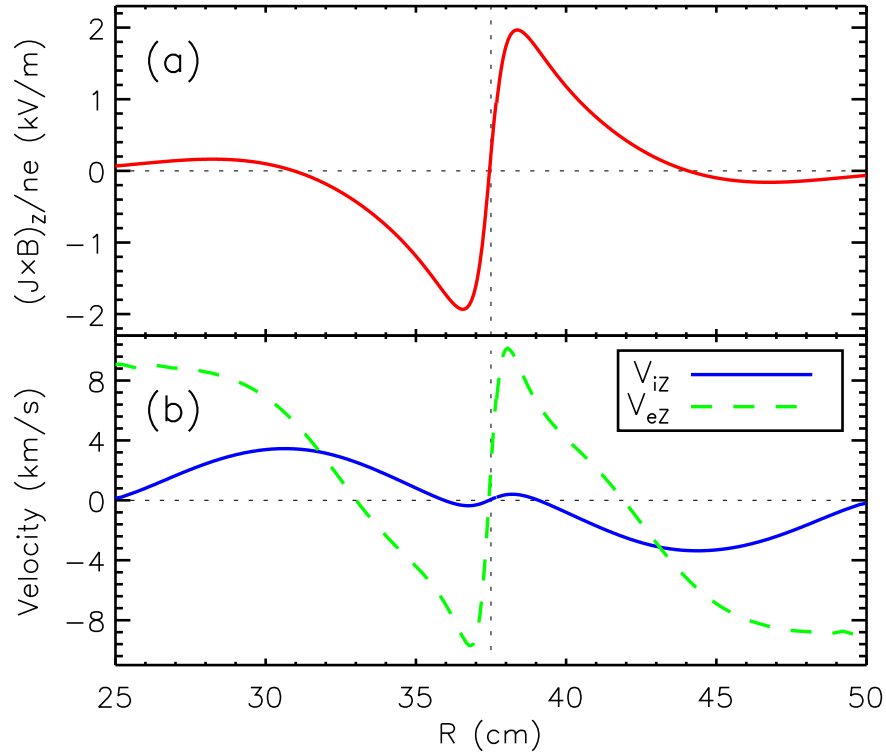


Fig. 2.16.—: The vertical component of the Hall electric field (a), and the vertical components of the ion and electron velocities V_{iZ} and V_{eZ} (b) along $Z = 0$ during a linear geometry simulation of two-fluid co-helicity push reconnection.

outflow. Artificially imposing a guide field leads to a vertical (Z) component of the Hall electric field in the outflow region, seen for the simulation in Figure 2.16(a). This vertical Hall electric field represents a Lorentz force that acts in opposite directions on the ions and the electrons on each side of the current sheet, resulting in different signs of the Z component of velocity for each species along $Z = 0$ as seen in Figure 2.16(b). The magnetic field is carried in the direction of electron motion on scales $\lesssim c/\omega_{pi}$, resulting in a tilted current sheet.

Associated with the tilting of the current sheet is tilting of the pressure contours, as shown in Figure 2.15(c). This can be understood in terms of the vertical component of the ion and electron velocity along $Z = 0$, shown in Figure 2.16(b). To the immediate left (right) of the X-point, the ions exhibit a small downward (upward) component of velocity that is directly due to the tilted nature of the current sheet. At distances further out, ions show a positive Z component of velocity for $R < 37.5$ cm and a negative Z component of velocity for $R > 37.5$ cm. This velocity profile is a direct result of the mechanism discussed above, and leads to the distorted pressure contours.

2.6.2 Two-Fluid Counter-Helicity Push Reconnection

Recent experimental results in MRX show that the X-point exhibits a radial shift in position associated with the Hall effect during counter-helicity push reconnection (Inomoto et al. 2006). Differences in the reconnection rate and the downstream pressure are also observed for reversed azimuthal field directions. In these results, the surface containing reconnecting field lines is rotated, and the electron velocity associated with the reconnecting current has a radial component. The magnetic field configuration is carried by the electrons in the radial direction, resulting in a shift in position of the X-point. As pointed out by Inomoto et al. (2006), this effect is related to the formation of the quadrupole field during null-helicity merging. However, a strict comparison with a tilted quadrupole does not take into account the axisymmetric nature of the configuration. For example, in the extreme case of the opposing azimuthal fields being much stronger than the opposing poloidal fields, quadrupole formation is disallowed because it would require a poloidal field that changes direction in the toroidal angle.

The shift in position of the X-point does not require cylindrical geometry, and so to

simplify the analysis of this symmetry breaking mechanism, linear geometry simulations of counter-helicity push reconnection are discussed first. Resistive MHD simulations of counter-helicity push reconnection do not show the development of this asymmetry. When two-fluid physics is added to the time advance during the middle of a simulation, the asymmetry develops quickly as the magnetic field becomes tied to the electron fluid. As the radial shift develops, the asymmetric outflow also becomes noticeable. This ties the asymmetry to the Hall effect.

Figure 2.17 shows current density contours (a) and pressure contours (b) for a simulation with two-fluid physics included from the beginning. The current sheet is shifted to the left of the flux cores, which are located at $R = 0.375$ m. There is a corresponding buildup of pressure on the side from which the current sheet was shifted. A quadrupole field is still present when viewed in a rotated reference frame (not shown). The electron outflow is predominantly towards the left and the ion outflow is predominantly towards the right. The pressure buildup on the right corresponds to the ion (bulk plasma) outflow, and the shift of the current sheet to the left corresponds to the electron outflow. As can be seen in Figure 2.18, the radial ion flow stagnation point, the radial electron flow stagnation point, the magnetic field null, and the peak out-of-plane current density are separated from each other.

Several effects facilitate the asymmetric flow pattern and pressure distribution.

1. High magnetic pressure closer to the X-point on the left slows ion outflow aimed in that direction (Inomoto et al. 2006).
2. Higher magnetic tension on the right increases outflow directed to the right.
3. As the plasma attempts to settle into equilibrium, the result is a diamagnetic ion flow

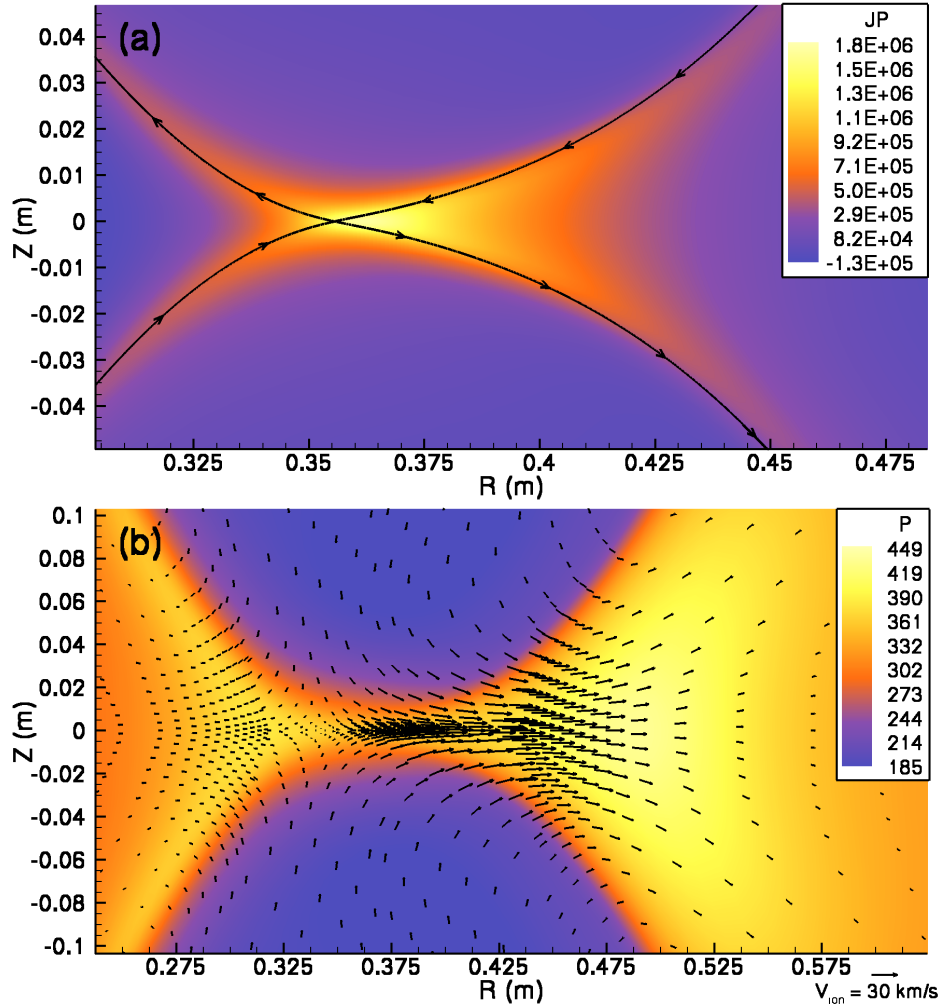


Fig. 2.17.—: Out-of-plane current density along with a magnetic field stream-trace of the separatrix (a), and plasma pressure with ion velocity vectors (b) during a simulation of two-fluid counter-helicity push reconnection performed in linear geometry to remove cylindrical geometry effects. The out-of-plane magnetic field induced by the flux cores is out of the page for $Z > 0$ and into the page for $Z < 0$. Note that in (a) the X-point is shifted to the left of $R = 0.375$ (the position of the flux core centers) and that in (b) there is strong ion outflow towards the right that leads to the asymmetric pressure buildup.

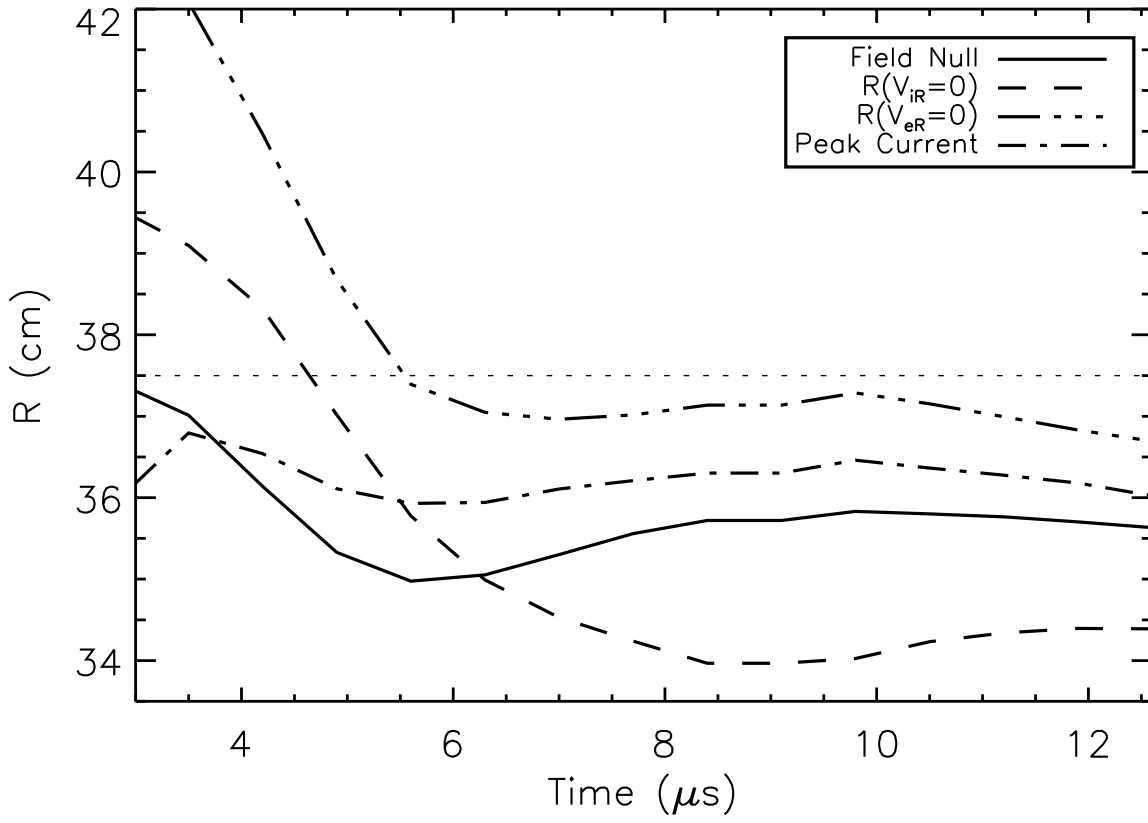


Fig. 2.18.—: The positions of the magnetic field null, the radial ion flow stagnation point, the radial electron flow stagnation point, and the peak current density as a function of time during a simulation of counter-helicity merging in linear geometry.

to the right above and below the current sheet.

All of these effects are present in this simulation and enhance asymmetric outflow in the same direction.

The asymmetric outflow is best understood by comparing the plasma pressure, magnetic tension, and magnetic pressure terms in the momentum equation along $Z = 0$, as shown in Figure 2.19. On the far left, magnetic pressure dominates and limits the ability of plasma to escape the reconnection region. This facilitates the development of a small region of enhanced plasma pressure that acts on the outflow to the left to cancel forces resulting from magnetic tension close to the X-point. On the right hand side, magnetic tension is stronger because the current sheet is pulled to the left. Magnetic and plasma pressure are largely flat for approximately 5 cm, and magnetic tension overwhelms all other forces in the region to the right of the current sheet.

The above analysis investigates the flow along $Z = 0$. However, diamagnetic effects are apparent in the flow patterns above and below the current sheet. In its general form, the diamagnetic drift is given by

$$\mathbf{V}_{*j} = -\frac{\nabla p_j \times \mathbf{B}}{q_j n B^2}. \quad (2.13)$$

The diamagnetic drift has been studied previously in the context of reconnection as a suppression mechanism when there is a density gradient in the inflow direction (Swisdak et al. 2003). Immediately above and below the current sheet, radial derivatives are small, so

$$\mathbf{V}_* \approx -\frac{1}{2qnB^2} \left(\hat{R} B_\phi \frac{\partial p_{tot}}{\partial Z} - \hat{\phi} B_R \frac{\partial p_{tot}}{\partial Z} \right), \quad (2.14)$$

where for this single-temperature model, the subscript j indicating species has been dropped. The pressure in the current sheet is a factor of 1.5-2 higher than the pressure a few centimeters above and below. This jump in pressure occurs within a length scale of 1-2 cm,

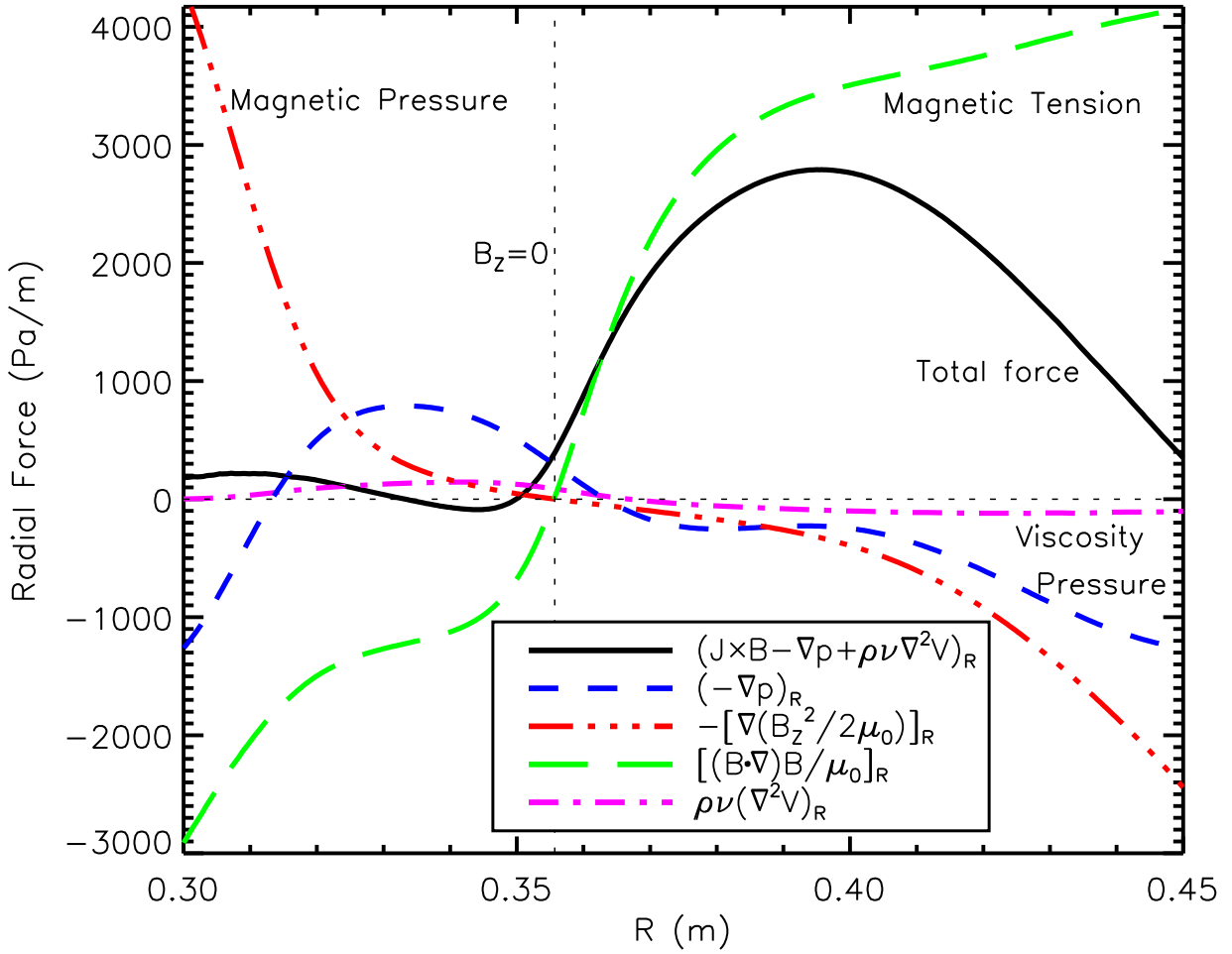


Fig. 2.19.—: Terms in the R -component of the momentum equation along $Z = 0$ m are compared for a simulation of two-fluid counter-helicity push reconnection using linear geometry. The X-point position is shifted to the left of $R = 0.375$ m due to the Hall effect.

corresponding to an extremely large localized pressure gradient. In this region, a typical value of the vertical pressure gradient is $\partial p/\partial Z \approx 7 - 10 \times 10^3$ Pa/m, significantly larger than most other pressure gradients found in the system. For the values found at $(R, Z) = (0.36, -0.01)$, the ions have a rightward diamagnetic drift of order 30 km/s, and the electrons have a leftward diamagnetic drift with the same magnitude. The drift for each species is in the same direction both above and below the current sheet. When the reconnection plane is not in the poloidal plane, pressure gradients are not in the same plane as the reconnecting magnetic fields and these additional diamagnetic drift effects must be considered.

Along $Z = 0$, the diamagnetic drift in the radial direction is small. The pressure gradient opposes the ion outflow but is shallow compared to $(\mathbf{J} \times \mathbf{B})_R$. This latter term plays the dominant role in accelerating the bulk plasma outflow in this region where the vertical pressure gradient goes to zero. It should be noted that in simulations with $\beta = 0$, the X-point is still shifted and there is asymmetric outflow even without the diamagnetic drift. However, above and below the current sheet the diamagnetic drift significantly alters the flow pattern.

This discussion of asymmetry due to the Hall effect has not invoked cylindrical geometry effects. A conclusion of Section 2.4, however, is that the lesser volume available on the inboard side of the current sheet leads to a fast buildup of pressure that pushes the X-point radially outward. Hence, during two-fluid counter-helicity push reconnection in cylindrical geometry, symmetry is broken due to both cylindrical geometry effects and the Hall effect. Depending on the orientation of the azimuthal field, these symmetry breaking mechanisms can either work together or oppositely.

Figure 2.20 shows the effects of the combination of these two symmetry breaking

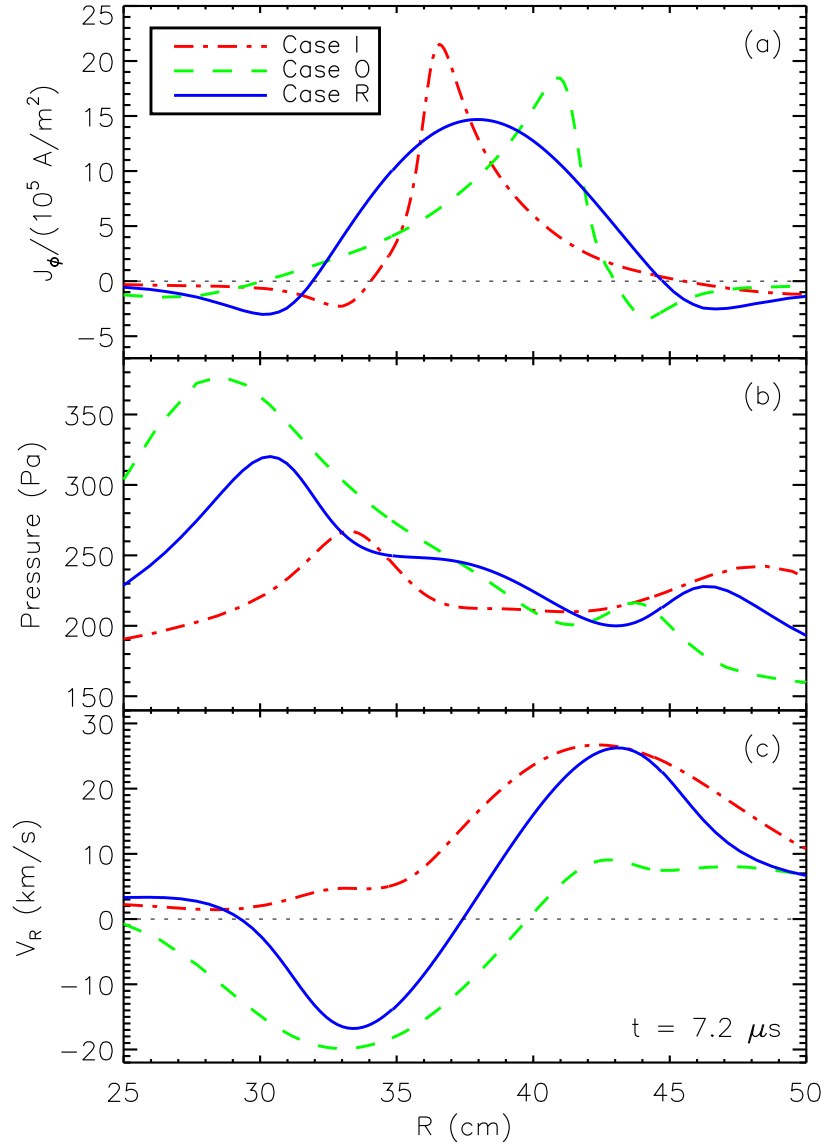


Fig. 2.20.—: Azimuthal current density (a), plasma pressure (b), and radial velocity (c) as functions of radius during counter-helicity push reconnection using cylindrical geometry. Symmetry breaking is due to both cylindrical geometry and the Hall effect. Cases I and O refer to two-fluid simulations of counter-helicity push reconnection showing an inward and outward radial shift, respectively. Case R refers to the resistive MHD equivalent of case I.

mechanisms on the azimuthal current density, the plasma pressure, and the radial velocity along $Z = 0$. Using the nomenclature from Inomoto et al. (2006) for two-fluid simulations, case O shows a radially outward shift of the X-point, while case I shows an inward shift of the X-point. In the poloidal slice shown in Figure 2.1, case O (case I) has azimuthal field in the out-of-page (in-page) direction for $Z > 0$ and in the in-page (out-of-page) direction for $Z < 0$. Case R is a resistive MHD simulation where the sign of B_ϕ does not affect the result. The initial conditions, plasma parameters, and driving voltage strengths are identical for all three cases.

The Hall symmetry breaking is most apparent in Figure 2.20(a). Cases I and O display the expected behavior for out-of-plane current density, clearly showing an inward shift of the X-point for case I and an outward shift of the X-point for case O, both relative to case R. Figures 2.20(b) and 2.20(c) show that the pressure distribution and the radial velocity profile are strongly affected by both cylindrical geometry effects and Hall symmetry breaking. In case O, both the Hall effect and cylindrical geometry effects are acting to increase the outflow in the inboard direction. As a result, the pressure profile across the reconnection region decreases almost monotonically and the radially inward outflow is much stronger than the radially outward outflow. In case I, the Hall effect is trying to push the outflow in the outboard direction while cylindrical geometry effects are trying to push the outflow in the inboard direction. The pressure profile is much flatter than case O, but the outflow is predominantly in the radially outward direction.

References

- Birn, J., Drake, J. F., Shay, M. A., Rogers, B. N., Denton, R. E., Hesse, M., Kuznetsova, M., Ma, Z. W., Bhattacharjee, A., Otto, A., & Pritchett, P. 2001, *J. Geophys. Res.*,

106, 3715

Biskamp, D., Schwarz, E., & Drake, J. F. 1997, *Phys. Plasmas*, 4, 1002

Borovsky, J. E., & Hesse, M. 2007, *Phys. Plasmas*, 14, 102309

Carter, T. A., Ji, H., Trintchouk, F., Yamada, M., & Kulsrud, R. M. 2002a, *Phys. Rev. Lett.*, 88, 015001

Carter T. A., Yamada, M., Ji, H., Kulsrud, R. M., & Trintchouk, F. 2002b, *Phys. Plasmas*, 9, 3272

Cassak, P. A., & Shay, M. 2007, *Phys. Plasmas*, 14, 102114

Cothran, C. D., Landreman, M., Brown, M. R., & Matthaeus, W. H. 2005, *Geophys. Res. Lett.*, 32, 3105

Daughton, W., Scudder, J., & Karimabadi, H. 2006, *Phys. Plasmas*, 13, 072101

Dorfman, S., Ji, H., Yamada, M., Ren, Y., Gerhardt, S. P., Kulsrud, R. M., McGeehan, B., & Wang, Y. 2006, *AIP Conf. Proc.*, 871, 306

Dorfman, S., Daughton, W., Roytershteyn, V., Ji, H., Ren, Y., & Yamada, M. 2008, *Phys. Plasmas*, 15, 102107

Frank, A. G., Bogdanov, S. Y., Dreiden, G. V., Markov, V. S., & Ostrovskaya, G. V. 2006, *Phys. Lett. A*, 348, 318

Fujimoto, K. 2006, *Phys. Plasmas*, 13, 072904

Gerhardt, S. P., Belova, E., Inomoto, M., Yamada, M., Ji, H., Ren, Y., & Kuritsyn, A. 2006, *Phys. Plasmas*, 13, 2508

Gerhardt, S. P., Belova, E. V., Yamada, M., Ji, H., Inomoto, M., Ren, Y., & McGeehan, B. 2007, *Phys. Rev. Lett.*, 99, 245003

- Hesse, M., Schindler, K., Birn, J., & Kuznetsova, M. 1999, *Phys. Plasmas*, 6, 1781
- Hsu, S. C., Fiksel, G., Carter, T. A., Ji, H., Kulsrud, R. M., & Yamada, M. 2000, *Phys. Rev. Lett.*, 84, 3859
- Hsu, S. C., Carter, T. A., Fiksel, G., Ji, H., Kulsrud, R. M., & Trintchouk, F. 2001, *Phys. Plasmas*, 8, 1916
- Inomoto, M., Gerhardt, S. P., Yamada, M., Ji, H., Belova, E., Kuritsyn, A., & Ren, Y. 2006, *Phys. Rev. Lett.*, 97, 135002
- Ji, H., Yamada, M., Hsu, S., & Kulsrud, R. 1998, *Phys. Rev. Lett.*, 80, 3256
- Ji, H., Yamada, M., Hsu, S., Kulsrud, R., Carter, T., & Zaharia, S. 1999, *Phys. Plasmas*, 6, 1743
- Ji, H., Terry, S., Yamada, M., Kulsrud, R., Kuritsyn, A., & Ren, Y. 2004a, *Phys. Rev. Lett.*, 92, 115001
- Ji, H., Yamada, M., Terry, S., Kulsrud, R., Ren, Y., & Kuritsyn, A. 2004b, *AIP Conf. Proc.*, 703, 437
- Karimabadi, H., Daughton, W., & Scudder, J. 2007, *Geophys. Res. Lett.*, 34, 13104
- Kondoh, K., Ugai, M., & Shimizu, T. 2004, *Adv. Space Res.*, 33, 794
- Kuritsyn, A., Ph.D. thesis, Princeton University, 2005
- Kuritsyn, A., Yamada, M., Gerhardt, S., Ji, H., Kulsrud, R., & Ren, Y. 2006, *Phys. Plasmas*, 13, 5703
- Kuritsyn, A., Ji, H., Gerhardt, S., Ren, Y., & Yamada, M. 2007, *Geophys. Res. Lett.*, 34, L16106

- Linton, M. G. 2006, *J. Geophys. Res.*, 111, 12
- Lukin, V. S., Qin, G., Matthaeus, W. M., & Brown, M. R. 2001, *Phys. Plasmas*, 8, 1600
- Lukin, V. S., & Jardin, S. C. 2003, *Phys. Plasmas*, 10, 3131
- Mandt, M. E., Denton, R. E., & Drake, J. F. 1994, *Geophys. Res. Lett.*, 21, 73
- Matthaeus, W. M., Cothran, C. D., Landreman, M., & Brown, M. R. 2005, *Geophys. Res. Lett.*, 32, 23104
- Mozer, F. S., Bale, S. D., & Phan, T. D. 2002, *Phys. Rev. Lett.*, 89, 015002
- Phan, T. D., Drake, J. F., Shay, M. A., Mozer, F. S., & Eastwood, J. P. 2007, *Phys. Rev. Lett.*, 99, 255002
- Pritchett, P. L. & Coroniti, F. V. 2004, *J. Geophys. Res.*, 109, 1220
- Ren, Y., Yamada, M., Gerhardt, S., Ji, H., Kulsrud, R., & Kuritsyn, A. 2005, *Phys. Rev. Lett.*, 95, 055003
- Ren, Y., Ph.D. thesis, Princeton University, 2007
- Ren, Y., Yamada, M., Ji, H., Dorfman, S., Gerhardt, S., & Kulsrud, R. 2008, *Phys. Plasmas*, 15, 082113
- Schnack, D., Lottati, I., Mikić, Z., & Satyanarayana, P. 1998, *J. Comput. Phys.*, 140, 71
- Schnack, D. D., Barnes, D. C., Brennan, D. P., Hegna, C. C., Held, E., Kim, C. C., Kruger, S. E., Pankin, A. Y., & Sovinec, C. R. 2006, *Phys. Plasmas*, 13, 058103
- Shay, M. A., Drake, J. F., & Swisdak, M. 2007, *Phys. Rev. Lett.*, 99, 155002
- Singh, N. 2007, *J. Geophys. Res.*, 112, 7209

- Sovinec, C. R., Glasser, A. H., Gianakon, T. A., Barnes, D. C., Nebel, R. A., Kruger, S. E., Schnack, D. D., Plimpton, S. J., Tarditi, A., & Chu, M. S. 2004, *J. Comput. Phys.*, 195, 355
- Sovinec, C. R., Schnack, D. D., Pankin, A. Y., Drennan, D. P., Tian, H., Barnes, D. C., Kruger, S. E., Held, E. D., Kim, C. C., Li, X. S., Kaushik, D. K., & Jardin, S. C., 2005 *J. Phys. Conf. Ser.*, 16, 25
- Sovinec, C. R., Schnack, D. D., Barnes, D. C., & Brennan, D. P. 2006, *Bull. Am. Phys. Soc.*, 51, 166
- Stenzel, R. L. & Gekelman, W. 1981, *J. Geophys. Res.*, 86, 649
- Swisdak, M., Rogers, B. N., Drake, J. F., & Shay, M. A. 2003, *J. Geophys. Res.*, 108, 23
- Trintchouk, F., Yamada, M., Ji, H., Kulsrud, R. M., & Carter, T. A. 2003, *Phys. Plasmas*, 10, 319
- Ugai, M. 2000, *Phys. Plasmas*, 7, 867
- Watanabe, T.-H., Hayashi, T., Sato, T., Yamada, M., & Ji, H. 1999, *Phys. Plasmas*, 6, 1253
- Yamada, M., Ji, H., Hsu, S., Carter, T., Kulsrud, R., Bretz, N., Jobes, F., Ono, Y., & Perkins, F. 1997a, *Phys. Plasmas*, 4, 1936
- Yamada, M., Ji, H., Hsu, S., Carter, T., Kulsrud, R., Ono, Y., & Perkins, F. 1997b, *Phys. Rev. Lett.*, 78, 3117
- Yamada, M., Ji, H., Hsu, S., Kulsrud, R., Carter, T., & Zaharia, S. 2000, *Phys. Plasmas*, 7, 1781
- Yamada, M., Ren, Y., Ji, H., Breslau, J., Gerhardt, S., Kulsrud, R., & Kuritsyn, A. 2006, *Phys. Plasmas*, 13, 2119

Chapter 3

Magnetic Reconnection with Asymmetry in the Outflow Direction

This chapter has been adapted from Murphy, N. A., Sovinec, C. R., & Cassak, P. A. 2009, J. Geophys. Res., to be submitted.

3.1 Introduction

While most two-dimensional models of magnetic reconnection assume that the process is symmetric to a 180° rotation about the X-point, there are many situations in nature and in the laboratory where this assumption is invalid. In recent years, a number of papers have addressed magnetic reconnection with asymmetry in the inflow direction (e.g., La Belle-Hamer et al. 1995; Karimabadi et al. 1999; Nakamura & Scholer 2000; Swisdak et al. 2003; Borovsky & Hesse 2007; Cassak & Shay 2007, 2008, 2009; Birn et al. 2008; Mozer et al. 2008; Pritchett 2008; Borovsky et al. 2008; Mozer & Pritchett 2009; Eriksson et al. 2009). In particular, Cassak and Shay (2007) generalize the Sweet-Parker model (Parker 1957; Sweet 1958) to account for reconnection between plasmas with different upstream densities and magnetic field strengths. They find that the reconnection rate is governed by a hybrid Alfvén speed that takes into account the densities and magnetic field strengths for the two upstream regions. The positions of the magnetic field null and flow stagnation point are displaced from each other, with the field null position being set by the balance of energy flux, and the stagnation point position being set by the balance of mass flux. This chapter extends the Sweet-Parker model to describe aspects of magnetic reconnection with asymmetry in the outflow direction.

The best known scenario for magnetic reconnection with asymmetry in the outflow direction is the Earth’s magnetotail. In this case, asymmetry is particularly important because it helps determine the amount of energy transported in the Earthward and tailward directions as a result of reconnection. At distances of $\sim 5\text{--}15R_E$, there is a considerable pressure gradient as the plasma pressure decreases approximately monotonically with dis-

tance from Earth (Lui et al. 1994; Shiokawa et al. 1997) Earthward-directed reconnection outflow must work against strong gradients in both plasma pressure and magnetic pressure. Reconnection with asymmetry in the outflow direction is often seen in simulations of Earth’s magnetotail (e.g., Birn et al. 1996; Hesse & Schindler 2001; Kuznetsova et al. 2007; Laitinen et al. 2005; Laitinen 2007; Birn & Hesse 2009), although the degree of asymmetry depends on the proximity of the reconnection layer to Earth and how reconnection is driven. The largest discrepancy between earthward and tailward outflow velocities in these simulations is seen by Laitinen et al. (2005) and Laitinen (2007), where the inflow already has a large component of velocity in the outflow direction; consequently, there is a large separation between the X-line and the flow reversal line in these simulations.

Satellite observations of magnetospheric reconnection with asymmetry in the outflow direction require multiple satellites crossing the earthward and tailward sides of the diffusion region at approximately the same time. Such observations are rare. An interesting example occurred during a crossing of the diffusion region by the *Cluster* satellites on 11 October 2001. *Cluster* was in the region between the outflow jets from 03:30–03:36 UT, but passed the X-line at 03:31 UT (well before *Cluster* was halfway through the current sheet). One possible explanation of this is that the X-line was near the tailward end of the diffusion region. However, other explanations (e.g., time-dependent behavior or undetected additional X-lines) cannot be ruled out with the available data (Laitinen et al. 2007).

In solar physics, reconnection during coronal mass ejections (CMEs), solar flares, and flux cancellation events will be asymmetric in the outflow direction when one outflow jet is directed downward and the other outflow jet is directed away from the Sun (e.g., Kopp & Pneuman 1976; Martin et al. 1985; Shibata et al. 1995; Litvinenko 1999; Lin & Forbes 2000). Observations of bi-directional jets during solar flares (e.g., Innes et al. 1997; Wang

et al. 2007) show that the redshifted jet is often slower than the blueshifted jet because the redshifted jet must propagate into a higher density medium, despite the effects of gravity. In these events, gravity does not merely act as a body force throughout the plasma; rather, gravity's most important effect is the establishment of a stratified medium. Simulations of reconnection in such a medium show that the redshifted jet can be up to an order of magnitude slower than the blueshifted jet (Roussev et al. 2001), and that reconnection in such an atmosphere displays a more complicated velocity structure than symmetric two-dimensional reconnection (Galsgaard & Roussev 2002). Recent observations and simulations also suggest a correlation between the reconnection rate and the velocity of the ejected plasmoid (Qiu & Yurchyshyn 2005; Shimizu et al. 2008; Nishida et al. 2009). Gravity itself can be an important consideration if the work done by electromagnetic forces is comparable to or less than the work done against gravity (Reeves et al. 2006). Line-tying effects (e.g., Huang & Zweibel 2009) are also likely to be important during reconnection in the solar atmosphere.

During turbulent reconnection (e.g., Lazarian & Vishniac 1999) and reconnection occurring during a turbulent cascade (e.g., Servidio et al. 2009), there will in general be many reconnection sites throughout the volume of interest. Reconnection occurring at each of these sites will in general be asymmetric in the inflow and outflow directions, as well as the out-of-plane direction. Reconnection processes involving multiple competing reconnection sites or multiple magnetic islands (e.g., Lee & Fu 1986; Drake et al. 2006; Chen et al. 2008, 2009) will also likely involve asymmetry in the outflow direction, especially if the X-lines are not evenly spaced.

The winds of strongly magnetized hot stars (e.g., the Bp star σ Ori E) can be channeled along a predominantly dipolar field to form an equatorial circumstellar disk or buildup of

material (Nakajima 1985; Cassinelli et al. 2002; Townsend & Owocki 2005). While the dipole field is in general dominant close to the star, recent axisymmetric simulations show that the continual funneling of material can eventually lead to centrifugal breakout events associated with magnetic reconnection (ud-Doula et al. 2006; 2008). In this case, the reconnection outflow is aligned with the radial direction, with one exhaust path directed towards the disk and the star, and the other leading to the interstellar medium. Such reconnection events could be the source of the X-ray flares observed on σ Ori E by ROSAT (Groote & Schmitt 2004). These considerations are also important for centrifugal instabilities and plasma release in the Jovian magnetosphere (e.g., Kivelson & Southwood, 2005).

In the laboratory, reconnection with asymmetry in the outflow direction occurs during the merging of spheromaks or other toroidal plasma configurations where the reconnection outflow is aligned with the radial direction. Relevant experiments include the Swarthmore Spheromak Experiment (SSX) (Cothran et al. 2003) the Magnetic Reconnection Experiment (MRX) (Yamada et al. 1997), and TS-3/4 at the University of Tokyo (Ono et al. 1993). Recent spheromak merging experiments at MRX have shown that asymmetry in the outflow direction develops as a result of the Hall effect (Inomoto et al. 2006) In these experiments at MRX, the reconnecting magnetic field lines do not lie in the poloidal plane, and there is a component of the electron flow associated with the reconnection current in the radial direction. This radial component of electron velocity pulls the reconnecting field lines, leading to a shift in position of the X-point, asymmetric outflow, and asymmetric downstream pressure. Reversing the toroidal field direction changes the direction of the shift, but because of cylindrical geometry effects, this also changes the reconnection rate and radial pressure profile (Inomoto et al. 2006; see also Chapter 2). Recent simulations of spheromak merging in SSX show reconnection with much stronger radially inward-directed

outflow even though the plasma pressure near $R = 0$ is large due to a pileup of exhaust (Lin et al. 2008). These results suggest that considerations of asymmetry in the outflow direction are important for the interpretation of bi-directional jets recently reported in experiment (Brown et al. 2006).

Chapter 2 reports on simulations of the reconnection process in the geometry of MRX which show that asymmetric inflow occurs during the pull mode of operation and asymmetric outflow during the push mode of operation. The inboard side of the current sheet is more susceptible to buildup or depletion of density due to the lesser available volume than on the outboard side of the current sheet. As a result of the pressure buildup at low radii during push reconnection, the X-point is located closer to the outboard side of the current sheet than the inboard side. Consequently, the radially inward-directed outflow is subjected to a stronger tension force than the radially outward-directed outflow, allowing comparable outflow velocities from both the inboard and outboard sides of the current sheet [note that a similar effect is discussed by Galsgaard & Roussev (2002)]. During several time intervals in these simulations and despite the higher pressure in the inboard downstream region, the radially inward-directed outflow is found to be quicker than the radially outward-directed outflow.

Oka et al. (2008) present particle-in-cell (PIC) simulations of reconnection where outflow from one end of the current sheet is impeded by a hard wall while outflow from the other end encounters no such obstruction. They find that the X-line retreats from the wall at a velocity of $\sim 0.1V_A$ and that the reconnection rate is largely unchanged from the symmetric case. Moreover, there is a separation between the ion flow stagnation point and the magnetic field null, with the field null located further from the wall than the ion flow stagnation point. In a work that relates asymmetry in the inflow direction with asymmetry

in the outflow direction, Swisdak et al. (2003) find that the presence of a density gradient in the inflow direction across a current sheet can lead to a drift of the X-line in the electron diamagnetic drift direction when a guide field is present (see also Rogers & Zakharov 1995). The reconnection process is suppressed when the drift velocity is comparable to or greater than the Alfvén velocity. The effects of X-point motion and asymmetry in the outflow direction during Petschek (1964) reconnection have also been considered (Owen & Cowley 1987a, b; Kiehas et al. 2007, 2009; Baty et al. 2009).

This chapter includes a control volume analysis for a current sheet with asymmetric downstream pressure and test the resulting scaling relations against simulations. The objectives are to determine (1) the relationship between the upstream parameters, the downstream pressures, and the reconnection outflow velocity, (2) how the reconnection rate is affected by asymmetric downstream pressure, (3) what sets the positions of the magnetic field null and flow stagnation point, and (4) how to describe reconnection in cylindrical geometry when the outflow is aligned with the radial direction.

Section 3.2 includes a presentation of the equations of resistive MHD which are then written in a time-independent integral form that is amenable to a control volume analysis. Section 3.3 contains a review of the effects of symmetric downstream pressure on antiparallel reconnection and the development of scaling relations for a current sheet with asymmetric downstream pressure. Section 3.4 reports on a similar analysis for a current sheet in cylindrical geometry with outflow aligned with the radial direction. Tests of the scaling relations derived in Sections 3.3 and 3.4 are included in Sections 3.3.4 and 3.4.2, respectively. The importance of asymmetric downstream pressure due to the background plasma pressure distribution is estimated in Section 3.5 for flux cancellation events and the Earth's magnetotail.

Conclusions for Chapter 3 are included in Section 4.1.

3.2 Equations of Magnetohydrodynamics

The equations of resistive MHD in conservative form (e.g., Goedbloed & Poedts 2004, pp. 165–166) are

$$\frac{\partial \rho}{\partial t} + \nabla \cdot (\rho \mathbf{V}) = 0, \quad (3.1)$$

$$\frac{\partial(\rho \mathbf{V})}{\partial t} + \nabla \cdot \left[\rho \mathbf{V} \mathbf{V} + \left(p + \frac{B^2}{2\mu_0} \right) \hat{\mathbf{I}} - \frac{\mathbf{B} \mathbf{B}}{\mu_0} \right] = 0, \quad (3.2)$$

$$\frac{\partial \mathcal{E}}{\partial t} + \nabla \cdot \left[\left(\frac{\rho V^2}{2} + \frac{\gamma}{\gamma - 1} p \right) \mathbf{V} + \frac{\mathbf{E} \times \mathbf{B}}{\mu_0} \right] = 0, \quad (3.3)$$

$$\frac{\partial \mathbf{B}}{\partial t} + \nabla \times \mathbf{E} = 0, \quad (3.4)$$

$$\mu_0 \mathbf{J} = \nabla \times \mathbf{B}, \quad (3.5)$$

$$\mathbf{E} + \mathbf{V} \times \mathbf{B} = \eta \mathbf{J}. \quad (3.6)$$

In order, these are the continuity equation, the momentum equation, the energy equation, Faraday's law, Ampere's law ignoring displacement current, and the resistive MHD Ohm's law. Here \mathbf{B} is the magnetic field, \mathbf{E} is the electric field, \mathbf{V} is the bulk plasma velocity, \mathbf{J} is the current density, p is the plasma pressure, ρ is mass density, η is the plasma resistivity, $\mathcal{E} \equiv \rho V^2/2 + p/(\gamma - 1) + B^2/2\mu_0$ is the total energy density, γ is the ratio of specific heats. The identity dyadic tensor is given by $\hat{\mathbf{I}} = \hat{\mathbf{x}}\hat{\mathbf{x}} + \hat{\mathbf{y}}\hat{\mathbf{y}} + \hat{\mathbf{z}}\hat{\mathbf{z}}$. Except as noted, SI units are used throughout this chapter.

Following the approach presented by Cassak & Shay (2007), by assuming a steady state, integrating over an arbitrary closed volume \mathcal{V} bounded by a surface \mathcal{S} , and using the

divergence theorem, the continuity, momentum, and energy equations can be written as

$$\oint_{\mathcal{S}} d\mathbf{S} \cdot (\rho \mathbf{V}) = 0, \quad (3.7)$$

$$\oint_{\mathcal{S}} d\mathbf{S} \cdot \left[\rho \mathbf{V} \mathbf{V} + \left(p + \frac{B^2}{2\mu_0} \right) \hat{\mathbf{i}} - \frac{\mathbf{B} \mathbf{B}}{\mu_0} \right] = 0, \quad (3.8)$$

$$\oint_{\mathcal{S}} d\mathbf{S} \cdot \left[\left(\frac{\rho V^2}{2} + \frac{\gamma p}{\gamma - 1} \right) \mathbf{V} + \left(\frac{\mathbf{E} \times \mathbf{B}}{\mu_0} \right) \right] = 0, \quad (3.9)$$

where $d\mathbf{S}$ is a differential area element pointing in the outward normal direction to \mathcal{S} .

Similarly, with the help of Stokes' theorem, equation (3.4) can be written as

$$\oint_{\mathcal{S}} d\mathbf{S} \times \mathbf{E} = 0. \quad (3.10)$$

Equations (3.7)–(3.10) are valid for any arbitrary closed volume, provided a steady-state has been achieved. These surface integrals are evaluated in Sections 3.3 and 3.4 in order to investigate reconnection with asymmetry in the outflow direction for linear and cylindrical geometry.

3.3 Linear Geometry

The Sweet-Parker model (Sweet 1958; Parker 1957) describes symmetric steady-state antiparallel magnetic reconnection in the resistive MHD framework when compressibility, viscosity, and downstream pressure are unimportant. This section extends the Sweet-Parker model to account for situations where there is asymmetric downstream pressure. After reviewing the effects of symmetric downstream pressure on the reconnection process in Section 3.3.1, the case of asymmetric downstream pressure is considered in Section 3.3.2. The internal structure of such an asymmetric current sheet is then investigated in Section 3.3.3. Tests of these scaling relations against resistive MHD simulations are presented in Section 3.3.4.

3.3.1 Effects of Symmetric Downstream Pressure

The effects of symmetric downstream pressure on a Sweet-Parker current sheet are discussed by Priest and Forbes (2000, pp. 123–126). Presently, their results are reviewed using the technique that is employed later this section for a current sheet with asymmetric downstream pressure while relaxing their assumptions regarding compressibility (see also Parker 1963; Chae et al. 2003; Litvinenko & Chae 2009). In this derivation V_{in} is the characteristic plasma inflow velocity, B_{in} is the characteristic upstream magnetic field strength, p_{in} is the characteristic upstream plasma pressure, p_{out} is the characteristic downstream plasma pressure, ρ_{in} is the characteristic upstream density, ρ_{out} is the characteristic downstream density, J_y is the characteristic out-of-plane current density inside the reconnection layer, E_y is the characteristic out-of-plane electric field, L is the current sheet half-length, δ is the current sheet half-thickness, and V_{out} is the characteristic outflow velocity. Define x as the outflow direction, y as the out-of-plane direction, and z as the inflow direction ($\hat{\mathbf{x}} \times \hat{\mathbf{y}} = \hat{\mathbf{z}}$).

Everywhere except in the vicinity of the neutral line, the ideal Ohm's law ($\mathbf{E} + \mathbf{V} \times \mathbf{B} = 0$) is valid. Because of the steady state assumption, the electric field is constant. This yields the relation

$$E_y = V_{in} B_{in} \quad (3.11)$$

for conservation of flux. This value for the electric field is valid everywhere. The out-of-plane current density can be estimated from Ampere's law using that B_x reverses over a distance of $\sim 2\delta$. Hence,

$$J_y \sim \frac{B_{in}}{\mu_0 \delta} \quad (3.12)$$

in the current sheet. The inflow velocity V_{in} , current sheet half-thickness δ , and resistivity

η are related by the relationship

$$V_{in} \sim \frac{\eta}{\mu_0 \delta}. \quad (3.13)$$

This dimensionally represents the steady-state condition where the resistive electric field ηJ_y within the layer matches the ideal $(-\mathbf{V} \times \mathbf{B})$ electric field outside the layer. Essentially, for a given inflow velocity in steady state reconnection, the thickness is set by how quickly the magnetic field is able to diffuse.

Evaluation of the conservation of mass relation given in equation (3.7) yields the relation

$$\rho_{in} V_{in} L \sim \rho_{out} V_{out} \delta. \quad (3.14)$$

The conservation of momentum surface integral given in equation (3.8) is satisfied by any distribution of fluxes with the assumed symmetry when integrating over the outer boundary of the current sheet. Evaluation of the conservation of energy relation given in equation (3.9) yields the relation

$$V_{in} L \left(\alpha p_{in} + \frac{B_{in}^2}{\mu_0} \right) \sim V_{out} \delta \left(\alpha p_{out} + \frac{\rho_{out} V_{out}^2}{2} \right), \quad (3.15)$$

where contributions from upstream kinetic energy and downstream magnetic energy are neglected (e.g., Litvinenko & Chae 2009). Here the definition $\alpha \equiv \gamma/(\gamma - 1)$ is used.

Dividing equation (3.15) by equation (3.14) and rearranging gives the scaling relation

$$V_{out}^2 \sim V_A^2 - \alpha \left(\frac{p_{out}}{\rho_{out}} - \frac{p_{in}}{\rho_{in}} \right) \quad (3.16)$$

where $V_A \equiv B_{in}/\sqrt{\mu_0 \rho_{in}}$ is the upstream Alfvén speed and factors of order unity are ignored.

Using equation (3.13), the scaling for the dimensionless reconnection rate can then be written as

$$\frac{V_{in}}{V_A} \sim \frac{1}{S^{1/2}} \sqrt{\frac{\rho_{out}}{\rho_{in}}} \left[1 - \frac{\alpha}{V_A^2} \left(\frac{p_{out}}{\rho_{out}} - \frac{p_{in}}{\rho_{in}} \right) \right]^{1/4} \quad (3.17)$$

where the Lundquist number is given by $S \equiv \mu_0 L V_A / \eta$. The Sweet-Parker scalings of $V_{out} \sim V_A$ and $V_{in}/V_A \sim S^{-1/2}$ are recovered when ρ_{out}/ρ_{in} and the quantity in brackets are independent of S . Compressibility acts to reduce the bottleneck caused by conservation of mass when the outflow density is greater than the inflow density.

As can be seen from equation (3.17), the dependence of the downstream pressure on the reconnection rate is relatively weak except when the bracketed quantity is close to zero. Equations (3.13) and (3.14) provide the relation

$$\delta \sim \frac{\rho_{in} V_{in} L}{\rho_{out} V_{out}} \sim \sqrt{\frac{\rho_{in}}{\rho_{out}} \frac{\eta}{\mu_0} \frac{L}{V_{out}}}. \quad (3.18)$$

For a given density ratio ρ_{in}/ρ_{out} and assuming that L is given, a decrease in the outflow velocity leads to an increase in the current sheet thickness. Because $\delta \sim V_{out}^{-1/2}$, and δ and V_{in} are inversely related ($\delta \sim V_{in}^{-1}$) from equation (3.13), the inflow velocity is only proportional to the square root of the outflow velocity ($V_{in} \sim V_{out}^{1/2}$). If, on the other hand, V_{in} is assumed given and L is free to vary, then greater downstream pressure corresponds to a current sheet of shorter length.

3.3.2 Effects of Asymmetric Downstream Pressure

The next step is to consider a current sheet with symmetric inflow but with asymmetric outflow and downstream pressure. In this framework, it is necessary to assume that the current sheet position and structure are static within an inertial reference frame. For example, reconnection could be externally driven in such a way that constrains the position of the current sheet. The setup of this problem is shown in Figure 3.1. The current sheet has a half-thickness δ and is split into three regions of lengths L_L , ϵ , and L_R , with boundaries at the flow stagnation point and magnetic field null, as indicated in Figure 3.1. The length ϵ is the distance between the magnetic field null and the flow stagnation point. These two

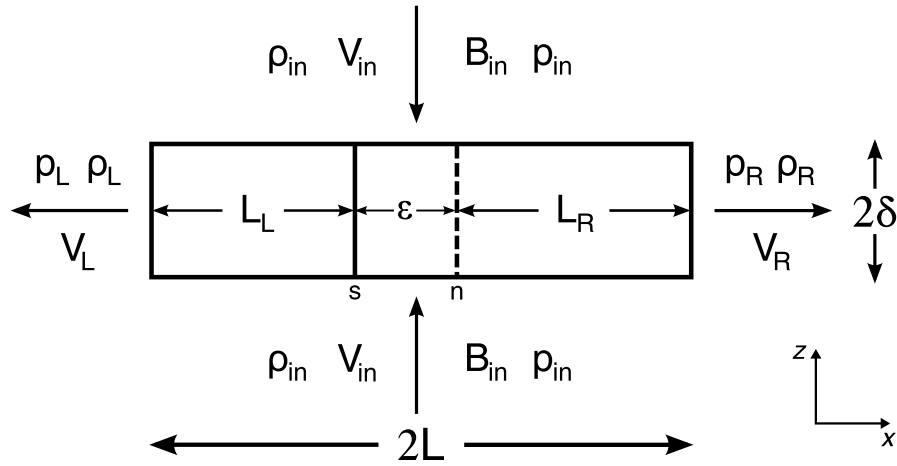


Fig. 3.1.—: Sweet-Parker-like reconnection with asymmetric downstream pressure and a pressure gradient through the current sheet. The solid vertical bar inside the current sheet (marked s) represents the flow stagnation point and the dashed vertical bar (marked n) represents the magnetic field null.

points will overlap only in the absence of a pressure gradient at the magnetic field null. The full length of the current sheet, $2L$, is defined to be

$$2L = L_L + \epsilon + L_R. \quad (3.19)$$

Throughout this paper, a subscript s refers to the value of a field at the flow stagnation point while a subscript n corresponds to the magnetic field null.

To proceed, the surface integrals given in equations (3.7)–(3.9) are evaluated over the whole volume of the current sheet depicted in Figure 3.1. This way, the details of the pressure profile in the x -direction inside the current sheet do not need to be known; rather, only knowledge of the characteristic upstream plasma pressure p_{in} and the characteristic downstream plasma pressures p_L and p_R is required. The conservation of mass surface

integral given in equation (3.7) yields the relation

$$2L\rho_{in}V_{in} \sim \rho_L V_L \delta + \rho_R V_R \delta. \quad (3.20)$$

Evaluation of the component of the conservation of momentum surface integral given in equation (3.8) in the outflow direction yields a relation between the plasma pressures and momentum fluxes from each exit of the reconnection layer,

$$\rho_L V_L^2 + p_L \sim \rho_R V_R^2 + p_R. \quad (3.21)$$

Because the current sheet is assumed to be long and thin, the above relation ignores forces due to the downstream magnetic field. However, magnetic tension does not need to be negligible throughout the volume of integration for this relationship to hold; rather, net tension from the boundary need only be small compared to the terms in equation (3.21). If the upstream magnetic field is not parallel to the boundaries along $z = \pm\delta$ in a way which is not symmetric in the outflow direction, this may yield an additional contribution by tension towards momentum balance in the outflow direction for modest aspect ratio current sheets. The momentum flux into the current sheet is assumed to not give a significant contribution to momentum balance in the outflow direction. Force balance must be met in both the inflow and outflow directions simultaneously in order for the assumption of time-independence to be valid.

Using the expression for the electric field given in equation (3.11), the energy conservation integral (3.9) provides the relation

$$2LV_{in} \left(\alpha p_{in} + \frac{B_{in}^2}{\mu_0} \right) \sim V_L \delta \left(\alpha p_L + \frac{\rho_L V_L^2}{2} \right) + V_R \delta \left(\alpha p_R + \frac{\rho_R V_R^2}{2} \right). \quad (3.22)$$

The above relation neglects upstream kinetic energy and downstream magnetic energy. The derivation of equation (3.13), which relates the inflow velocity, resistivity, and current sheet

thickness, is unchanged in the presence of asymmetric downstream pressure.

Using equation (3.20) to eliminate $2LV_{in}$ from equation (3.22) and equation (3.21) to eliminate V_R provides the cubic relationship for V_L^2 ,

$$0 \sim C_{6L}V_L^6 + C_{4L}V_L^4 + C_{2L}V_L^2 + C_{0L}. \quad (3.23)$$

The coefficients for the above relation are functions of the upstream magnetic field strength as well as the upstream and downstream densities and pressures, and are given by

$$C_{6L} \equiv \frac{1}{4} \left(\frac{\rho_L^3}{\rho_R} - \rho_L^2 \right), \quad (3.24)$$

$$C_{4L} \equiv \frac{\rho_L^2}{\rho_R} \left(\alpha p_R - \frac{3}{4} \Delta p \right) - \alpha \rho_L p_L, \quad (3.25)$$

$$C_{2L} \equiv \rho_L (\rho_R - \rho_L) c_{in}^4 + 2\rho_L \Delta p (1 - \alpha) c_{in}^2 - \alpha^2 p_L^2 + \alpha^2 p_R^2 \left[\frac{\rho_L}{\rho_R} \left(1 - \frac{\Delta p}{2\alpha p_R} \right) \left(1 - \frac{3\Delta p}{2\alpha p_R} \right) \right], \quad (3.26)$$

$$C_{0L} \equiv -\rho_R \Delta p \left[c_{in}^2 - \frac{1}{2} \left(\frac{2\alpha p_R - \Delta p}{\rho_R} \right) \right]^2, \quad (3.27)$$

where the velocity c_{in} is given by

$$c_{in}^2 \equiv \frac{B_{in}^2}{\mu_0 \rho_{in}} + \alpha \frac{p_{in}}{\rho_{in}}, \quad (3.28)$$

and the average downstream pressure \bar{p} and the pressure difference Δp are defined to be

$$\bar{p} \equiv \frac{p_L + p_R}{2}, \quad (3.29)$$

$$\Delta p \equiv p_R - p_L. \quad (3.30)$$

Equation (3.23) can be solved analytically using the method of Cardano (1545), or numerically with a root-finding technique. In the symmetric limit, $C_{0L} = C_{2L} = C_{4L} = C_{6L} = 0$, thus satisfying equation (3.23) trivially for this limiting case. Symmetric results can be recovered by using that $C_{6L} = 0$ and factoring Δp from the remaining terms. The solution

of equation (3.23) for asymmetric conditions is sensitive to discrepancies between the left hand and right hand sides of equations (3.20), (3.21), and (3.22). However, if ϖ is equal to the right hand side divided by the left hand side of equation (3.20), and ς is equal to the right hand side divided by the left hand side of equation (3.22), then the transformation $c_{in}^2 \rightarrow (\varsigma/\varpi) c_{in}^2$ will algebraically account for different scaling factors for the left and right hand sides of equations (3.20) and (3.22) in equations (3.23)–(3.27).

Equation (3.23) simplifies for some special cases. When $\rho_L = \rho_R \equiv \rho_{out}$, the coefficient $C_{\delta L}$ vanishes, leaving a quadratic equation in V_L^2 . In the incompressible limit with $\rho_{in} = \rho_L = \rho_R \equiv \rho$ and $\alpha = 1$, the solution becomes

$$V_{L,R}^2 \sim \sqrt{4 \left(c_{in}^2 - \frac{\bar{p}}{\rho} \right)^2 + \left(\frac{\Delta p}{2\rho} \right)^2} \pm \frac{\Delta p}{2\rho}, \quad (3.31)$$

where the plus and minus signs refer to V_L and V_R , respectively, and equation (3.21) is used. This gives the expected result that the outflow speed is slower on the side with higher downstream pressure.

Next, consider the special case with $p_L = p_R = p_{out}$, but where the downstream densities can be different. In this case, C_{0L} vanishes, again leaving a quadratic equation. The solution is

$$V_{L,R}^2 \sim c_{in}^2 \sqrt{\frac{\rho_{R,L}}{\rho_{L,R}}} - \alpha \frac{p_{out}}{\rho_{L,R}}, \quad (3.32)$$

where factors of order unity are ignored. This equation shows that the outflow speed is higher on the low density side. The scalings presented in equations (3.31) and (3.32) both reduce to the scaling in equation (3.16) in the symmetric limit.

Equations (3.23), (3.31), and (3.32) were derived solely from the scaling relations for conservation of mass, energy, and momentum without explicitly assuming a dissipation mechanism (see also Cassak & Shay 2007). By using equations (3.13) and (3.20) (and con-

sequently assuming uniform resistive dissipation inside the current sheet), the reconnection rate can be written as

$$\frac{V_{in}}{V_A} \sim \sqrt{\frac{V_L + V_R}{2V_A S}}. \quad (3.33)$$

Equations (3.11) and (3.33) yield the expression

$$E_y \sim B_{in} \sqrt{\frac{\eta (V_L + V_R)}{2\mu_0 L}} \quad (3.34)$$

for the reconnection electric field strength.

Solutions of equation (3.31) for V_L as a function of $p_L - p_{in}$ and $p_R - p_{in}$ in units of the upstream magnetic pressure are presented in Figure 3.2 for the incompressible limit. The value for V_R can be found by switching the values for $p_L - p_{in}$ and $p_R - p_{in}$. The outflow velocity from one end does not depend strongly on the downstream pressure from the opposite end. For $p_L - p_{in} = p_R - p_{in} \geq B_{in}^2/\mu_0$, the Poynting flux into the layer is insufficient to drive reconnection, so $V_L = V_R = 0$. Because of the assumptions behind equation (3.21), any pressure difference between p_L and p_R will be associated with a velocity difference between V_L and V_R . These solutions show that it is not necessarily true that reconnection events (e.g., in the solar atmosphere) require bi-directional outflow jets traveling at approximately the Alfvén speed. Rather, in the presence of asymmetric downstream pressure, it is possible to have one Alfvénic jet and one sub-Alfvénic jet (see also Roussev et al. 2001).

The normalized reconnection rate, $S^{1/2}V_{in}/V_A = \sqrt{(V_L + V_R)/2V_A}$, is shown in Figure 3.3 for the incompressible case using equations (3.31) and (3.33). Even when outflow from one side of the current sheet is completely blocked due to downstream pressure, the reconnection rate can still be large if the outflow from the other side occurs at a sizeable fraction of the Alfvén speed. The reconnection rate goes to zero for $p_L - p_{in} = p_R - p_{in} \geq B_{in}^2/\mu_0$. Reconnection will be greatly slowed only when outflow from both sides of the current sheet

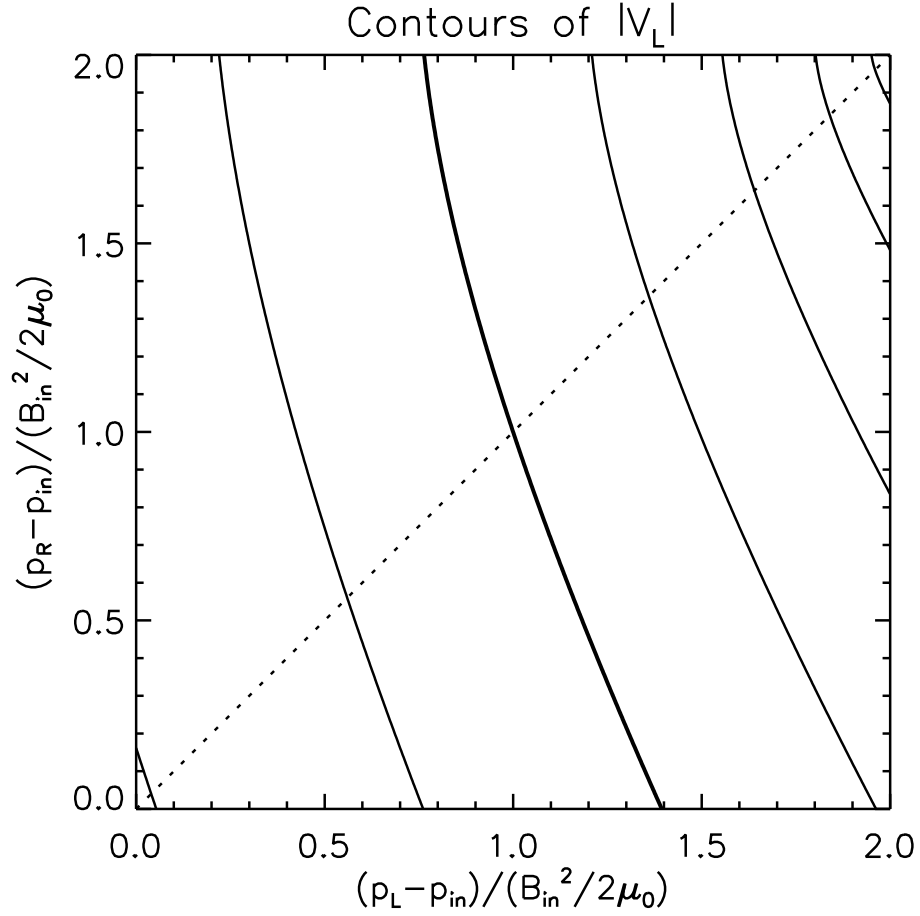


Fig. 3.2.—: The magnitude of flow velocity on the left side of the current sheet, $|V_L|$, calculated from equation (3.31) as a function of $p_L - p_{in}$ and $p_R - p_{in}$. Contours are separated by $0.2V_A$, with the thickest contour representing $V_L = V_A$. The value for V_R can be found by switching p_L and p_R . This figure assumes that the scaling factors in equations (3.20), (3.21), and (3.22) are unity.

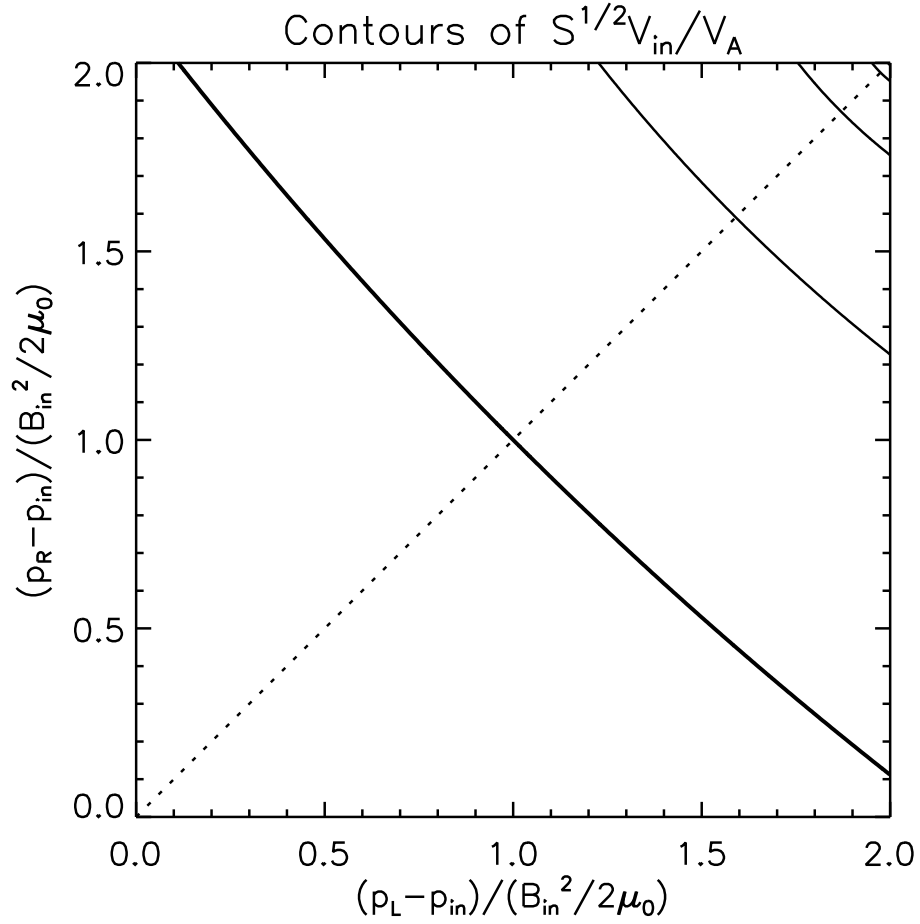


Fig. 3.3.—: The normalized reconnection rate, given by $S^{1/2}V_{in}/V_A = \sqrt{(V_L + V_R)/2V_A}$, as a function of $p_L - p_{in}$ and $p_R - p_{in}$ and calculated using equation (3.31) to find V_L and V_R . The contours are separated by 0.2, with the thickest contour representing a value of 1. This figure assumes that the scaling factors in equations (3.20), (3.21), and (3.22) are unity.

is blocked. This is consistent with the simulations of X-line retreat reported by Oka et al. (2008), in which the reconnection rate is not greatly affected when outflow from one reconnection jet is impeded by the presence of an obstacle while the other outflow jet has no such obstruction.

These scaling relations show that the reconnection rate is allowed to remain relatively high because the current sheet becomes thicker (e.g., δ becomes larger) in the presence of increased downstream pressure. For cases where the length of the current sheet is prescribed and the inflow velocity is presumed unknown, higher downstream pressure corresponds to a decrease in the inflow velocity and an increase in the thickness of the current sheet. For cases where the inflow velocity is prescribed and the length of the current sheet is presumed unknown, higher downstream pressure corresponds to a decrease in the length and an increase in the thickness of the current sheet in order to maintain the same reconnection rate.

This analysis requires knowledge of both upstream and downstream parameters in order to calculate outflow velocities and reconnection rates. This model is consequently less predictive than the model for reconnection with asymmetry in the inflow direction given by Cassak & Shay (2007), which only requires knowledge of upstream parameters. Nevertheless, this model sheds light on how the upstream and downstream parameters interact to give a reconnection rate. More accurate treatments likely require the use and interpretation of numerical simulations to self-consistently capture the time-dependent interplay between small and large scales during the reconnection process and effects associated with current sheet motion.

3.3.3 Internal Structure of an Asymmetric Current Sheet

Now that the global quantities associated with a current sheet with asymmetric downstream pressure can be found, the internal structure of the current sheet can be investigated. As in the model by Cassak & Shay (2007) the position of the flow stagnation point is set by conservation of mass. Evaluation of equation (3.7) inside the current sheet yields the conservation of mass relations

$$\rho_{in}V_{in}L_L \sim \rho_L V_L \delta, \quad (3.35)$$

$$\rho_{in}V_{in}\epsilon \sim \rho_n V_n \delta, \quad (3.36)$$

$$\rho_{in}V_{in}(\epsilon + L_R) \sim \rho_R V_R \delta, \quad (3.37)$$

where ρ_n is the density and V_n is the outflow component of velocity at the magnetic field null. These relations implicitly assume that the inflow velocity and upstream density are not strong functions of position within the current sheet. The location of the flow stagnation point can be derived from equations (3.19), (3.35), and (3.37), and is given by the relations

$$L_L \sim 2L \left(\frac{\rho_L V_L}{\rho_L V_L + \rho_R V_R} \right), \quad (3.38)$$

$$\epsilon + L_R \sim 2L \left(\frac{\rho_R V_R}{\rho_L V_L + \rho_R V_R} \right). \quad (3.39)$$

The densities in equations (3.35)–(3.39) cancel when incompressibility is assumed.

Evaluation of the conservation of energy surface integral given in equation (3.9) inside the current sheet yields the approximate relations

$$V_{in}L_L \left[\alpha p_{in} + \frac{B_{in}^2}{\mu_0} \right] + V_{in}\delta \left(\frac{B_{in}B_s}{\mu_0} \right) \sim V_L\delta \left[\alpha p_L + \frac{\rho_L V_L^2}{2} \right], \quad (3.40)$$

$$V_{in}\epsilon \left[\alpha p_{in} + \frac{B_{in}^2}{\mu_0} \right] \sim V_{in}\delta \left(\frac{B_{in}B_s}{\mu_0} \right) + V_n\delta \left[\alpha p_n + \frac{\rho_n V_n^2}{2} \right], \quad (3.41)$$

$$V_{in}L_R \left[\alpha p_{in} + \frac{B_{in}^2}{\mu_0} \right] + V_n\delta \left[\alpha p_n + \frac{\rho_n V_n^2}{2} \right] \sim V_R\delta \left[\alpha p_R + \frac{\rho_R V_R^2}{2} \right], \quad (3.42)$$

where B_s is the vertical magnetic field strength at the flow stagnation point. When the magnetic field null and flow stagnation point are separated, there will be a Poynting flux across the flow stagnation point and a kinetic energy flux across the magnetic field null.

The next step is to consider the position of the magnetic field null relative to the flow stagnation point in a steady state [see also Malyshkin et al. (2005) for a related analysis]. When time derivatives are negligible, the outflow component of the momentum equation reduces to

$$\rho V_x \frac{\partial V_x}{\partial x} = \frac{B_z}{\mu_0} \frac{\partial B_x}{\partial z} - \frac{\partial p}{\partial x}, \quad (3.43)$$

using the fact that magnetic tension in the current sheet exceeds the magnetic pressure gradient ($|B_z \partial B_x / \partial z| \gg |B_z \partial B_z / \partial x|$). At the flow stagnation point, the magnetic tension force must cancel the pressure gradient force in a steady-state system. Moreover, the magnetic field null is colocated with the flow stagnation point in a steady state only when there is no pressure gradient at the magnetic field null.

Define x_n as the position of the magnetic field null and x_s as the position of the flow stagnation point. By definition, x_s is given by $V_x(x_s) \equiv 0$. Evaluating equation (3.43) at the flow stagnation point using equation (3.12) gives

$$\frac{B_z(x_s)}{\mu_0} \frac{B_{in}}{\delta} \sim \left. \frac{\partial p}{\partial x} \right|_{x=x_s}. \quad (3.44)$$

Using that $B_z(x_n) \equiv 0$, a Taylor expansion to first order yields

$$B_z(x_s) = (x_s - x_n) \left. \frac{\partial B_z}{\partial x} \right|_{x=x_n} + \mathcal{O}(\epsilon^2). \quad (3.45)$$

Hence, an expression for the distance between the flow stagnation point and the magnetic field null for a steady state can be derived,

$$\epsilon \equiv |x_s - x_n| \sim \left(\frac{\mu_0 \delta}{B_{in}} \right) \left(\frac{|\partial p / \partial x|_{x=x_s}}{|\partial B_z / \partial x|_{x=x_n}} \right). \quad (3.46)$$

When the assumptions behind equation (3.43) are valid, the plasma pressure at the flow stagnation point will be greater than the plasma pressure at the magnetic field null.

3.3.4 Comparison to Linear Geometry Simulations

Here, the scaling relations derived in Sections 3.3.2 and 3.3.3 are compared against linear geometry resistive MHD simulations incorporating the geometry and driving mechanism of MRX. Asymmetry in the outflow direction develops for the push mode of operation (Figure 2.2; see also Yamada et al. 1997) when one downstream wall is closer to the current sheet than the other downstream wall. The driving process in these simulations constrains the position of the reconnection layer and thus limits time-dependent motion of the current sheet. Except as otherwise noted, the numerical method and simulation setup are described in Chapter 2.

For these simulations, the resistivity is given by $\eta/\mu_0 = 20 \text{ m}^2 \text{ s}^{-1}$, which corresponds to a Lundquist number of $S \sim 100$ using the half-length of the current sheet and the immediately upstream magnetic field strength and density. The magnetic Prandtl number is given by $\text{Pm} \equiv \nu/(\eta/\mu_0) = 0.25$, with $\nu = D = \chi = 5 \text{ m}^2 \text{ s}^{-1}$. Reconnection is driven by applying an electric field on the surfaces of two flux cores which have a minor radius of 9.4 cm and are located at $(x, z) = (0 \text{ cm}, \pm 27 \text{ cm})$ using the coordinate system established in Section 3.3. In linear geometry, the flux cores are infinite cylinders. The out-of-plane electric field at the surface of the flux cores is 424.4 V/m. The upper and lower boundaries are at $z = \pm 62 \text{ cm}$. For case A, the downstream boundaries are at $x = -22.5 \text{ cm}$ and $x = 32.5 \text{ cm}$. For case B, the downstream boundaries are at $x = -17.5 \text{ cm}$ and $x = 32.5 \text{ cm}$. A cut along $z = 0$ from case B at $13.3 \mu\text{s}$ is shown in Figure 3.4. At this time, the flow stagnation point is at $x = 1.42 \text{ cm}$ and the magnetic field null is at $x = 1.82 \text{ cm}$, indicating

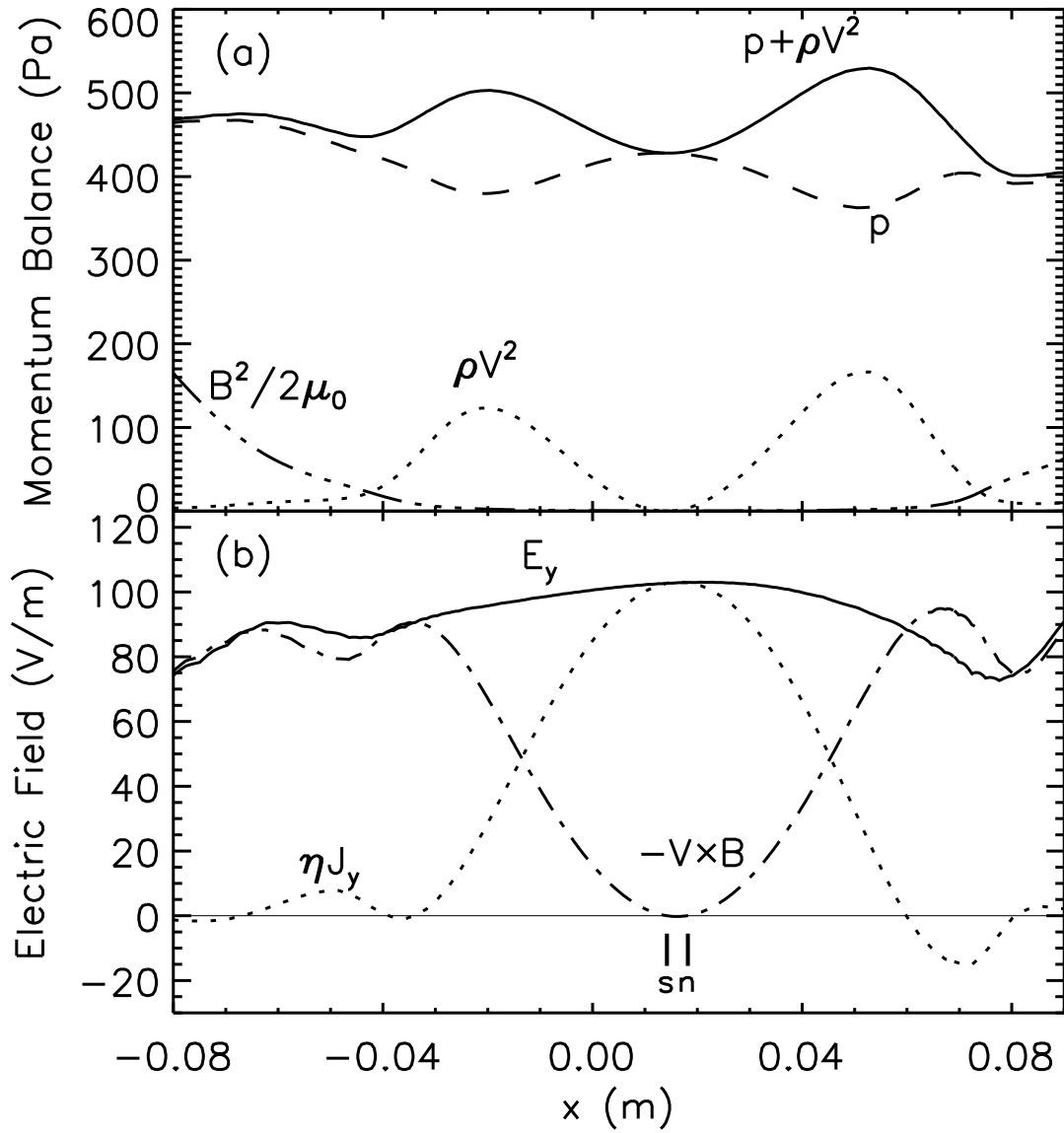


Fig. 3.4.—: A slice in the outflow direction along $z = 0$ of terms from (a) momentum balance and (b) electric field balance for case B at $t = 13.3 \mu\text{s}$. Vertical bars represent the positions of the flow stagnation point (marked s) and the magnetic field null (marked n). The ideal electric field is zero at both the flow stagnation point and the magnetic field null.

a short separation between the two points. The flow stagnation point is located closer to the side with the impeded outflow than the magnetic field null. Magnetic pressure is not important within the current sheet.

To perform quantitative comparisons between the simulations presented in this section and the scaling relations presented in Section 3.3, the relevant quantities must be extracted from the numerical results (see also Cassak & Shay 2007). The full length $2L$ of the current sheet is taken to be the distance along $z = 0$ between the two locations where the out-of-plane current density drops to a fraction f of its peak value, where f is either $1/e$ or $1/e^2$. The thickness of the current sheet, δ , is taken to be the distance in the z direction between the location where the out-of-plane current density peaks and where it falls off to f of its peak value. The values for the upstream fields are extracted from the simulation at $z = \pm\delta$ above and below where the current density peaks. The values for the downstream fields are taken at $z = 0$ where the out-of-plane current density falls to f of its peak value.

Comparisons between simulation and our scaling relations are shown in Figure 3.5, using both of the aforementioned values of f . Figure 3.5(a) compares the left and right hand sides of equation (3.20) which approximates conservation of mass, Figure 3.5(b) compares the left and right hand sides of equation (3.21) regarding momentum balance, and Figure 3.5(c) compares the left and right hand sides of equation (3.22) which approximates conservation of energy. Verification of these scaling relations requires that the data reasonably fit a straight line through the origin. It is not necessary for this line to have a slope of unity (plotted as a dotted line). In Figures 3.5(a), 3.5b, and 3.5(c), the left and right hand sides of each of the equations approximately fit straight lines through the origin with slopes close to unity. In Figures 3.5(a) and 3.5c, the slope is slightly greater than unity (~ 1.15 – 1.2).

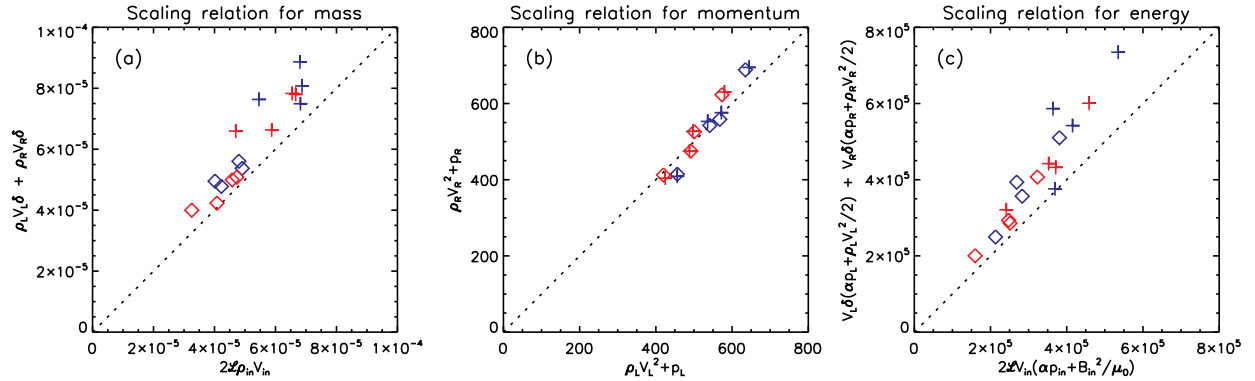


Fig. 3.5.— Comparisons between the scaling relationships derived in Section 3.3 for reconnection with asymmetric downstream pressure and a resistive MHD simulation of the push mode of operation in MRX using linear geometry with one downstream wall closer to the reconnection site than the other. Shown are the left and right hand sides of equations (3.20)–(3.22) representing scaling relations for (a) mass, (b) momentum, and (c) energy. The data points representing cases A and B are plotted in blue and red, respectively, for $f = e^{-1}$ (diamonds) and $f = e^{-2}$ (plus signs). The data were extracted at $9.1 \mu\text{s}$, $11.2 \mu\text{s}$, $13.3 \mu\text{s}$, and $15.4 \mu\text{s}$.

Extracted values for simulation results and predicted parameters using these results are shown in Table 3.1 for $t = 13.3 \mu s$ and $f = e^{-2}$. The first eighteen quantities are directly extracted from simulation results using the method described above. The bottom five quantities are predictions using equations (3.21), (3.23), (3.34), (3.38), and (3.46). Equation (3.23) is evaluated assuming that the scaling factors given in equations (3.20), (3.21), and (3.22) are unity. The predicted and observed values for V_L and V_R differ by $\sim 15\text{--}30\%$ for each case, possibly due to scaling factors. The position of the flow stagnation point is within 2 mm of the predicted value for each case. The comparison between the observed and predicted values for ϵ is complicated because the pressure gradient varies by a factor of ~ 2 between x_s and x_n . The values in the table correspond to $\partial p/\partial x$ evaluated at the flow stagnation point as in equation (3.46); however, for case B if $\langle \partial p/\partial x \rangle$ is used (where the average is taken between x_s and x_n), then the prediction of $\epsilon = 3.6$ mm better matches the simulation result of $\epsilon = 4.1$ mm. The position of the flow stagnation point is within 2 mm of the predicted value for each case. The predicted electric field is $\sim 20\%$ below the peak resistive electric field $\eta J_{y,max}$. However, Figure 3.4 shows that the predicted electric field better matches the total electric field in the wings of the reconnection layer.

3.4 Cylindrical Geometry

Axisymmetric magnetic reconnection in cylindrical coordinates (R, Z, ϕ) with outflow aligned with the radial direction is considered here. The setup of this problem is shown in Figure 3.6. Inflow occurs on the annuli defined by $R \in [R_1, R_2]$ for $Z = \pm\delta$. Outflow occurs on two cylindrical surfaces at radii R_1 and R_2 for $Z \in [-\delta, \delta]$, with velocities V_1 and V_2 , respectively. In astrophysics, this is potentially applicable to reconnection events in magnetically confined disks in hot star winds (e.g., Nakajima 1985; Cassinelli et al. 2002;

Table 3.1. Simulation results and model predictions at $t = 13.3 \mu\text{s}$

Parameter (units)	Case A	Case B
B_{in} (G)	239	216
V_{in} (km s^{-1})	4.10	4.41
V_L (km s^{-1})	39.4	27.0
V_R (km s^{-1})	43.4	33.2
p_{in} (Pa)	199	249
p_L (Pa)	364	383
p_R (Pa)	340	365
ρ_{in} (kg m^{-3})	1.43×10^{-7}	1.65×10^{-7}
ρ_L (kg m^{-3})	1.34×10^{-7}	1.56×10^{-7}
ρ_R (kg m^{-3})	1.25×10^{-7}	1.46×10^{-7}
$\eta J_{y,max}$ (V m^{-1})	115	103
δ (cm)	0.71	0.73
$2L$ (cm)	9.30	8.07
x_L (cm)	-3.81	-2.53
x_s (cm)	0.73	1.41
x_n (cm)	0.93	1.82
x_R (cm)	5.49	5.54
ϵ (cm)	0.20	0.41
V_L (km s^{-1} , predicted) ^a	46.8	19.6
V_R (km s^{-1} , predicted) ^a	50.3	23.0
x_s (cm, predicted) ^b	0.78	1.22
ϵ (cm, predicted) ^c	0.38	0.11
E_y (V m^{-1} , predicted) ^d	101	83

^aFrom equations (3.21) and (3.23).

^bFrom equation (3.38).

^cFrom equation (3.46).

^dFrom equation (3.34).

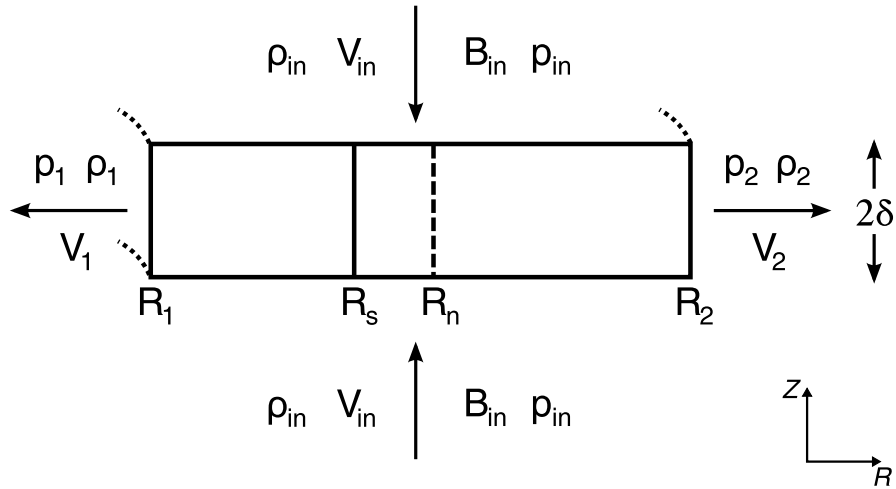


Fig. 3.6.— Sweet-Parker-like reconnection in cylindrical geometry with outflow aligned with the radial direction. Because of the divergence constraint, B_{in} must be a function of radius. The solid vertical bar inside the current sheet represents the flow stagnation point and the dashed vertical bar represents the magnetic field null.

Townsend & Owocki 2005; ud-Doula et al. 2006; ud-Doula et al. 2008). In the context of laboratory plasmas, this setup is appropriate to describe the push mode of reconnection in MRX (Yamada et al. 1997; Inomoto et al. 2006) and general spheromak merging.

As shown in Chapter 2, cylindrical geometry effects can significantly impact the reconnection process even in some situations when the range in radii over which reconnection occurs is small compared to the major radius. This is because it is easier to build up or deplete density on the inboard side of the current sheet than on the outboard side. These geometric effects influence the location of the flow stagnation point and magnetic field null.

3.4.1 Global Properties and Internal Structure

Evaluation of equation (3.7) for the entire current sheet yields the conservation of mass relation

$$(\pi R_2^2 - \pi R_1^2) \rho_{in} V_{in} \sim 2\pi R_1 \delta \rho_1 V_1 + 2\pi R_2 \delta \rho_2 V_2, \quad (3.47)$$

which takes into account the geometry of the current sheet.

The next step is to integrate equation (3.8) over the surface \mathcal{S} bounding the volume \mathcal{V} given by $R \in [R_1, R_2]$, $\theta \in [\theta_1, \theta_2]$, and $Z \in [-\xi/2, \xi/2]$, where ξ is an arbitrarily small length parameter. Contributions from magnetic pressure and tension are ignored; however, there are many cylindrical geometry applications where this assumption is likely to be violated. The surface integrals over the sides located at $Z = \pm\xi/2$ cancel due to symmetry. The problem essentially reduces to a line integral over the boundary of \mathcal{V} located in the $Z = 0$ plane. Side A (B) refers to the circular arc along $R = R_1$ ($R = R_2$) for $\theta \in [\theta_1, \theta_2]$. Side C (D) refers to the line segment along $\theta = \theta_1$ ($\theta = \theta_2$) for $R \in [R_1, R_2]$.

The differential area elements pointing in the outward normal direction are

$$d\mathbf{S}_A = -R_1 (\cos \theta \hat{\mathbf{x}} + \sin \theta \hat{\mathbf{y}}) d\theta dZ, \quad (3.48)$$

$$d\mathbf{S}_B = R_2 (\cos \theta \hat{\mathbf{x}} + \sin \theta \hat{\mathbf{y}}) d\theta dZ, \quad (3.49)$$

$$d\mathbf{S}_C = (\sin \theta_1 \hat{\mathbf{x}} - \cos \theta_1 \hat{\mathbf{y}}) dR dZ, \quad (3.50)$$

$$d\mathbf{S}_D = (-\sin \theta_2 \hat{\mathbf{x}} + \cos \theta_2 \hat{\mathbf{y}}) dR dZ. \quad (3.51)$$

The velocities along sides A and B are

$$\mathbf{V}(R_1, \theta) = -V_1 \cos \theta \hat{\mathbf{x}} - V_1 \sin \theta \hat{\mathbf{y}}, \quad (3.52)$$

$$\mathbf{V}(R_2, \theta) = V_2 \cos \theta \hat{\mathbf{x}} + V_2 \sin \theta \hat{\mathbf{y}}. \quad (3.53)$$

There is no azimuthal component of flow, so there is no contribution from the momentum flux tensor, $\rho\mathbf{V}\mathbf{V}$, in the integrand of equation (3.8) along sides C and D. Define

$$p_m \equiv \frac{1}{R_2 - R_1} \int_{R_1}^{R_2} dR p(R, Z = 0) \quad (3.54)$$

as the mean plasma pressure along a radial line segment between $R = R_1$ and $R = R_2$ for $Z = 0$.

Using equation (3.54), the contributions for each portion of the boundary are then

$$\frac{1}{\xi} \int_A d\mathbf{S}_A \cdot [\rho\mathbf{V}\mathbf{V} + p\hat{\mathbf{i}}] = -R_1 (\rho_1 V_1^2 + p_1) [(\sin \theta_2 - \sin \theta_1) \hat{\mathbf{x}} - (\cos \theta_2 - \cos \theta_1) \hat{\mathbf{y}}], \quad (3.55)$$

$$\frac{1}{\xi} \int_B d\mathbf{S}_B \cdot [\rho\mathbf{V}\mathbf{V} + p\hat{\mathbf{i}}] = R_2 (\rho_2 V_2^2 + p_2) [(\sin \theta_2 - \sin \theta_1) \hat{\mathbf{x}} - (\cos \theta_2 - \cos \theta_1) \hat{\mathbf{y}}], \quad (3.56)$$

$$\frac{1}{\xi} \int_C d\mathbf{S}_C \cdot p\hat{\mathbf{i}} = p_m (R_2 - R_1) (\sin \theta_1 \hat{\mathbf{x}} - \cos \theta_1 \hat{\mathbf{y}}), \quad (3.57)$$

$$\frac{1}{\xi} \int_D d\mathbf{S}_D \cdot p\hat{\mathbf{i}} = p_m (R_2 - R_1) (-\sin \theta_2 \hat{\mathbf{x}} + \cos \theta_2 \hat{\mathbf{y}}). \quad (3.58)$$

For a steady state, the sum of equations (3.55)–(3.58) must equal zero. As necessary, this condition is satisfied if pressure is constant ($p_1 = p_2 = p_m$) and flow is zero ($V_1 = V_2 = 0$). Without loss of generality, take $\theta_1 = 0$. The resulting relation for momentum balance is

$$R_2 (\rho_2 V_2^2 + p_2 - p_m) \sim R_1 (\rho_1 V_1^2 + p_1 - p_m). \quad (3.59)$$

This relation allows $V_1 > V_2$ for some cases even when $p_1 > p_2$. However, in deriving equation (3.59), contributions from magnetic tension are ignored. Because merging in cylindrical geometry often occurs with a modest aspect ratio current sheet, this assumption will not always be satisfied.

Because of the divergence constraint, it is not reasonable to assume that B_{in} will be constant with radius. Consequently, it is reasonable to assume that the upstream magnetic field has the form

$$B_{in}(R) = \frac{B_0 R_0}{R}, \quad (3.60)$$

where B_0 is the reconnecting magnetic field strength at the radius R_0 . The magnetic field is assumed to be purely radial. In this geometry with the electric field purely in the azimuthal direction, the steady-state condition requires $R^{-1}\partial_R(RE_\phi) = 0$ (or equivalently, that the quantity RE_ϕ is constant with radius). Using the magnetic field profile in equation (3.60), the electric field is given by

$$E_\phi(R) = \frac{V_{in}B_0R_0}{R}. \quad (3.61)$$

Using this expression for the azimuthal electric field, the conservation of energy integral given in equation (3.9) can then be evaluated,

$$\begin{aligned} (\pi R_2^2 - \pi R_1^2) V_{in} \alpha p_{in} + \frac{2\pi V_{in} B_0^2 R_0^2}{\mu_0} \ln\left(\frac{R_2}{R_1}\right) \sim \\ 2\pi R_1 \delta V_1 \left(\frac{\rho_1 V_1^2}{2} + \alpha p_1\right) + 2\pi R_2 \delta V_2 \left(\frac{\rho_2 V_2^2}{2} + \alpha p_2\right), \end{aligned} \quad (3.62)$$

where upstream kinetic energy and downstream magnetic energy are neglected.

As in Section 3.3.1, Ampere's law can be used to estimate the out-of-plane current density to be

$$J_\phi(R) \sim \frac{B_0 R_0}{\mu_0 \delta R}. \quad (3.63)$$

By assuming resistive dissipation, the inflow velocity, current sheet thickness, and resistivity remain related by

$$V_{in} \sim \frac{\eta}{\mu_0 \delta}. \quad (3.64)$$

The next step is to investigate the internal structure of the current sheet. As in the linear geometry analysis, the position of the flow stagnation point follows from conservation of mass. Evaluation of equation (3.7) yields the relations

$$\rho_{in} V_{in} \pi (R_s^2 - R_1^2) \sim \rho_1 V_1 (2\pi R_1 \delta), \quad (3.65)$$

$$\rho_{in} V_{in} \pi (R_2^2 - R_s^2) \sim \rho_2 V_2 (2\pi R_2 \delta). \quad (3.66)$$

Dividing equations (3.65) and (3.66) gives

$$R_s \sim \sqrt{\frac{\rho_1 V_1 R_1 R_2^2 + \rho_2 V_2 R_2 R_1^2}{\rho_1 V_1 R_1 + \rho_2 V_2 R_2}} \quad (3.67)$$

after the flow stagnation radius R_s has been solved for. A similar analysis to the linear geometry case can be done to derive more information about the relative positions of the flow stagnation point and magnetic field null.

Further analytic progress can be made by assuming (1) incompressibility, (2) that plasma pressure effects are not important for scaling purposes [e.g., pressure terms are not significant for energy balance and either $R_1(p_1 - p_m) \approx R_2(p_2 - p_m)$ or $\rho_{1,2} V_{1,2}^2 \gg |p_{1,2} - p_m|$], and (3) that the separation between the flow stagnation point and magnetic field null is small. Dividing equations (3.65) and (3.66) then yields the relation

$$\frac{V_1}{V_2} \sim \frac{R_2}{R_1} \left(\frac{R_s^2 - R_1^2}{R_2^2 - R_1^2} \right). \quad (3.68)$$

Equation (3.59) can then be written as

$$\left(\frac{V_1}{V_2} \right)^2 \sim \frac{R_2}{R_1}. \quad (3.69)$$

Conservation of energy on either side of the colocated flow stagnation point and magnetic field null is then described by the relations

$$\frac{2\pi V_{in} B_0^2 R_0^2}{\mu_0} \ln \left(\frac{R_s}{R_1} \right) \sim R_1 V_1 \left(\frac{\rho V_1^2}{2} \right), \quad (3.70)$$

$$\frac{2\pi V_{in} B_0^2 R_0^2}{\mu_0} \ln \left(\frac{R_2}{R_s} \right) \sim R_2 V_2 \left(\frac{\rho V_2^2}{2} \right). \quad (3.71)$$

Dividing equations (3.70) and (3.71) yields the relation

$$\left(\frac{V_1}{V_2} \right)^3 \sim \frac{R_2 \ln(R_s/R_1)}{R_1 \ln(R_2/R_s)}. \quad (3.72)$$

If one of the quantities V_1/V_2 , R_1 , R_s , and R_2 is known, then equations (3.68), (3.69), and (3.72) can be used to solve for the remaining three quantities. The assumptions made to derive equations (3.68)–(3.72) are likely to be violated in a realistic situation. In particular, high pressure is likely to develop at low radii due to the limited available volume (see Chapter 2). However, these relations provide insight into a limiting case in which pressure effects are unimportant.

3.4.2 Driven Reconnection in Cylindrical Geometry

To test the theoretical model given by equations (3.47), (3.59), and (3.62) for reconnection in cylindrical geometry with outflow aligned with the radial direction, comparisons are made to the resistive MHD simulation of MRX’s push mode of operation using cylindrical geometry reported in Section 2.4.2. The method of extracting length scales and upstream/downstream parameters for this simulation is analogous to the method described in Section 3.3.4, with the inner and outer radii R_1 and R_2 defined to be the positions where the toroidal current density along $Z = 0$ drops to f of its peak value.

Figure 3.7(a) compares the left and right hand sides of equation (3.47) which approximates conservation of mass, Figure 3.7(b) compares the left and right hand sides of equation (3.59) which approximates radial momentum balance, and Figure 3.7(c) compares the left and right hand sides of equation (3.62) which approximates conservation of energy. In Figure 3.7(a), the left and right hand sides differ by $\sim 30\text{--}45\%$ for $f = e^{-1}$ but only by $\sim 6\text{--}20\%$ for $f = e^{-2}$. In Figure 3.7(b), agreement is better at later times. Note that the magnitudes of many of the individual terms in equation (3.59) are larger than the total values for the left and right hand sides. At $t = 11.9 \mu\text{s}$ and at other times in the simulation, $V_1 > V_2$ even though $p_1 > p_2$. The data in Figure 3.7(c) show that the Poynting flux into the reconnection

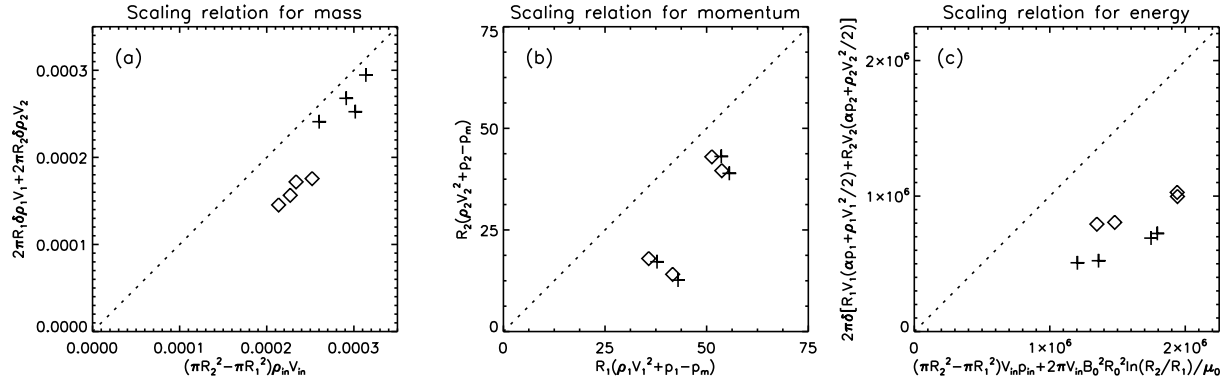


Fig. 3.7.—: Comparisons between the scaling relationships derived in Section 3.4 for reconnection in cylindrical geometry with outflow aligned with the radial direction, and the resistive MHD simulation of the push mode of operation of MRX reported in Section 2.4.2. Shown are the left and right hand sides of equations (3.47), (3.59), and (3.62) representing scaling relations for (a) mass, (b) momentum, and (c) energy, where the symbol conventions of Figure 3.5 are used. The data were extracted at $9.1 \mu\text{s}$, $11.9 \mu\text{s}$, $13.3 \mu\text{s}$, and $15.4 \mu\text{s}$.

layer is overestimated because equation (3.62) does not account for the upstream magnetic field becoming partially vertical along the low and high radii portions of the current sheet.

3.4.3 Discussion

This section provides scaling relations for reconnection in cylindrical geometry with outflow aligned with the radial direction. Equations (3.47), (3.59), and (3.62) are analogous to equations (3.20), (3.21), and (3.22) from Section 3.3. As in the linear geometry model, these expressions were derived without explicitly specifying which mechanism breaks magnetic field lines. These expressions also depend on both upstream and downstream parameters.

The magnetic field profile assumed in equation (3.60) is idealized in its present form, but can be modified to more accurately represent the upstream magnetic field. In particular, there will often be a vertical component of the upstream magnetic field near R_1 and R_2 which does not contribute to the Poynting flux into the layer but can contribute to the tension term in equation (3.8). Consequently, a profile for the upstream magnetic field which allows for a vertical component near R_1 and R_2 is likely to be more appropriate in many situations. However, it is difficult to make an assumption about the upstream magnetic field profile *a priori*. Comparisons with simulation suggest that such effects are likely important for the cylindrical geometry simulations of push reconnection reported in Chapter 2.

Equation (3.59), which describes momentum balance in the outflow direction, shows that it is possible for the radially inward-directed outflow to leave the current sheet at a greater speed than the radially outward-directed outflow, even when there is greater pressure on the inboard side of the current sheet than the outboard side. Such an effect is observed at several times in these simulations. This result suggests that effects related to geometry,

pressure, and asymmetry in the outflow direction are important for the interpretation of bi-directional jets observed in spheromak merging experiments (e.g., Brown et al. 2006), especially when the aspect ratio is small. The ratio of kinetic energy flux towards both low radii and high radii is likely to have important consequences on the system as a whole.

This section assumes that the magnetic field is purely poloidal and the outflow is purely radial. In astrophysical disks, however, there are likely to be components of flow and magnetic field in the azimuthal direction as a result of orbital motion. During spheromak merging, there will likely be toroidal flow along with a toroidal component of the reconnecting magnetic field. The analysis performed in this section will need to be extended in order to account for these considerations.

The scaling relations presented in this section can be compared with information from devices such as SSX, MRX, and TS-3/4. Measurements of the outflow velocity are often made using ion Doppler spectroscopy (IDS) which requires an average over a chord, but it may be possible to choose a chord that is inclined with respect to the midplane of the experiment or to place an obstruction near $R = 0$ so that the line of sight includes one crossing of a reconnection site rather than two. Mach probes can also be used to measure velocity, but may obstruct the flow. The scalings by Cassak and Shay (2007) for reconnection with asymmetry in the inflow direction may also be testable using the pull mode of reconnection in MRX, although effects related to downstream pressure may need to be taken into account.

3.5 Applicability to Flux Cancellation and the Magnetotail

An appropriate application of the model presented in this chapter is to flux cancellation events in the vicinity of the solar photosphere (e.g., Martin et al. 1985; Litvinenko 1999).

These events are believed to be associated with reconnection because of the observation of upflows (e.g., Martin 1990; Litvinenko & Martin 1999) and downflows (e.g., Chae et al. 2004) that are consistent with reconnection events. While reconnection events in the corona are often explosive, photospheric reconnection events are typically steady and resistive. Thus, the assumptions of time-independence and an elongated current sheet are more likely to be met. Litvinenko (1999) argues that such large-scale reconnection events should have a characteristic length scale no longer than a scale height (~ 100 km) and occur at $z \sim 600$ km above the photosphere. Using the model for the solar atmosphere given by equation (3) of Gary (2001), the plasma pressure drops from ~ 1500 to ~ 700 dyne cm^{-2} between $z = 500$ km and $z = 600$ km. The magnetic field in this region is of order 100–500 G, corresponding to $\beta \sim 0.1$ –3. This estimate shows that effects associated with asymmetric downstream pressure are likely to be important during photospheric reconnection (see also Roussev et al. 2001; Galsgaard & Roussev 2002). However, this estimate does not take into account local variations in plasma pressure associated with reconnection events, including the ability of reconnection to set its own downstream pressure (as seen in Chapter 2).

Using the information from Gary (2001), it is possible to make a crude application of the linear geometry model to flux cancellation events. Such an application is shown in Table 3.2. The reconnection layer is assumed to be vertical and of length 100 km between $z = 500$ km and $z = 600$ km. As before, the plasma pressure is calculated from equation (3) of Gary (2001). The number density is estimated to be $n = 5 \times 10^{15}$ cm^{-3} in both the upstream and downstream regions, corresponding to $\rho = 8.35 \times 10^{-6}$ kg m^{-3} . However, incompressibility is not otherwise assumed. The upstream magnetic field is chosen to be 200 G. The resistivity in Table 3.2 corresponds to $T = 4200$ K. The choice of $\gamma = 1.2$ rather than $\gamma = 5/3$ is made to approximate the effects of thermal conduction and radiative losses

that soften the equation of state. Equations (3.13), (3.20) (3.21), are (3.23) are used to calculate V_{lower} , V_{upper} , V_{in} , and δ . The asymmetry in outflow velocity is of order $\sim 10\%$. The effects of asymmetry are reduced for low β plasmas and increased for soft equations of state, but will also increase if there is a buildup of reconnection exhaust in one downstream region but not the other.

Another possible application of this model is to reconnection in the near-Earth magnetotail (e.g., the events reported by Mukai et al. 2000; Sergeev et al. 2008). Reconnection events are most commonly observed at $\sim 20\text{--}50R_E$ but have been observed to occur as close as $\sim 10R_E$. Because of the limitations of *in situ* measurements by a small number of satellites, the characteristic length scales of diffusion regions in the magnetotail are difficult to constrain. However, fully kinetic simulations show the development of multiscale structures in and around the diffusion region during collisionless reconnection (e.g., Karimabadi et al. 2007; Shay et al. 2007). An inner diffusion region with a characteristic length scale of $\sim 10c/\omega_{pi}$ is seen in conjunction with an elongated electron outflow layer with a characteristic length scale of $\sim 50c/\omega_{pi}$ in these simulations. Recent satellite measurements of reconnection in the solar wind (e.g., Phan et al. 2006, 2007, 2009; Gosling et al. 2007; Lavraud et al. 2009) and in the Earth's magnetotail (e.g., Chen et al. 2008, 2009) support the picture of extended diffusion regions in natural systems, although it is possible that there is a selection effect that large-scale events are able to be observed more easily with currently available satellites. The ion inertial length in the magnetotail is generally of order $50\text{--}10^3$ km, depending on the density. Taking into account these uncertainties, I estimate a characteristic length scale for a reconnection layer in the near-Earth magnetotail to be between $10^8\text{--}10^9$ cm ($10^3\text{--}10^4$ km). The plasma pressure distribution of the magnetotail is estimated using the

equation (22) from the work by Zaharia et al. (2005), which represents the plasma pressure for a characteristic disturbed-time equilibrium (see also Zaharia et al. 2003a, 2003b; Wing et al. 2007). Using this model, Figure 3.8 shows the ratio of the plasma pressure at the tailward side of a reconnection layer of length L (either 10^8 cm or 10^9 cm) divided by the plasma pressure at the earthward side. The results show that if extended diffusion regions are prevalent in the magnetotail, then it is likely that effects associated with asymmetric downstream pressure are important at even large distances from Earth. On the other hand, if reconnection layers are short, then the downstream pressure will not be very asymmetric due to the large-scale equilibrium. Even so, the ability of the magnetospheric configuration to confine downstream plasma might lead to asymmetric downstream pressure even for short diffusion regions. However, collisionless effects and time-dependent behavior such as current sheet motion are also important in the magnetotail.

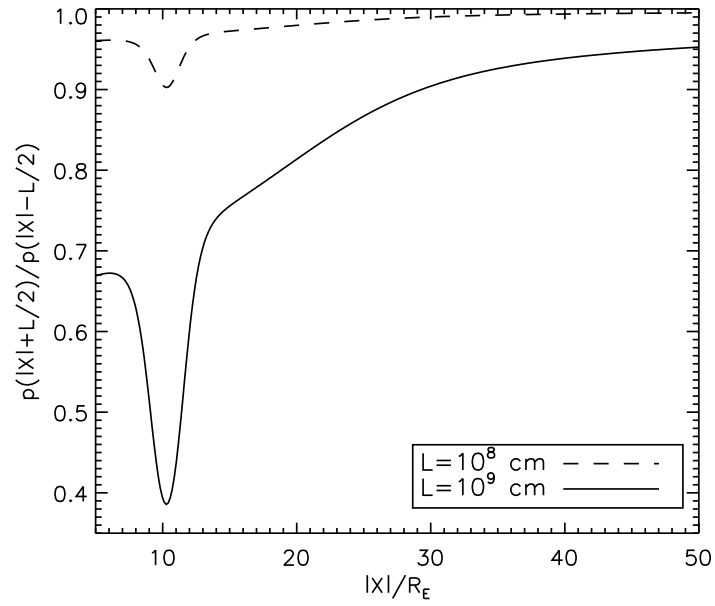


Fig. 3.8.—: The ratio of the plasma pressure at a tailward distance of $X + L/2$ divided by the plasma pressure at a tailward distance of $X - L/2$ as a function of distance from Earth in the tailward direction for two possible characteristic lengths of a reconnection layer. The plasma pressure is calculated from equation (22) from the work of Zaharia et al. (2005).

Table 3.2. Application of linear geometry model to flux cancellation events

Parameter (units)	Value
p_{lower} (dyne cm ⁻²)	1500
p_{in} (dyne cm ⁻²)	1000
p_{upper} (dyne cm ⁻²)	700
n (cm ⁻³)	5×10^{15}
B_{in} (G)	200
η/μ_0 (m ² s ⁻¹)	2×10^4
γ	1.2
V_{lower} (km s ⁻¹ , predicted)	7.7
V_{upper} (km s ⁻¹ , predicted)	8.3
V_{in} (km s ⁻¹ , predicted)	5.7×10^{-2}
δ (km, predicted)	0.35

References

- Baty, H., Forbes, T. G., & Priest, E. R. 2009, *Phys. Plasmas*, 16, 012102
- Birn, J., & Hesse, M. 2009, *Annales Geophysicae*, 27, 1067
- Birn, J., & Hesse, M., & Schindler, K. 1996, *J. Geophys. Res.*, 101, 12939
- Birn, J., Borovsky, J. E., & Hesse, M. 2008, *Phys. Plasmas*, 15, 032101
- Borovsky, J. E., & Hesse, M. 2007, *Phys. Plasmas*, 14, 102309
- Borovsky, J. E., Hesse, M., Birn, J., & Kuznetsova, M. M. 2008, *J. Geophys. Res.*, 113, A07210
- Brown, M. R., Cothran, C. D., & Fung, J. 2006, *Phys. Plasmas*, 13, 056503
- Cardano, G. 1545, *Artis Magnæ, Sive de Regulis Algebraicis Liber Unus*
- Cassak, P. A., & Shay, M. A. 2007, *Phys. Plasmas*, 14, 102114
- Cassak, P. A., & Shay, M. A. 2008, *Geophys. Res. Lett.*, 35, 19102
- Cassak, P. A., & Shay, M. A. 2009, *Phys. Plasmas*, 16, 055704
- Cassinelli, J. P., Brown, J. C., Maheswaran, M., Miller, N. A., & Telfer, D. C. 2002, *ApJ*, 578, 951
- Chae, J., Moon, Y.-J., & Park, S.-Y. 2003, *Journal of the Korean Astronomical Society*, 36, 13
- Chae, J., Moon, Y.-J., & Pevtsov, A. A. 2004, *ApJ*, 602, L65
- Chen, L.-J., Bessho, N., Lefebvre, B., Vaith, H., Fazakerley, A., Bhattacharjee, A., Puhl-Quinn, P. A., Runov, A., Khotyaintsev, Y., Vaivads, A., Georgescu, E., & Torbert, R. 2008, *J. Geophys. Res.*, 113, A12213

- Chen, L.-J., Bessho, N., Lefebvre, B., Vaith, H., Asnes, A., Santolik, O., Fazakerley, A., Puhl-Quinn, P., Bhattacharjee, A., Khotyaintsev, Y., Daly, P., & Torbert, R. 2009, *Phys. Plasmas*, 16, 056501
- Cothran, C. D., Falk, A., Fefferman, A., Landreman, M., Brown, M. R., & Schaffer, M. J. 2003, *Phys. Plasmas*, 10, 1748
- Drake, J. F., Swisdak, M., Che, H., & Shay, M. A. 2006, *Nature*, 443, 553
- Eriksson, S., Gosling, J. T., Phan, T. D., Blush, L. M., Simunac, K. D. C., Krauss-Varban, D., Szabo, A., Luhmann, J. G., Russell, C. T., Galvin, A. B., & Acuña, M. H. 2009, *J. Geophys. Res.*, 114, A07103
- Galsgaard, K., & Rousev, I. 2002, *A&A*, 383, 685
- Gary, G. A. 2001, *Sol. Phys.*, 203, 71
- Goedbloed, J. P., & Poedts, S. 2004, *Principles of Magnetohydrodynamics* (Cambridge, UK: Cambridge University Press)
- Gosling, J. T., Eriksson, S., Blush, L. M., Phan, T. D., Luhmann, J. G., McComas, D. J., Skoug, R. M., Acuna, M. H., Russell, C. T., & Simunac, K. D. 2007, *Geophys. Res. Lett.*, 34, L20108
- Groote, D., & Schmitt, J. H. M. M. 2004, *A&A*, 418, 235
- Hesse, M., & Schindler, K. 2001, *Earth Planets Space*, 53, 645
- Hooper, E. B., Kopriva, T. A., Cohen, B. I., Hill, D. N., McLean, H. S., Wood, R. D., Woodruff, S., & Sovinec, C. R. 2005, *Phys. Plasmas*, 12, 092503
- Huang, Y.-M., & Zweibel, E. G. 2009, *Phys. Plasmas*, 16, 042102
- Innes, D. E., Inhester, B., Axford, W. I., & Willhelm, K. 1997, *Nature*, 386, 811

- Inomoto, M., Gerhardt, S. P., Yamada, M., Ji, H., Belova, E., Kuritsyn, A., & Ren, Y. 2006, *Phys. Rev. Lett.*, 97, 135002
- Karimabadi, H., Krauss-Varban, D., Omid, N., & Vu, H. X. 1999, *J. Geophys. Res.*, 104, 12313
- Karimabadi, H., Daughton, W., & Scudder, J. 2007, *Geophys. Res. Lett.*, 34, 13104
- Kiehas, S., Semenov, V. S., Kubyshkina, M., Angelopoulos, V., Nakamura, R., Keika, K., Ivanova, I., Biernat, H. K., Baumjohann, W., Mende, S. B., Magnes, W., Auster, U., Fornacon, K.-H., Larson, D., Carlson, C. W., Bonnell, J., & McFadden, J. 2009, *J. Geophys. Res.*, 114, A00C20
- Kiehas, S. A., Semenov, V. S., Kubyshkin, I. V., Tolstykh, Y. V., Penz, T., & Biernat, H. K. 2007, *Annales Geophysicae*, 25, 293
- Kivelson, M. G., & Southwood, D. J. 2005, *J. Geophys. Res.*, 110, A12209
- Kopp, R. A., & Pneuman, G. W. 1976, *Sol. Phys.*, 50, 85
- Kuznetsova, M. M., Hesse, M., Rastätter, L., Taktakishvili, A., Toth, G., De Zeeuw, D. L., Ridley, A., & Gombosi, T. I. 2007, *J. Geophys. Res.*, 112, 10210
- La Belle-Hamer, A. L., Otto, A., & Lee, L. C. 1995, *J. Geophys. Res.*, 100, 11875
- Laitinen, T. V. 2007, Ph.D. thesis, Finnish Meteorological Institute
- Laitinen, T. V., Pulkkinen, T. I., Palmroth, M., Janhunen, P., & Koskinen, H. E. J. 2005, *Annales Geophysicae*, 23, 3753
- Laitinen, T. V., Nakamura, R., Runov, A., Rème, H., & Lucek, E. A. 2007, *Annales Geophysicae*, 25, 1025

- Lavraud, B., Gosling, J. T., Rouillard, A. P., Fedorov, A., Opitz, A., Sauvaud, J.-A., Foullon, C., Dandouras, I., Génot, V., Jacquy, C., Louarn, P., Mazelle, C., Penou, E., Phan, T. D., Larson, D. E., Luhmann, J. G., Schroeder, P., Skoug, R. M., Steinberg, J. T., & Russell, C. T. 2009, *Sol. Phys.*, 256, 379
- Lazarian, A., & Vishniac, E. T. 1999, *ApJ*, 517, 700
- Lee, L. C., & Fu, Z. F. 1986, *J. Geophys. Res.*, 91, 6807
- Lin, J., & Forbes, T. G. 2000, *J. Geophys. Res.*, 105, 2375
- Lin, Y., Wang, X. Y., Brown, M. R., Schaffer, M. J., & Cothran, C. D. 2008, *Plasma Phys. Controlled Fusion*, 50, 074012
- Litvinenko, Y. E. 1999, *ApJ*, 515, 435
- Litvinenko, Y. E., & Martin, S. F. 1999, *Sol. Phys.*, 190, 45
- Litvinenko, Y. E., & Chae, J. 2009, *A&A*, 495, 953
- Lui, A. T. Y., Spence, H. E., & Stern, D. P. 1994, *J. Geophys. Res.*, 99, 151
- Malyshkin, L. M., Linde, T., & Kulsrud, R. M. 2005, *Phys. Plasmas*, 12, 102902
- Martin, S. F., Livi, S. H. B., & Wang, J. 1985, *Australian Journal of Physics*, 38, 929
- Martin, S. F. 1990, in *Solar Photosphere: Structure, Convection, and Magnetic Fields*, IAU Symposium 138, ed. J. O. Stenflo (Dordrecht: Kluwer Academic Publishers), 129
- Mozer, F. S., & Pritchett, P. L. 2009, *Geophys. Res. Lett.*, 36, L07102
- Mozer, F. S., Angelopoulos, V., Bonnell, J., Glassmeier, K. H., & McFadden, J. P. 2008, *Geophys. Res. Lett.*, 35, L17S04

- Mukai, T., Nagai, T., Hoshino, M., Saito, Y., Shinohara, I., Yamamoto, T., & Kokubun, S. 2000, *Adv. Space Res.*, 25, 1679
- Nakajima, R. 1985, *Astrophys. Space Sci.*, 116, 285
- Nakamura, M., & Scholer, M. 2000, *J. Geophys. Res.*, 105, 23179
- Nishida, K., Shimizu, M., Shiota, D., Takasaki, H., Magara, T., & Shibata, K. 2009, *ApJ*, 690, 748
- Oka, M., Fujimoto, M., Nakamura, T. K. M., Shinohara, I., & Nishikawa, K. 2008, *Phys. Rev. Lett.*, 101, 205004
- Ono, Y., Morita, A., Katsurai, M., & Yamada, M. 1993, *Phys. Fluids B*, 5, 3691
- Owen, C. J., & Cowley, S. W. H. 1987a, *Planet. Space Sci.*, 35, 451
- Owen, C. J., & Cowley, S. W. H. 1987b, *Planet. Space Sci.*, 35, 467
- Parker, E. N. 1957, *J. Geophys. Res.*, 62, 509
- Parker, E. N. 1963, *ApJS*, 8, 177
- Petschek, H. E. 1964, in *AAS/NASA Symposium on the Physics of Solar Flares*, ed. W. N. Hess (Washington, D.C.: NASA), 425
- Phan, T. D., Gosling, J. T., Davis, M. S., Skoug, R. M., Øieroset, M., Lin, R. P., Lepping, R. P., McComas, D. J., Smith, C. W., Reme, H., & Balogh, A. 2006, *Nature*, 439, 175
- Phan, T. D., Drake, J. F., Shay, M. A., Mozer, F. S., & Eastwood, J. P. 2007, *Phys. Rev. Lett.*, 99, 255002
- Phan, T. D., Gosling, J. T., & Davis, M. S. 2009, *Geophys. Res. Lett.*, 36, L09108

- Priest, E., & Forbes, T. 2000, *Magnetic Reconnection: MHD Theory and Applications* (Cambridge, UK: Cambridge University Press)
- Pritchett, P. L. 2008, *J. Geophys. Res.*, 113, A06210
- Qui, J., & Yurchyshyn, V. B. 2005, *ApJL*, 634, L121
- Reeves, K. K. 2006, *ApJ*, 644, 592
- Rogers, B., & Zakharov, L. 1995, *Phys. Plasmas*, 2, 3420
- Roussev, I., Galsgaard, K., Erdélyi, R., & Doyle, J. G. 2001, *A&A*, 370, 298
- Sergeev, V., Kubyshkina, M., Alexeev, I., Fazakerley, A., Owen, C., Baumjohann, W., Nakamura, R., Runov, A., Vörös, Z., Zhang, T. L., Angelopoulos, V., Sauvaud, J.-A., Daly, P., Cao, J. B., & Lucek, E. 2008, *J. Geophys. Res.*, 113, A07S36
- Servidio, S., Matthaeus, W. H., Shay, M. A., Cassak, P. A., & Dmitruk, P. 2009, *Phys. Rev. Lett.*, 102, 115003
- Shay, M. A., Drake, J. F., & Swisdak, M. 2007, *Phys. Rev. Lett.*, 99, 155002
- Shibata, K., Masuda, S., Shimojo, M., Hara, H., Yokoyama, T., Tsuneta, S., Kosuji, T., & Ogawara, Y. 1995, *ApJL*, 451, L83
- Shimizu, M., Nishida, K., Takasaki, H., Shiota, D., Magara, T., & Shibata, K. 2008, *ApJL*, 683, L203
- Shiohara, K., Baumjohann, W., & Haerendel, G. 1997, *Geophys. Res. Lett.*, 24, 1179
- Sovinec, C. R., Glasser, A. H., Gianakon, T. A., Barnes, D. C., Nebel, R. A., Kruger, S. E., Schnack, D. D., Plimpton, S. J., Tarditi, A., & Chu, M. S. 2004, *J. Comp. Phys.*, 195, 355

- Sweet, P. A. 1958, in IAU Symp. 6, *Electromagnetic Phenomena in Cosmical Physics*, ed. B. Lehnert (Dordrecht: Kluwer) 123
- Swisdak, M., Rogers, B. N., Drake, J. F., & Shay, M. A. 2003, *J. Geophys. Res.*, 108, 23
- Townsend, R. H. D., & Owocki, S. P. 2005, *MNRAS*, 357, 251
- ud-Doula, A., Townsend, R. H. D., & Owocki, S. P. 2006, *ApJL*, 640, L191
- ud-Doula, A., Owocki, S. P., & Townsend, R. H. D. 2008, *MNRAS*, 385, 97
- Wing, S., Gjerloev, J. W., Johnson, J. R., & Hoffman, R. A. 2007, *Geophys. Res. Lett.*, 34, L16110
- Zaharia, S., & Cheng, C. Z. 2003a, *Geophys. Res. Lett.*, 30, 1883
- Zaharia, S., & Cheng, C. Z. 2003b, *J. Geophys. Res.*, 108, 1412
- Zaharia, S., Birn, J., & Cheng, C. Z. 2005, *J. Geophys. Res.*, 110, A09228

Chapter 4

Conclusions

4.1 Summary and Conclusions

This thesis contains an investigation of the interplay between local and global effects during the process of magnetic reconnection. Chapter 2 reports on simulations of two-fluid reconnection that fully incorporate the Hall term in the generalized Ohm's law while using the geometry of an actual reconnection experiment. Both the push and pull modes of the Magnetic Reconnection Experiment (MRX) are simulated with and without two-fluid effects to investigate the impact of global effects on the reconnection process (see Figure 2.2 for illustrations of MRX's push and pull modes of operation). The two-fluid model used in these simulations includes resistivity, the Hall term, and a scalar electron pressure gradient in the generalized Ohm's law, but not electron inertia. A uniform resistivity is used in the reconnection region, thus ignoring effects associated with anomalous resistivity.

In all of the simulations reported in Chapter 2, pressure effects are found to be an important intermediary between small and large scales. Asymmetries in the inflow and outflow directions feed back on the reconnection process through large scale pressure gradients. During pull reconnection, the inboard side of the current sheet is depleted of density more quickly than the outboard side due to the small volume available on the inboard side. Consequently, the current sheet displays a radially inward motion after reconnection commences which stops when magnetic pressure becomes large enough to counterbalance the plasma pressure gradient. This radial motion is seen also in experiment (e.g., Dorfman et al. 2006). A similar effect occurs during push reconnection. Whereas the upstream regions are asymmetric during pull reconnection, the downstream regions are asymmetric during push reconnection. A significant pressure buildup occurs on the inboard side of the current sheet.

While such a pressure buildup would normally be expected to strongly suppress radially inward directed outflow, the X-point position is shifted to the outboard side of the current sheet. This strengthens the magnetic tension on the inboard side of the current sheet, thus allowing strong radially inward directed outflow to be maintained.

Two-fluid simulations of pull reconnection show good agreement with the structure and magnitude of the out-of-plane quadrupole magnetic field which develops as the electron flow associated with the reconnection current pulls in-plane magnetic field lines in the out-of-plane direction. In both simulation and experiment, the outboard quadrupole lobes peak in strength closer to the X-point than the inboard quadrupole lobes. This effect is related to geometry in that the ion inertial length is longer on the inboard side than the outboard side due to the lower density.

A comparison of the reconnection rates for resistive MHD and two-fluid push and pull reconnection shows that in these simulations, geometry plays a more substantial role in determining the reconnection rate than the inclusion of the Hall term. For a given mode of operation, the inclusion of the Hall term increases the reconnection rate by $\sim 25\%$, but for a given physical model, push reconnection is $\sim 50\%$ quicker than pull reconnection. The difference is attributed to the importance of downstream pressure and the limited flux available to reconnect during the pull mode of operation. During push reconnection, the reconnection rate plateaus at a value slightly over the electric field strength that would exist in the absence of plasma, indicating that for this case reconnection is occurring as quickly as it is driven. Pull reconnection, however, is limited by flux availability and is eventually quenched by downstream pressure.

Comparing the electron outflow velocity profiles between simulation and experiment shows a discrepancy in the location of the peak electron outflow. While in experiment

the peak electron outflow velocity occurs near $Z \approx 6$ cm, the peak electron outflow in simulation occurs within 1–2 cm of the X-point. We interpret the simulation results as a direct consequence of Hall physics controlling the nature of the diffusion region. Thus, the standard picture of Hall reconnection is inadequate in describing the small-scale physics present in the experimental current sheet. The relative elongation of the electron layer in MRX could be related to kinetic effects reported in Daughton et al. (2006), Fujimoto (2006), Karimabadi et al. (2007), Shay et al. (2007), and Phan et al. (2006, 2007, 2009).

In addition to the effects associated with null-helicity merging described above, there are additional two-fluid effects which manifest themselves during co-helicity and counter-helicity push reconnection. When a guide field is present during co-helicity merging, the electrons in the outflow region experience a Lorentz force in the Z direction. The electrons carry the magnetic field, resulting in a tilt of the current sheet. The ion flow is also affected, resulting in an asymmetric pressure distribution due to the Z component of the ion outflow. During simulations that use cylindrical geometry, the current sheet position is shifted from $Z = 0$.

The simulations of two-fluid counter-helicity push reconnection using linear geometry allow investigation of the development of asymmetric outflow that is associated with the radial shift in position of the X-point seen by Inomoto et al. (2006). On the side to which the X-point is shifted, the dominant force is magnetic pressure, which is important due to both the compression of B_Z and to the simple fact that the radial shift in position of the X-point means that the strong vertical magnetic field is closer. On the side from which the X-point is shifted, forces associated with magnetic and plasma pressure are small, while the force due to magnetic tension is large. The consequences are that outflow on the side to which the X-point is shifted is suppressed, while outflow on the side from which the X-point is

shifted is enhanced. Additionally, diamagnetic drifts of ions and electrons above and below the current sheet help facilitate this asymmetric flow pattern. When cylindrical geometry is used, symmetry breaking due to volume effects acts to push the X-point outward and increase pressure on the inboard side of the current sheet, as in null-helicity cases. Hence, depending on the orientation of B_ϕ or sign of B_ϕ relative to the toroidal direction above and below the current sheet, the Hall symmetry breaking can work with symmetry breaking due to the cylindrical geometry, or against it.

Push reconnection in MRX is asymmetric because the outflow direction is aligned with the radial direction. Asymmetry in the outflow direction is not unique to the laboratory; in fact, similar events occur in planetary magnetotails, coronal mass ejections, flux cancellation events, astrophysical disks, and magnetized turbulence. Chapter 3 uses control volume analyses to address the scaling of steady reconnection with asymmetry in the outflow direction for both linear and cylindrical geometry.

A set of scaling relations describing steady magnetic reconnection with asymmetric outflow and downstream pressure for linear geometry is presented in Section 3.3. The scaling relations arising from conservation of mass, momentum, and energy were derived for a long and thin current sheet without explicitly specifying the dissipation mechanism that breaks magnetic field lines. These relations are then used to derive a cubic equation in the square of the outflow velocity from one side, which can be solved numerically or by using Cardano's method. This cubic polynomial reduces to a quadratic polynomial for both the incompressible case and the case with symmetric downstream pressure but asymmetric downstream density. When resistive dissipation is assumed, we present an expression for the reconnection rate that depends on the outflow velocities from both sides of the current sheet.

In the presence of asymmetric downstream pressure, it is possible to have one Alfvénic jet and one sub-Alfvénic jet rather than two bi-directional Alfvénic jets. Moreover, the reconnection rate is not greatly affected when outflow from only one side is blocked because the thickness of the current sheet is allowed to increase to avoid a bottleneck. The reconnection rate is greatly reduced only when outflow from both sides of the current sheet is blocked. This helps explain results by Oka et al. (2008), who find that the presence of an obstacle on one downstream side of the current sheet does not greatly impact the reconnection rate.

In a steady state, the magnetic field null and flow stagnation point overlap only in the absence of pressure gradient forces at the magnetic field null. Otherwise, the magnetic field null is located on the side of the flow stagnation point which allows magnetic tension to counter the non-electromagnetic forces at the flow stagnation point. The position of the flow stagnation point can be estimated using conservation of mass, and the position of the magnetic field null can be estimated using a Taylor expansion around the flow stagnation point. When there is a separation between the two points, there will be a Poynting flux across the flow stagnation point and a kinetic energy flux across the magnetic field null.

Section 3.4 addresses the problem of reconnection in cylindrical geometry with the outflow aligned with the radial direction. This setup is appropriate for reconnection in some astrophysical disks (e.g., ud-Doula et al. 2006) as well as spheromak merging in the laboratory. As for the linear geometry case, scaling relations approximating conservation of mass, momentum, and energy are derived for a long and thin current sheet without explicitly specifying the dissipation mechanism. The model assumes an upstream magnetic field profile that is proportional to $1/R$, but the analysis can be modified to account for different upstream magnetic field profiles. Unlike the linear geometry model, these relations must be solved numerically. It is possible to have quicker radially inward-directed outflow

than radially outward-directed outflow even when the inboard pressure exceeds the outboard pressure. These results can assist in the interpretation of bi-directional reconnection outflow jets that have been observed during spheromak merging experiments such as SSX (e.g., Brown et al. 2006). These scaling relations may also be testable in present experimental devices such as SSX, MRX, and TS-3/4.

In Section 3.3.4, resistive MHD simulations using the NIMROD code are performed for both linear and cylindrical geometry. The first test uses the driving mechanism and geometry of MRX in linear geometry with one downstream wall closer to the current sheet than the other. The advantage of using this setup is that the position of the current sheet is constrained between the flux cores. Data extracted from this test show good correspondence between the left and right hand sides of the scaling relations approximating conservation of mass, momentum, and energy. The second test incorporates the geometry and driving mechanism of MRX in cylindrical geometry, finding agreement in the scaling relations to within a factor of ~ 2 . Future numerical, experimental, and observational tests in different geometries will benefit our understanding of reconnection with asymmetry in the outflow direction.

The scaling relations described in Chapter 3 rely on a number of assumptions. Most importantly, the derivations assume a steady state and that profiles have attained their asymptotic distributions. Refinements or alternatives to the analysis presented in Chapter 3 would benefit from the inclusion of time-dependent effects. Of particular interest would be determining what sets the velocity of X-line retreat as observed by Oka et al. (2008). The analysis assumes that the reconnection magnetic field lines are antiparallel and thus neglects the possibility of a guide magnetic field. Three-dimensional effects, which could enhance the ability of plasma to exit the current sheet (e.g., Lazarian & Vishniac 1999; Sullivan &

Rogers 2008), are ignored. Energy losses through thermal conduction, energetic particles, and radiation are not considered. The scaling relations also assume that the current sheet is long and thin so that the kinetic energy flux into the sheet and the Poynting flux out of the sheet are small and that contributions from tension along the boundary of the control volume can be ignored.

4.2 Astrophysical Significance of Results

Our understanding of the physics of magnetic reconnection comes primarily from three areas: solar physics, space physics, and laboratory plasma physics. Direct or *in situ* measurements of reconnection are possible only in the latter two areas. Reconnection is invoked in many astrophysical situations, but outside of the solar system this physical process is too small-scale to be observed. Consequently, astrophysicists must draw upon knowledge from these related fields using simulation, theory, and observations together in order to have a chance of accurately describing magnetic reconnection elsewhere in the universe.

The simulations in Chapter 2 show how outflow from a reconnection event can modify the global equilibrium only to have the global equilibrium feed back on the reconnection process. How much the reconnection process is affected by downstream pressure depends on the ability of the downstream magnetic field configuration to confine reconnection exhaust. In the solar atmosphere, flux ropes below a reconnection layer can impede downward-directed outflow in much the same manner as outflow is impeded during push reconnection in MRX. High magnetic pressure near Earth can lead to similar consequences during magnetotail reconnection. Geometric effects are found to play an important role in reconnection and can even be more important at determining the reconnection rate than the inclusion of two-fluid effects. How strongly reconnection is driven, and in what way it is driven, help to determine

the length and thickness of a reconnection layer and the reconnection rate. These geometric results, including the observation that the reconnection layer can self-adjust so that reconnection is able to occur as quickly as it is driven, will have significant consequences if they can be extrapolated to high Lundquist number plasmas in the solar corona. For low density plasmas in the solar wind and magnetosphere, the Hall effect can lead to asymmetry in the reconnection process, especially in conjunction with other geometric effects.

Hall physics in a plasma becomes important when the electrons can move with the magnetic field but the ions cannot. In the context of reconnection in a fully ionized plasma, this occurs when the ion inertial length, c/ω_{pi} , is comparable to or greater than the characteristic length scales of a diffusion layer. MRX is in such a regime, as are reconnection events in the Earth's magnetosphere and the solar wind. However, in a partially ionized plasma, decoupling between ions and electrons will also occur due to ion-neutral collisions. In such plasmas, the length scale where decoupling becomes important is enhanced by a factor of $\sqrt{\rho/\rho_i}$ over the ion inertial length (e.g., Pandey & Wardle 2008). Thus, two-fluid effects similar to those included in simulations of MRX may have important consequences for reconnection events in weakly or partially ionized plasmas such as protoplanetary disks.

Whenever reconnection occurs in a realistic situation, there will be some degree of asymmetry. Asymmetry in the outflow direction occurs most notably in coronal mass ejections, solar flares, photospheric flux cancellation events, planetary magnetotails, astrophysical disks, and laboratory spheromak merging experiments. The models developed in Chapter 3 address the problem of steady reconnection with asymmetric outflow and downstream pressure. Importantly, this work addresses the problems of where energy goes during asymmetric reconnection, how the reconnection rate is affected, and what the speeds of each outflow jet are. The cylindrical geometry model is applicable to astrophysical disks

in addition to spheromak merging experiments.

Effects associated with asymmetric downstream pressure are likely to be important for reconnection events in a stratified medium where the pressure gradient length scale is comparable to the length of the reconnection layer. Section 3.5 shows that this criterion should be satisfied for reconnection events in the solar photosphere and Earth's magnetotail. Critically, however, this criterion depends on the length of the diffusion layer (e.g., Daughton et al. 2006; Fujimoto 2006; Shay et al. 2007; Karimabadi et al. 2007; Ren et al. 2008; Dorfman et al. 2008; Phan et al. 2006, 2007, 2009; Gosling et al. 2007; Chen et al. 2008, 2009; Lavraud et al. 2009; Uzdensky 2009; Sullivan & Bhattacharjee 2009; see also Chapter 2) and neglects the ability of reconnection to influence its downstream pressure. In particular, asymmetric downstream pressure is likely to occur if one outflow jet is impeded or confined by the downstream magnetic field while the other jet is not obstructed. If this occurs, the length of the diffusion region should be of less direct concern.

Both the simulations in Chapter 2 and the model in Chapter 3 shed light on the observational signatures of magnetic reconnection in space physics and astrophysics. In particular, the density, temperature, and velocity structures seen in simulations of MRX can be used in conjunction with observations of the solar atmosphere to gauge the importance of coupling between small and large scales and asymmetry during the reconnection process. The relative speeds of bi-directional jets for reconnection with asymmetry in the outflow direction are predicted by the model developed in Chapter 3 for time-independent reconnection in a long and thin current sheet. The propagation of bi-directional asymmetric jets can be used as a probe of the plasma pressure and density of a medium if their properties are well-understood (see, for example, Freeland et al. 2008).

4.3 Future Work

The simulations reported in Chapter 2 were performed to investigate the coupling between small and large scales during magnetic reconnection. MRX was chosen as a basis for these simulations because of its moderate scale separation in addition to the availability of experimental data to compare against simulations. In the coming years, increases in computing power combined with algorithm improvement will allow multiscale simulations with greater separation of scales as well as more complete physics on smaller scales. Such simulations, when validated against observational and experimental data, will provide additional insight into how magnetic reconnection behaves in astrophysical settings where scale separation is extreme.

The inability of the two-fluid model used in Chapter 2 to reproduce the experimentally observed electron outflow velocity profile shows that additional physics needs to be included in models describing collisionless reconnection. PIC simulations by Dorfman et al. (2008) are able to reproduce the observed electron outflow velocity profile but not the thickness of the diffusion region. An effort is underway to add collisions to their code so that resistive effects can be represented. Nevertheless, the fundamental question of what sets the aspect ratio of the diffusion region during collisionless reconnection remains unanswered. Until this is understood, we will not be able to fully understand what conditions are needed in order for reconnection to be fast.

Two conclusions from Chapter 2 are that (1) reconnection is asymmetric due to cylindrical geometry effects, and (2) effects associated with downstream pressure play a significant role in slowing down the outflow. Because of the importance of downstream pressure, a straightforward application to pull reconnection of the model developed by Cassak &

Shay (2007) is not possible. To apply their results to MRX, it will be necessary to repeat their analysis without dropping the terms associated with upstream and downstream plasma pressure.

The scaling relations derived in Chapter 3 assume that time-dependent effects are negligible and that the current sheet is approximately static in an appropriate inertial reference frame. However, in many situations in nature and the laboratory, reconnection is bursty and there is considerable current sheet motion. Moreover, downstream pressure is not expected to remain constant over time; rather, downstream pressure depends on both the history of the reconnection event and the nature of the global magnetic field configuration. Incorporating time-dependent effects into the picture developed in Chapter 3 will be an important next step.

The models presented in Chapter 3 would benefit from being applied to situations in nature and the laboratory where reconnection with asymmetry in the outflow direction occurs. Such situations include reconnection in the Earth's magnetotail, coronal mass ejections, solar flares, flux cancellation events, astrophysical disks, and spheromak merging experiments. These applications will test the assumptions made in Chapter 3 and will gauge the importance of time-dependent effects. For the magnetotail, consequences of this model involving uneven energy transport in the earthward and tailward directions should be considered in more detail because of the implications regarding magnetic substorms. This model should also be reconsidered in the contexts of collisionless reconnection, during which the aspect ratio of the diffusion region can become modest, and reconnection with a guide field.

References

- Brown, M. R., Cothran, C. D., & Fung, J. 2006, *Phys. Plasmas*, 13, 056503
- Cassak, P. A., & Shay, M. A. 2007, *Phys. Plasmas*, 14, 102114
- Chen, L.-J., Bessho, N., Lefebvre, B., Vaith, H., Fazakerley, A., Bhattacharjee, A., Puhl-Quinn, P. A., Runov, A., Khotyaintsev, Y., Vaivads, A., Georgescu, E., & Torbert, R. 2008, *J. Geophys. Res.*, 113, A12213
- Chen, L.-J., Bessho, N., Lefebvre, B., Vaith, H., Asnes, A., Santolik, O., Fazakerley, A., Puhl-Quinn, P., Bhattacharjee, A., Khotyaintsev, Y., Daly, P., & Torbert, R. 2009, *Phys. Plasmas*, 16, 056501
- Daughton, W., Scudder, J., & Karimabadi, H. 2006, *Phys. Plasmas*, 13, 072101
- Dorfman, S., Ji, H., Yamada, M., Ren, Y., Gerhardt, S. P., Kulsrud, R. M., McGeehan, B., & Wang, Y. 2006, *AIP Conf. Proc.*, 871, 306
- Dorfman, S., Daughton, W., Roytershteyn, V., Ji, H., Ren, Y., & Yamada, M. 2008, *Phys. Plasmas*, 15, 102107
- Freeland, E., Cardoso, R. F., & Wilcots, E. 2008, *ApJ*, 685, 858
- Fujimoto, K. 2006, *Phys. Plasmas*, 13, 072904
- Gosling, J. T., Eriksson, S., Blush, L. M., Phan, T. D., Luhmann, J. G., McComas, D. J., Skoug, R. M., Acuna, M. H., Russell, C. T., & Simunac, K. D. 2007, *Geophys. Res. Lett.*, 34, L20108
- Inomoto, M., Gerhardt, S. P., Yamada, M., Ji, H., Belova, E., Kuritsyn, A., & Ren, Y. 2006, *Phys. Rev. Lett.*, 97, 135002
- Karimabadi, H., Daughton, W., & Scudder, J. 2007, *Geophys. Res. Lett.*, 34, 13104

- Lavraud, B., Gosling, J. T., Rouillard, A. P., Fedorov, A., Opitz, A., Sauvaud, J.-A., Foullon, C., Dandouras, I., Génot, V., Jacquy, C., Louarn, P., Mazelle, C., Penou, E., Phan, T. D., Larson, D. E., Luhmann, J. G., Schroeder, P., Skoug, R. M., Steinberg, J. T., & Russell, C. T. 2009, *Sol. Phys.*, 256, 379
- Lazarian, A., & Vishniac, E. T. 1999, *ApJ*, 517, 700
- Oka, M., Fujimoto, M., Nakamura, T. K. M., Shinohara, I., & Nishikawa, K. 2008, *Phys. Rev. Lett.*, 101, 205004
- Pandey, B. P., & Wardle, M. 2009, *MNRAS*, 385, 2269
- Phan, T. D., Gosling, J. T., Davis, M. S., Skoug, R. M., Øieroset, M., Lin, R. P., Lepping, R. P., McComas, D. J., Smith, C. W., Reme, H., & Balogh, A. 2006, *Nature*, 439, 175
- Phan, T. D., Drake, J. F., Shay, M. A., Mozer, F. S., & Eastwood, J. P. 2007, *Phys. Rev. Lett.*, 99, 255002
- Phan, T. D., Gosling, J. T., & Davis, M. S. 2009, *Geophys. Res. Lett.*, 36, L09108
- Ren, Y., Yamada, M., Ji, H., Dorfman, S., Gerhardt, S., & Kulsrud, R. 2008, *Phys. Plasmas*, 15, 082113
- Shay, M. A., Drake, J. F., & Swisdak, M. 2007, *Phys. Rev. Lett.*, 99, 155002
- Sullivan, B. P., & Rogers, B. N. 2008, *Phys. Plasmas*, 15, 102106
- Sullivan, B. P., & Bhattacharjee, A. 2009, *Phys. Plasmas*, submitted
- ud-Doula, A., Townsend, R. H. D., & Owocki, S. P. 2006, *ApJL*, 640, L191
- Uzdensky, D. 2009, *Phys. Plasmas*, 16, 040702

Appendix A

Technical Modifications to NIMROD

A.1 Introduction

The procedure for defining a logically rectangular grid in NIMROD is well-established. However, there are some applications for which a logically rectangular grid is not practical. The two goals of this appendix are to detail changes made to NIMROD for application to MRX (see Chapter 2) and to provide a guide for future researchers who wish to establish logically non-rectangular grids such as the one shown in Figure 2.1. This appendix should be used in combination with the tutorial by Sovinec (2001). Some familiarity with the code is assumed. All code presented in this appendix is written in the NIMROD dialect of Fortran 90.

Before proceeding, it is worth commenting on the advantages and disadvantages of using a logically non-rectangular grid in NIMROD. The primary advantage is geometric flexibility. In particular, some computational domains cannot reasonably be mapped onto a logically rectangular grid. Moreover, the use of a logically rectangular grid sometimes requires high resolution in regions where it is not needed (e.g., the gun region of a driven spheromak experiment), which can increase computational time. A logically non-rectangular grid can allow greater control of mesh packing than a logically rectangular grid under most circumstances. The primary disadvantages of a logically non-rectangular grid are the time commitment required to implement the grid, the complexity, and the increased difficulty in postprocessing. The most time-consuming part of establishing a logically non-rectangular grid is implementing connectivity information. With regards to postprocessing, several options in `nimplot` are not presently implemented for a logically non-rectangular grid (e.g., the toroidally averaged poloidal flux diagnostic). However, the vector and contour options

can still be used. Because of the time needed to manually implement connectivity between grid blocks, a logically non-rectangular grid should only be used when a logically rectangular grid cannot reasonably be implemented.

A.2 Establishment of a Logically Non-Rectangular Grid

The finite element grid used for NIMROD simulations of MRX is composed of twenty connected logically rectangular blocks of quadrilateral finite elements (known as `rblocks`). Although these `rblocks` individually are logically rectangular, the grid as a whole is not due to the presence of two flux cores that must each be surrounded completely by the computational domain (Figure 2.2; see also Yamada et al. 1997). Consequently, extensive modification of the preprocessing software for NIMROD is needed to incorporate the geometry and initial conditions for simulations of MRX.

Preprocessing in NIMROD is done by the program `nimset`. For a logically rectangular grid, the position information for each finite element is specified within the `lxy` data structure before being ultimately decomposed into separate `rblocks` and stored within the `rb` data structure. The node positions of each element are defined by arrays contained within each of these structures. As described by Sovinec (2001, p. 40), `lxy%fs(iv,ix,iy)` contains the corner vertex positions, `lxy%fsh(iv,ib,ix,iy)` contains the horizontal side node positions, `lxy%fsv(iv,ib,ix,iy)` contains vertical side node positions, and `lxy%fsi(iv,ib,ix,iy)` contains the interior node positions. The indices `ix` and `iy` refer to the logical indices of the element within the rectangular grid, the index `iv` refers to the direction vector ($R, x \rightarrow iv=1$; $Z, y \rightarrow iv=2$; and for 3D vector fields: $\phi, z \rightarrow iv=3$ for cylindrical and linear geometry), and `ib` corresponds to the internal block node ordering.

The following loop, placed within the `rect_init` subroutine contained in the file

`nimset_init.f`, will specify the vertex positions within `lxy` from the two-dimensional arrays `xx` and `yy`.

```

DO jx=0,mx
  DO jy=0,my
    lxy%fs(1,jx,jy)=xx(jx,jy)
    lxy%fs(2,jx,jy)=yy(jx,jy)
  ENDDO
ENDDO

```

When higher order basis functions are being used, the following loop from `rect_init` specifies the interior node positions.

```

IF (poly_degree>1) THEN
  DO ibasis=2,SIZE(lxy%ix0)
    dx=lxy%dx(ibasis)
    dy=lxy%dy(ibasis)
    DO iy=lxy%iy0(ibasis),lxy%my
      iym=MAX(iy-1,0_i4)
      IF (dy==0) iym=iy
      DO ix=lxy%ix0(ibasis),lxy%mx
        ixm=MAX(ix-1,0_i4)
        IF (dx==0) ixm=ix
        xxyy=(1-dy)*((1-dx)*lxy%fs(:,ixm,iym)+dx*lxy%fs(:,ix,iym))
$           +dy*((1-dx)*lxy%fs(:,ixm,iy )+dx*lxy%fs(:,ix,iy ))
        CALL lagr_quad_basis_assign_loc(lxy,xxyy,ibasis,ix,iy)
      ENDDO
    ENDDO
  ENDDO

```

```

                ENDDO
            ENDDO
        ENDDO
    ENDIF

```

To establish a logically non-rectangular grid, the position information is placed directly within the `rb` data structure instead of within `lxy`. The first step is to specify the number of `rblocks` that will be used in the grid.

```

    nrbl = 20  !number of rblocks
    ALLOCATE(rb(nrbl))

```

Next, put in the dimensions of each of the blocks, where, in the following example, `mx_block1` and `my_block1` are the numbers of elements within `rblock #1` in each direction.

```

    rb(1)%mx = mx_block1
    rb(1)%my = my_block1

```

For simulations run in parallel, it is useful to have the number of elements within each `rblock` be approximately constant so that the loads on each processor are balanced. For simulations run in serial, however, it is useful to allow for the possibility of `rblocks` with different numbers of elements. Next, make data allocations. The position information is located within the `rb(ibl)%rz` structure. The index `ibl` refers to the block number.

```

    DO ibl=1,nrbl  !loop over blocks
        CALL lagr_quad_alloc(rb(ibl)%rz,rb(ibl)%mx,rb(ibl)%my,2_i4,
$      poly_degree,name='lagrrz',title=(/' r ', ' z '/))
        rb(ibl)%rz%fs=0  !initializing all vertex positions to 0
    
```

```
ENDDO
```

The next step is to specify the location of the element vertices.

```

ibl=1
DO ix=0,rb(ibl)%mx
  DO iy=0,rb(ibl)%my
    rb(ibl)%rz%fs(1,ix,iy)= R_positions_block1(ix,iy)
    rb(ibl)%rz%fs(2,ix,iy)= Z_positions_block1(ix,iy)
  ENDDO
ENDDO

```

Then it is necessary to fill in the interior node positions. This step is usually done within lxy.

```

DO ibl=1,nrbl
  DO ibasis=2,SIZE(rb(ibl)%rz%ix0)
    dx=rb(ibl)%rz%dx(ibasis)
    dy=rb(ibl)%rz%dy(ibasis)
    IF (dx.LT.0.0.OR.dy.LT.0) THEN !check for distorted elements
      WRITE (*,*) 'ibl=',ibl, ' ibasis=',ibasis
      WRITE (*,*) 'dx=',dx,' dy=',dy
      CALL nim_stop('dx or dy < 0')
    ENDIF
    DO iy=rb(ibl)%rz%iy0(ibasis),rb(ibl)%my
      iym=MAX(iy-1,0_i4)
      IF (dy==0) iym=iy
    ENDDO
  ENDDO
ENDDO

```

```

DO ix=rb(ibl)%rz%ix0(ibasis),rb(ibl)%mx
  ixm=MAX(ix-1,0_i4)
  IF (dx==0) ixm=ix
  xxyy=(1-dy)*((1-dx)*rb(ibl)%rz%fs(:,ixm,iym)
$           +dx*rb(ibl)%rz%fs(:,ix,iym))
$           +dy*((1-dx)*rb(ibl)%rz%fs(:,ixm,iy )
$           +dx*rb(ibl)%rz%fs(:,ix,iy))
  CALL lagr_quad_basis_assign_loc(rb(ibl)%rz,
$           xxyy,ibasis,ix,iy)
ENDDO
ENDDO
ENDDO
ENDDO

```

To ensure that the finite element mesh is smooth and has high enough resolution in regions of large gradients, an iterative grid smoothing technique is used for simulations of MRX. The positions of the finite element vertices along the exterior and flux core boundaries are specified. Then, a new position for every finite element vertex is calculated using a weighted average technique from the positions of the surrounding vertices calculated during the previous iteration,

$$R_{i+1} = \frac{1}{\sum_i W_i} \sum_i R_i W_i, \quad (\text{A.1})$$

$$Z_{i+1} = \frac{1}{\sum_i W_i} \sum_i Z_i W_i. \quad (\text{A.2})$$

For most vertices the sums in equations (A.1) and (A.2) are taken over the surrounding eight vertices. However, there are four vertices in the MRX grid where five **rblocks** meet

which consequently have nine surrounding vertices (see Figure 2.1). The weight function $W(R, Z)$ is chosen to provide high resolution in and around the current sheet, along the quadrupole field, and near the flux core boundaries. Different weight functions are used for push and pull reconnection and for two-fluid and resistive MHD simulations. The weight functions and placement of exterior finite element vertices are manually fine-tuned to ensure that no elements are excessively distorted and that resolution is adequate in the necessary locations within the computational domain. Results are typically best when element sizes vary gradually rather than abruptly. In most instances, it is best to use mesh packing only for the element vertices and not for the interior nodes (e.g., this step should be taken prior to the loop that sets up interior node positions). However, to ensure smooth application of electric field boundary conditions during simulations of MRX, the placement of the interior nodes for the first ring of elements around each flux core are put along circular arcs so that there are no distinct corners at element boundaries around the flux cores.

A.3 Defining Initial Conditions for a Logically Non-Rectangular Grid

Establishing initial conditions for a logically non-rectangular grid is similar to the process taken in Section A.2 to establish such a grid. For a logically rectangular grid, the equilibrium fields are established in the data structures `lbq` (magnetic field), `ljq` (current density), `lpq` (pressure), and `lnd` (number density). Additionally, diffusivity shaping is stored in `ldiff`. For a logically non-rectangular grid, the equilibrium fields are established in the block decomposed data structure `rb`. The equilibrium magnetic field is stored in `rb(ib1)%be_eq`, the equilibrium current density is stored in `rb(ib1)%ja_eq`, the equilibrium velocity is stored in `rb(ib1)%ve_eq`, the equilibrium pressure is stored in `rb(ib1)%pres_eq`,

the equilibrium electron pressure is stored in `rb(ib1)%prese_eq`, the equilibrium number density is stored in `rb(ib1)%nd_eq`, and diffusivity shaping is stored in `rb(ib1)%diff_shape` for each `rblock`. For simulations of MRX, the initial conditions are constant density and temperature, no velocity and current density, and magnetic field comes from either circular current loops centered around $R = 0$ (for cylindrical geometry) or infinite wires in the out-of-plane direction (for linear geometry).

For a scalar such as number density which often is initially set to a constant, the procedure for implementing simple.

```

DO ibl=1,nrb1
  mxb = rb(ib1)%mx
  myb = rb(ib1)%my
  CALL lagr_quad_alloc(rb(ib1)%nd_eq,mxb,myb,1_i4,poly_degree,
$      name='lnd_eq',title=(/' lndeq'/))
  rb(ib1)%nd_eq%fs=ndens
  IF(poly_degree.GT.1)THEN
    rb(ib1)%nd_eq%fsh=ndens
    rb(ib1)%nd_eq%fsi=ndens
    rb(ib1)%nd_eq%fsv=ndens
  ENDIF
ENDDO

```

Many fields are functions of position. The following loop stores the poloidal position information in the variables `rpt` and `zpt`, which can then be used to calculate the value of a field for that point.

```

DO ibl=1,nrbl
  CALL lagr_quad_alloc(rb(ibl)%diff_shape,mxb,myb,
$    1_i4, !change to 3_i4 for a 3D vector
$    poly_degree,name='ldiff',title=(/' ldiff'/))
  DO ibasis=1,SIZE(rb(ibl)%diff_shape%ix0)
    DO iy=rb(ibl)%diff_shape%iy0(ibasis),rb(ibl)%diff_shape%my
      DO ix=rb(ibl)%diff_shape%ix0(ibasis),rb(ibl)%diff_shape%mx
        dx=ix-rb(ibl)%diff_shape%ix0(ibasis)
$         +rb(ibl)%diff_shape%dx(ibasis)
        dy=iy-rb(ibl)%diff_shape%iy0(ibasis)
$         +rb(ibl)%diff_shape%dy(ibasis)
        CALL lagr_quad_eval(rb(ibl)%rz,dx,dy,0_i4)
        rpt=rb(ibl)%rz%f(1) !calculate R position
        zpt=rb(ibl)%rz%f(2) !calculate Z position
        diff_value = calc_diff_shape(rpt,zpt) !scalar
        CALL lagr_quad_basis_assign_loc(rb(ibl)%diff_shape,
$          (/diff_value/),ibasis,ix,iy)
      ENDDO
    ENDDO
  ENDDO
ENDDO

```

A three dimensional vector field can be implemented in much the same way.

A.4 Connectivity

After establishing element positions in the `rb` data structure, connectivity information must be saved in the `seam` and `seam0` data structures. The `seam` data structure contains connectivity information between different `rblocks`, whereas the `seam0` data structure is used to specify which element vertices are along the exterior of the domain. See Sovinec (2001, pages 56–59) for descriptions of the `seam` and `seam0` data structures.

Some complications must be considered when using bicubic or higher order finite element basis functions are used before arbitrarily stitching together `rblocks`. These complications arise from the way NIMROD handles connectivity information between two element vertices. In particular, NIMROD assumes a particular ordering of the interior nodes. For example, a logically “top” seam of an `rblock` will match with a logically “bottom” seam or a logically “right” seam, but the interior node ordering will not work for a logically “top” seam against a logically “top” seam or a logically “left” seam. For MRX, this problem is avoided by rotating four `rblocks` in logical space to ensure that the logical internal node ordering is consistent with the conventions used by NIMROD. Otherwise, simulations would be limited to polynomial degree ≤ 2 for which the ordering of nodes along block boundaries is irrelevant.

Because of the non-trivial nature of the grid in MRX, seam information must be programmed in manually. The following steps are necessary to define `seam0`.

1. Define `nv` to be total number of exterior finite element vertices
2. Perform the following allocations

```
seam0%nvert = nv
ALLOCATE(seam0%vertex(nv))
```

```

ALLOCATE(seam0%excorner(nv))
ALLOCATE(seam0%r0point(nv))
ALLOCATE(seam0%expoint(nv))
ALLOCATE(np(nv))

```

Set `seam0%excorner` and `seam0%r0point` to be false except for exterior corners and when $R = 0$, respectively.

3. With `iv` as the index for `seam0`, set `np(iv)=1` for exterior vertices that are contained within only one block and `np(iv)=2` for exterior vertices that are part of two blocks.
4. Perform the following loop to allocate `seam0%vertex(iv)%ptr`

```

DO iv=1,nv
  CALL ptr_alloc(seam0%vertex(iv),2_i4,np(iv))
ENDDO

```

5. Perform a loop around the boundary that includes the following commands for each vertex,

```

seam0%vertex(iv)%ptr(1,1) = ibl  !block number
seam0%vertex(iv)%ptr(2,1) = ivb  !vertex index within block

```

where `ibl` is the `rblock` index and `ivb` is the vertex index within the `rblock`. If the vertex is included within a second `rblock`, then it is necessary to also include the following commands

```

seam0%vertex(iv)%ptr(1,2) = ibl2
seam0%vertex(iv)%ptr(2,2) = ivb2

```

After `seam0` has been successfully established, it is necessary to define `seam` using the following steps.

1. Declare `np_array`:

```

TYPE :: np_array_type
    INTEGER(i4), DIMENSION(:), ALLOCATABLE :: npb
END TYPE np_array_type
TYPE (np_array_type), DIMENSION(nrbl) :: np_array

```

This structure will contain the number of connections each vertex within a block.

2. Allocate the seam data structure and `np_array(ibl)%npb(iv)`:

```

ALLOCATE(seam(nrbl))
DO ibl=1,nrbl
    nv = 2*rb(ibl)%mx + 2*rb(ibl)%my
    seam(ibl)%nvert=nv
    ALLOCATE(seam(ibl)%vertex(nv))
    ALLOCATE(seam(ibl)%excorner(nv))
    ALLOCATE(np_array(ibl)%npb(nv))
    DO iv=1,nv !initialize with the most common case
        seam(ibl)%excorner(iv) = .FALSE.
        np_array(ibl)%npb(iv) = 1_i4
    ENDDO
ENDDO

```

Here, `iv` is the vertex index within an `rblock` and `nv` is the total number of vertices within an `rblock`.

3. For each vertex along the boundary of an `rblock` that is connected to more than one other vertex, The following statement says that vertex at the logically top right corner of `rblock #1` is connected to three additional vertices from different `rblocks`.

```
np_array(1)%npb(rb(1)%mx+rb(1)%my) = 3
```

4. After `np_array` is correctly defined, then allocate `seam(ibl)%vertex(iv)%ptr`

```
DO ibl=1,nrbl
  DO iv=1_i4,seam(ib)%nvert
    CALL ptr_alloc(seam(ibl)%vertex(iv),2_i4,np_array(ibl)%npb(iv))
    DO ip=1,np_array(ibl)%npb(iv)
      seam(ibl)%vertex(iv)%ptr(1,ip)=0_i4 !initializing to
      seam(ibl)%vertex(iv)%ptr(2,ip)=0_i4 !unphysical values
    ENDDO
  ENDDO
ENDDO
```

Here, the index `ip` is defined such that each vertex that is connected to a different vertex is given its own `ip`.

5. Use the subroutines `seam_match` and `seam_kitty` to connect the `rblocks` to each other within the `seam` data structure. The code and examples are given in Section A.4.1.

6. Assign `ix` and `iy` with `seam` for each of the vertices (using code from `seam_init` in `nimset_init.f`).

```

DO ib=1,nbl
    mxb=rb(ib)%mx
    myb=rb(ib)%my
    ALLOCATE(ixv(2*(mx+my)))
    ALLOCATE(iyv(2*(mx+my)))
    ixv=(/(ix,ix=1,mxb),(mxb,iy=1,myb),
$      (ix,ix=mx-1,0,-1),(0,i4,iy=my-1,0,-1)/)
    iyv=(/(0,i4,ix=1,mxb),(iy,iy=1,myb),
$      (myb,ix=mx-1,0,-1),(iy,iy=my-1,0,-1)/)
    DO iv=1,seam(ib)%nvert
        seam(ib)%vertex(iv)%intxy(1)=ixv(iv)
        seam(ib)%vertex(iv)%intxy(2)=iyv(iv)
    ENDDO
    DEALLOCATE(ixv)
    DEALLOCATE(iyv)
ENDDO

```

After all of these steps have been implemented, it is necessary to test the grid and connectivity using `nimrod`. The easiest method for testing connectivity is typically a diffusion problem, but wave tests are also practical. Problems with the grid can easily be seen using `nimplot` and `xdraw`.

A.4.1 Seam Matching Subroutines

The following subroutines, `seam_match` and `seam_kitty`, were developed for the MRX application to simplify the process of establishing seams between different `rblocks` in NIM-ROD. The subroutine `seam_match` matches seams for block boundaries that face each other, and `seam_kitty` matches seams for block boundaries at corners where only one point from each block borders the other block.

```

=====
c      subprogram seam_match
c      Takes the border between two blocks and matches them.  Inputs are
c      ib1,ib2 = block numbers being matched.
c      Note that we need iv1A < iv1B in order to get the matching right.
c      If you are starting from scratch, nimrod generally assumes that
c      same_dir=.FALSE. so it is good to build this into the grid from
c      the beginning, ie that adjacent blocks always have their vertices
c      increasing in opposite directions.
=====

      SUBROUTINE seam_match(ib1,ib2,iv1A,iv1B,iv2A,iv2B,same_dir)
      INTEGER(i4) :: ib1,ib2,iv1A,iv1B,iv2A,iv2B,il,nside,
&      ip1A,ip1B,ip2A,ip2B,iv1,iv2,np1A,np2A,np1B,np2B,ip
      LOGICAL :: same_dir

      ip1A = 1
      ip2A = 1
      ip1B = 1

```

```

ip2B = 1
c-----
c   Get side information from block 1.  This means that if we are
c   looking at where the vertex index wraps around (as in the bottom
c   of block #2, etc) then block 2 should be the block that involves
c   a discontinuity. The vertex index iv must be continuous in block 1
c-----

nside = abs(iv1A-iv1B)
IF (iv1A.GE.iv1B) THEN
    write (*,*) 'Blocks are: ', ib1,ib2
    CALL nim_stop("seam_match: Need iv1A < iv1B")
ENDIF

c-----
c   see comments at beginning of this subroutine since same_dir should
c   be considered false.
c-----

IF(same_dir)THEN
    CALL nim_stop("same_dir=T will cause an error in edge_segment
&_init in edge.f")
ENDIF

c-----
c   Get the indices for the pointers for the four cases.
c   Points A+B, blocks 1+2.
c   seam(ib)%vertex(iv)%ptr(:,*) <--starred index

```

c-----

```
np1A = SIZE(seam(ib1)%vertex(iv1A)%ptr,2)
IF (np1A.GT.1) THEN
  ted1A: DO ip=1,np1A
    IF (seam(ib1)%vertex(iv1A)%ptr(2,ip).LT.1) THEN
      ip1A = ip
      EXIT ted1A
    ENDIF
  ENDDO ted1A
ELSE
  IF (seam(ib1)%vertex(iv1A)%ptr(1,ip).GT.0) THEN
    write (*,*) 'seam_match: no valid points: ip1A',
$      ' ib1=',ib1,' ib2=',ib2, ' iv1A=',iv1A, ' iv2A=',iv2A
  ENDIF
  ip1A = 1
ENDIF
```

c-----

```
np1B = SIZE(seam(ib1)%vertex(iv1B)%ptr,2)
IF (np1B.GT.1) THEN
  DO ip=1,np1B
    IF (seam(ib1)%vertex(iv1B)%ptr(2,ip).LT.1) THEN
      ip1B = ip
      EXIT
    ENDIF
  ENDIF
```

```

        ENDDO
ELSE
    IF (seam(ib1)%vertex(iv1B)%ptr(2,1).GT.0) THEN
        write (*,*) 'seam_match: no valid points: ip1B',ib1,ib2
    ENDIF
    ip1B = 1
ENDIF

```

c-----

```

np2A = SIZE(seam(ib2)%vertex(iv2A)%ptr,2)
IF (np2A.GT.1) THEN
    DO ip=1,np2A
        IF (seam(ib2)%vertex(iv2A)%ptr(2,ip).LT.1) THEN
            ip2A = ip
            EXIT
        ENDIF
    ENDDO
ELSE
    IF (seam(ib2)%vertex(iv2A)%ptr(2,1).GT.0) THEN
        write (*,*) 'seam_match: no valid points: ip2A',ib1,ib2
    ENDIF
    ip2A = 1
ENDIF

```

c-----

```

np2B = SIZE(seam(ib2)%vertex(iv2B)%ptr,2)

```

```

IF (np2B.GT.1) THEN
  DO ip=1,np2B
    IF (seam(ib2)%vertex(iv2B)%ptr(2,ip).LT.1) THEN
      ip2B = ip
      EXIT
    ENDIF
  ENDDO
ELSE
  IF (seam(ib2)%vertex(iv2B)%ptr(2,1).GT.0) THEN
    write (*,*) 'seam_match: no valid points: ip2B',ib1,ib2
  ENDIF
  ip2B = 1
ENDIF

```

c-----

c Check for errors and match vertex A

c-----

```

IF (seam(ib1)%vertex(iv1A)%ptr(1,ip1A).GT.0) THEN
  write (*,*) 'seam_match: Overlap: ',ib1,ib2,' iv1A'
ENDIF

IF (seam(ib2)%vertex(iv2A)%ptr(1,ip2A).GT.0) THEN
  write (*,*) 'seam_match: Overlap: ',ib1,ib2,' iv2A'
ENDIF

seam(ib1)%vertex(iv1A)%ptr(1,ip1A) = ib2
seam(ib1)%vertex(iv1A)%ptr(2,ip1A) = iv2A

```

```

seam(ib2)%vertex(iv2A)%ptr(1,ip2A) = ib1
seam(ib2)%vertex(iv2A)%ptr(2,ip2A) = iv1A
c-----
c   Check for errors and match vertex B
c-----

IF (seam(ib1)%vertex(iv1B)%ptr(1,ip1B).GT.0) THEN
    write (*,*) 'seam_match: Overlap: ',ib1,ib2,'iv2B'
ENDIF

IF (seam(ib2)%vertex(iv2B)%ptr(1,ip2B).GT.0) THEN
    write (*,*) 'seam_match: Overlap: ',ib1,ib2,'iv2B'
ENDIF

seam(ib1)%vertex(iv1B)%ptr(1,ip1B) = ib2
seam(ib1)%vertex(iv1B)%ptr(2,ip1B) = iv2B
seam(ib2)%vertex(iv2B)%ptr(1,ip2B) = ib1
seam(ib2)%vertex(iv2B)%ptr(2,ip2B) = iv1B

c-----
c   Now match the vertices in between A & B.
c   same_dir=T means that iv1 increases when iv2 increases
c-----

DO il=1,nside-1
    iv1=il+iv1A
    IF (same_dir) THEN
        iv2 = il + iv2A
    ELSE

```

```

        iv2 = iv2A - il
    ENDIF

c-----
c   Verify that nothing is being written over.
c-----

    IF (seam(ib1)%vertex(iv1)%ptr(2,1).GT.0) THEN
        write (*,*) 'seam_match: overlap in between A & B. iv1'
        write (*,*) 'ib1=',ib1,' ib2=',ib2, ' iv1=',iv1,' iv2=',iv2
    ENDIF

    IF (seam(ib2)%vertex(iv2)%ptr(2,1).GT.0) THEN
        write (*,*) 'seam_match: overlap in between A & B. iv2'
        write (*,*) 'ib1=',ib1,' ib2=',ib2, ' iv1=',iv1,' iv2=',iv2
    ENDIF

c-----
c   Put the parameters into their final place in seam%vertex%ptr
c-----

    seam(ib1)%vertex(iv1)%ptr(1,1) = ib2
    seam(ib1)%vertex(iv1)%ptr(2,1) = iv2
    seam(ib2)%vertex(iv2)%ptr(1,1) = ib1
    seam(ib2)%vertex(iv2)%ptr(2,1) = iv1

ENDDO

RETURN

END SUBROUTINE seam_match

```

```

=====
c      subprogram seam_kitty
c      Matches the seams for blocks that are kitty corner to each other.
c      Includes error checking to make sure the indices are reasonable.
=====
      SUBROUTINE seam_kitty(ib1,ib2,iv1,iv2)
      INTEGER(i4) :: ib1,ib2,iv1,iv2,ip1,ip2,ip,np1,np2
c-----
c      Find the indices ip1 and ip2 for seam%vertex(:,*) <--starred index
c-----

      np1 = SIZE(seam(ib1)%vertex(iv1)%ptr,2)
      IF (np1.GT.1) THEN
        DO ip=1,np1
          IF (seam(ib1)%vertex(iv1)%ptr(2,ip).LT.1) THEN
            ip1 = ip
            EXIT
          ENDIF
        ENDDO
      ELSE
        IF (seam(ib1)%vertex(iv1)%ptr(2,1).GT.0) THEN
          write (*,*) 'seam_match: no valid points: ip1',ib1,ib2
        ENDIF
        ip1 = 1
      ENDIF

```

```
c-----  
  
np2 = SIZE(seam(ib2)%vertex(iv2)%ptr,2)  
IF (np2.GT.1) THEN  
  DO ip=1,np2  
    IF (seam(ib2)%vertex(iv2)%ptr(2,ip).LT.1) THEN  
      ip2 = ip  
      EXIT  
    ENDIF  
  ENDDO  
ELSE  
  IF (seam(ib2)%vertex(iv2)%ptr(2,1).GT.0) THEN  
    write (*,*) 'seam_match: no valid points: ip2',ib1,ib2  
  ENDIF  
  ip2 = 1  
ENDIF  
  
c-----  
c   Now check to make sure there is no overlap.  
c-----  
  
IF (seam(ib1)%vertex(iv1)%ptr(1,ip1).GT.0) THEN  
  write (*,*) 'seam_kitty: Overlap: ',ib1,ib2,'iv1'  
ENDIF  
  
IF (seam(ib2)%vertex(iv2)%ptr(1,ip2).GT.0) THEN  
  write (*,*) 'seam_kitty: Overlap: ',ib1,ib2,'iv2'  
ENDIF
```

```

c-----
c   Put the points into seam(ib)%vertex(iv)%ptr(:,ip)
c-----

      seam(ib1)%vertex(iv1)%ptr(1,ip1) = ib2
      seam(ib1)%vertex(iv1)%ptr(2,ip1) = iv2
      seam(ib2)%vertex(iv2)%ptr(1,ip2) = ib1
      seam(ib2)%vertex(iv2)%ptr(2,ip2) = iv1

      RETURN

      END SUBROUTINE seam_kitty

```

Prior to using these subroutines it is necessary to define the number of connections each vertex has with other vertices so that `seam(ib1)%vertex(iv)%ptr` can be appropriately allocated. The call of `seam_kitty` given by

```
CALL seam_kitty(3,13, rb(3)%mx+rb(3)%my, rb(13)%mx)
```

defines the seam for the top right logical corner of rblock #3 to go with the bottom right logical corner for rblock #13. The code

```

CALL seam_match(1, 2, !rblock numbers
&   rb(1)%mx + rb(1)%my,      !starting iv for first rblock
&   2*rb(1)%mx + rb(1)%my,   !ending iv for first rblock
&   rb(2)%mx,                !starting iv for second rblock
&   2*rb(2)%mx + 2*rb(2)%my, !ending iv for second rblock
&   .FALSE.)

```

sets the seam between the logical top boundary of rblock #1 and the logical bottom boundary of rblock #2. The subroutine is able to handle the case where `iv` goes from `nv`

to 1 while wrapping around the logically bottom left corner.

References

Sovinec, C. R. 2001, *A Tutorial on NIMROD Physics Kernel Development*, UW-CPTC 01-3,
available at: http://www.cptc.wisc.edu/reports/UW-CPTC_01-3.pdf

Yamada, M., Ji, H., Hsu, S., Carter, T., Kulsrud, R., Bretz, N., Jobes, F., Ono, Y., &
Perkins, F. 1997, *Phys. Plasmas*, 4, 1936